ROTATING OPTICAL BEAMS: DIGITAL HOLOGRAPHIC GENERATION, PROPERTIES AND SELF-RECONSTRUCTION DYNAMICS

BY

RONALD K. ROP
(Sc./PhD/P/17/07)
B.Ed., M.Sc. (Egerton)

A THESIS SUBMITTED IN PARTIAL FULFILMENT OF THE REQUIREMENTS FOR THE AWARD OF THE DEGREE OF DOCTOR OF PHILOSOPHY IN PHYSICS OF UNIVERSITY OF ELDORET, KENYA.

2013

DECLARATION

Declaration by Candidate

I hereby declare that the work presented in this thesis is my own original work and that, to the best of my knowledge and belief, has not been presented for a degree in any other university. No part of this thesis may be reproduced without the prior written permission of the author and/or University of Eldoret, Kenya.

Signature: ___________________________ Date: ___________________

Rop, Ronald K. (Sc./PhD/P/17/07)

Declaration by Supervisors

This thesis has been submitted for examination with our approval as the University supervisors.

Name of Supervisor: Prof. George Amolo

Signature: ______________________ Date: ___________________
Department of Physics, University of Eldoret, Kenya

Name of Supervisor: Dr. Nicholas Makau

Signature: ______________________ Date: ___________________
Department of Physics, University of Eldoret, Kenya

DEDICATION

To my family: my wife Joyce and children Ezra, Esther and Ann, in appreciation of their patience and understanding during the many days of my absence

and

to my parents and siblings who have given me much more than words can express.

ABSTRACT

This thesis reports on an experimental investigation of rotating optical beams. Superpositions of higher-order Bessel beams with rotating intensity profiles were generated using a digital holographic experimental technique and the propagation properties in free space were investigated. Phase masks of two annular rings, of equal width but different radii were digitally generated and imprinted on a spatial light modulator. The digital phase masks were illuminated with a linearly polarized He-Ne laser beam to obtain superpositions of higher-order Bessel beams of the same order but of opposite topological charges and of different orders but same or different topological charges depending on the number of times the azimuthal phase in one annular ring varied relative to the other ring. The superposition of beams with the same order but opposite topological charges resulted in fields with on average zero orbital angular momentum but which exhibited a rotation in their intensity profiles. On the other hand, the superposition of beams with unequal orders produced orbital angular momentum-carrying Helicon beams with rotating intensity profiles. The rotation rates of the generated superposition fields were measured for different orders and for various values of the difference between the wave-vectors of the superimposing beams. The experimental results showed that the intensity profiles rotated at constant rates, for example 30.14 rad/m, as the fields propagated and that the rotation rates varied linearly with the difference between the wave vectors of the superimposing beams and inversely as the order of the beams for zero orbital angular momentum beams and inversely as the difference between the orders of the beams for Helicon beams. In addition, the propagation of the rotating optical beams past total and partial obstructions of different geometries set on- or off-axis was investigated theoretically and experimentally. The experimental results showed that the rotation of the intensity profile does not affect the self-reconstruction of rotating Bessel beams. However, the position of the obstacle with respect to the propagation axis of the beam is important in determining the nature of the reconstruction process of the beams. For on-axis obstructions, the reconstructed beam had the form and orientation of the unobstructed beam but off-axis obstructions resulted in a beam which does not attain the exact form of the unobstructed beam.

TABLE OF CONTENTS

LIST OF TABLES

LIST OF FIGURES

LIST OF SYMBOLS

$E(x, y, z, t)$ - Time dependent scalar electric field in rectangular coordinates

$E(r, \theta, z)$ - Scalar electric field in cylindrical coordinates

r - Radial coordinate

θ - Azimuthal coordinate

z - Longitudinal coordinate or distance

k - Wave number

k_r - Radial wave number

k_z - Longitudinal wave number

k_θ - Azimuthal wave number

ω - Angular frequency

c - Velocity of light in a vacuum (or free space)

λ - Wavelength of light

$A(\theta)$ - Complex angular spectrum of a field

ξ - Constant specifying the direction of rotation and the longitudinal period of a field

η - Arbitrary real function

Δz - Change in propagation distance

m - Azimuthal index, which represents the order of a Bessel beam

$J_m(k_r r)$ - m^{th} order Bessel function of the first kind

a_m - Fourier coefficients

α - Half-angle of the cone of wave vectors constituting a Bessel beam

$t(r,\theta)$ - Transmission function of the ring slit aperture

Δ - Width of each ring slit

r_i - Radius of the inner ring slit

r_o - Radius of the outer ring slit

r_c - Average radius of the two ring slits

Δk - Difference between the longitudinal wave numbers of the two Bessel beams traversing the two ring slits

Δm - Absolute difference between the orders of the two superimposed Bessel beams

D - Diameter (or size) of obstacle

$z_{\min}$ - Reconstruction distance of a Bessel beam

f - Focal length of Fourier lens

γ - Opening angle of axicon

$H_0^{(1)}(k_r r)$ - Zero-order Hankel function of the first kind

$H_0^{(2)}(k_r r)$ - Zero-order Hankel function of the second kind

$N_0(k_r r)$ - Zero-order Newman function

∇ - Del operator

∇^2 - Laplacian operator

$R(z)$ - Radius of curvature of a Gaussian beam (GB)

ω_0 - Beam waist of a GB

$\omega(z)$ - Beam width of a GB

z_0 - Rayleigh range of a GB

ϕ - Divergence of a GB

φ - Additional phase shift of a GB

‘i’ - Complex notation

ε_0 - Permittivity of a vacuum (or free space)

μ_0 - Permeability of a vacuum (or free space)

f_T - Focal length of tube lens

f_o - Focal length of objective lens

m_{eff} - Effective magnification of objective lens

ACRONYMS

BBs	-	Bessel beams
BMM	-	Biomedical microscopy
BNS	-	Boulder Nonlinear Systems
CCD	-	Charge-coupled device
CGH	-	Computer generated holography
CGHs	-	Computer generated holograms
CWs	-	Conical waves
DH	-	Digital holography
DHM	-	Digital holographic microscopy
DM	-	Deformable mirror
DOE	-	Diffractive optical element
EA	-	Electrically addressed
ELS	-	Elastic light scattering
FT	-	Fourier transform
FWHM	-	Full width at half maximum
GB(s)	-	Gaussian beam(s)
HGBs	-	Hermite-Gaussian beams

HOBB(s)	-	Higher-order Bessel beam(s)
HOT	-	Holographic optical tweezing
ICW	-	Incoming conical wave
LASER	-	Light amplification by stimulated emission of radiation
LC(s)	-	Liquid crystal(s)
LCD	-	Liquid crystal display
LCSLM	-	Liquid crystal spatial light modulator
LG	-	Laguerre-Gaussian
LGBs	-	Laguerre-Gaussian Beams
MCP	-	Micro-channel plate
MO	-	Magneto-optic
MOSLM	-	Magneto-optic spatial light modulator
MQW	-	Multiple-quantum well
MTF	-	Modulation transfer function
NIR	-	Near Infrared
OA	-	Optically addressed
OAM	-	Orbital angular momentum
OCW	-	Outgoing conical wave
PIOFs	-	Propagation-invariant optical fields
RBBs	-	Rotating Bessel beams
RMS	-	Royal metric system

ROACH	-	Reference-less on-axis complex hologram
ROFs	-	Rotating optical fields
RSA	-	Ring slit aperture
SAM	-	Spin angular momentum
SBP	-	Spectral band width
SIFs	-	Self-imaging fields
SLM(s)	-	Spatial light modulator(s)
TEM	-	Transverse electric magnetic
ZOBB(s)	-	Zero-order Bessel beam(s)

ACKNOWLEDGEMENTS

Foremost, I would like to thank God for the gift of life, the gift of salvation, the blessing of good health and for His surpassing grace that has always been sufficient throughout the entire duration of the course.

In addition, I have the umpteenth privilege to acknowledge, with sincere gratitude, the contribution of many persons and institutions without whose support this work would have been near impossible to implement and even complete. I would like to thank Prof. George Amolo and Dr. Nicholas Makau of Physics Department, University of Eldoret for accepting to supervise me, for their patience and persistence, for their generosity of ideas and for the immense support they gave me wholeheartedly during the entire period. We have shared very many light moments together that have been instrumental in breaking the routine of searching through volumes of books. Their faith in my ability to measure up has always inspired me. Thanks also to the former Head of Physics Department, Prof. Samuel Rotich, to the current Head Dr. Joel Tonui and to Dr. David Waswa for support and the many fruitful discussions we had.

I am profoundly grateful to Professor Andrew Forbes, Chief Scientist and Research Group Leader (Mathematical Optics), National Laser Centre (NLC), CSIR, South Africa for accepting to host me in his Mathematical Optics group and lab and for his

invaluable guidance during the many research visits I made to NLC. Prof Andrew offered me an opportunity that transformed many aspects of my life. I am indebted to Andrew for his patience, tolerance, availability, astuteness and veracity. On the same note, I appreciate the NLC team and in particular the NLC Manager Dr Ndumiso Cingo and the ALC Manager Dr Paul Motalane for their generosity and support. I am grateful to the ALC for granting me a scholarship to undertake research work. Special thanks go to Drs Igor Litvin and Steff Roux for their guidance and other members of Mathematical optics group: Angela, Yaseera, Darryl and Ati who were always willing and available to support me in my experimental and theoretical work. Angela and Yaseera were very instrumental in helping me in the lab. In addition, Cosmas, Melaku, Bathusile and Bonex were always helpful. I also would like to thank the Entabeni community: the manager Yuanita and the friends with whom we frequently met for their hospitality and communion. Their presence made my stay in Entabeni, CSIR and South Africa enjoyable and memorable. I also thank Prof Hellen Gleeson (University of Manchester, UK), Dr Carlos Lopez-Mariscal (US Naval Research Laboratory) and Prof Thomas Freuer (University of Bern, Switzerland) for very valuable discussions and their willingness to support my work.

I would also like to thank UNESCO/ANSTI Office in Nairobi for granting me two research staff exchange fellowships to visit the NLC. Special thanks to Prof Massaquoi, Mary, Joseph and David for facilitating the same. On the same note, I thank Egerton University for granting me study leave for the duration of the course and its staff Dr Sang, Dr Kirui, Dr Hussein, and Prof. Omolo for their constant encouragement to me to pursue and complete the PhD.

Finally, I am grateful to my dear wife Joyce for her support, patience, strength of character and a great deal of understanding during the whole period. In particular, she has been a constant encouragement to me to complete the course. I am indebted to her for ably and single-handedly taking care of our children Ezra, Esther and Ann during the many days of my absence. I also thank my parents, Zakayo and Ruth Cheruiyot, my siblings Philip, Edna, Fred, Leonard and Jennifer and my many friends for their great support. I look forward to sharing with you the joy of completing the course.

Thank you all and may God bless you.

THESIS OUTLINE

This thesis comprises six chapters. Chapter 1 is the introduction: it gives an overview of the subject area of the thesis: rotating optical beams. The chapter highlights briefly the emergence and development of the laser as a source of light and as electromagnetic radiation. It discusses briefly some laser beams such as Gaussian beams and the various novel laser beams. In addition, the chapter presents the significance and the objectives of the study and the statement of the problem.

In Chapter two, a review of literature in the area of novel laser beams and in particular Bessel and rotating optical fields is presented. The various experimental and theoretical methods, which have been used by earlier investigators to generate Bessel beams and rotating optical beams are presented in detail along with their limitations. Chapter three presents the theoretical background of laser beams but in particular of Bessel beams and rotating optical beams. New aspects of the theory on superposition of coherent beams are also highlighted.

In Chapter four, the experimental methods used for generating rotating optical fields (in particular rotating Bessel beams), for measuring the rotation rates of these fields and for investigating their propagation in free space and their propagation dynamics past total and partial obstructions are discussed. The experimental layouts are also presented. Chapter five presents the experimental results in form of two-dimensional plots and images of the intensity profiles of the rotating beams and of the obstructed fields. The images obtained by theoretical simulations are also presented for comparison purposes. The results are discussed in detail in the same chapter. Finally, Chapter 6 presents a summary of the conclusions and recommendations based on the results obtained. Thereafter, a list of the references cited in this thesis is presented. A list of publications and conference presentations, the data tables and the MatLab® and Mathematica® scripts used, respectively, for generating the digital phase masks and for simulating theoretical images are presented in the Appendix for future reference and for completeness sake.

CHAPTER ONE

INTRODUCTION

1.1. Overview

It is slightly over half a century ago when the laser, both as a source and as a new type of electromagnetic radiation was first demonstrated by Maiman (1960). In fact, 2010 was the international community's 50 years' anniversary of the LASER. When it was discovered the laser was considered as a "solution without a problem" (Quimby, 2006) but over the last five decades it has developed to become one of the most versatile tools in almost all scientific and technological fields. Lasers have enabled new applications in various fields including the medical and biomedical fields, communication as well as material science and processing. New and more accurate imaging and diagnostic techniques such as biomedical microscopy (BMM), optical holography and interferometry (Hariharan, 1987), digital holographic microscopy (DHM) (Moon, Daneshpanah, Anand & Javidi, 2011), elastic light scattering (ELS) (Robinson et al., 2011) and holographic optical tweezing (HOT) (Curtis, Koss & Grier, 2002) would not have been possible without tailored laser beams.

The development of new laser sources proceeded in tandem with the discovery of new laser beams with interesting intensity profiles and propagation properties. These laser beams, obtained directly as outputs of laser resonators or through beam shaping of ordinary Gaussian beams, have greatly enhanced the applications of lasers. Such laser beams are called novel laser beams, examples of which include Hermite-Gaussian beams (HGBs) and Laguerre-Gaussian beams (LGBs) (Pagani & Nasalski, 2005), Bessel beams (BBs) (McGloin & Dholakia, 2005), Airy beams (Siviloglou, Brokly, Dogariu & Christodoulides, 2007), Mathieu beams (Gutiérrez-Vega et al., 2001) and rotating optical fields (Chavez-Cerda, McDonald & New, 1996; Patterson & Smith, 1996; Pääkkönen et al., 1998). Owing to the unique properties of Bessel beams such as self-reconstruction and the ring structure of their transverse intensity profile, rotating Bessel beams form the subject of investigation of this thesis. In addition, since Bessel beams exhibit self-healing properties, it was of great interest to investigate whether rotating Bessel beams also have reconstruction properties. In the following section, a brief discussion of Gaussian beams is presented as an introduction to the general field of laser beams and in particular rotating beams.

1.2. Introduction to Laser Beams

The electric field of an optical wave propagating in free space can be described by (Peatross & Ware, 2011);

$$\vec{E}\left(r,t\right)=\vec{E}\left(r\right)\exp(-i\omega t)\,, \tag{1.1}$$

where ω is the angular frequency of the field (assumed monochromatic) and ‘i’ is the complex notation. Such a field obeys the wave equation;

$$\nabla^2\vec{E}-\frac{n^2}{c^2}\frac{\partial^2\vec{E}}{\partial t^2}=0\,, \tag{1.2}$$

and propagates with a velocity approximately equal to c/n in a medium of index of refraction n, which is assumed to be uniform. The symbol ∇ is the Laplacian operator and $c = 1/\sqrt{\varepsilon_0\mu_0}$ = 3.0 x 10^8ms^{-1} is speed of the wave (light) in free space in which ε_0 and μ_0 are the permittivity and permeability of free space, respectively. Applying equation (1.2) to (1.1) and performing explicitly the time derivative gives the time-independent Helmholtz equation (Peatross & Ware, 2011);

$$\nabla^2\vec{E}(r) + k^2\vec{E}(r) = 0, \tag{1.3}$$

where $k \equiv n\omega/c$ is the magnitude of the wave vector. In equation (1.3), the trivial time dependence has been omitted. Under scalar approximation, equation (1.3) becomes the scalar Helmholtz equation;

$$\nabla^2 E(r) + k^2 E(r) = 0. \tag{1.4}$$

A more general solution of equation (1.4) in rectangular coordinates and propagating along the z – direction is of the form (Verdeyen, 1995);

$$E(x,y,z) = E_0\psi(x,y,z)\exp(-ikz), \tag{1.5}$$

where E_o is the amplitude factor, $\exp(-ikz)$ is the plane wave factor and $\psi(x,y,z)$ is a slowly varying complex function which gives a measure of the difference between the beam under consideration (such as a laser beam) and a plane wave. Since $\psi(x,y,z)$ varies slowly with z, then applying equations (1.4) and (1.5) yields the paraxial wave equation in cylindrical co-ordinates (Kogelnik & Li, 1966),

$$\frac{1}{r}\frac{\partial}{\partial r}\left(\frac{\partial\psi}{\partial r}\right) - i2k\frac{\partial\psi}{\partial z} = 0. \tag{1.6}$$

The solution to equation (1.6) with cylindrical symmetry is the fundamental Gaussian beam (GB) mode; the transverse electric and magnetic mode, TEM$_{00}$. It is a beam of electromagnetic radiation whose angular distribution is Gaussian. Gaussian beams (GBs) are important because they are the fundamental mode of oscillation of laser resonators with spherical mirrors (Kogelnik & Li, 1966). In addition, the propagation modes of some optical fibres have Gaussian distribution.

The fundamental, symmetric Gaussian beam propagating in the z direction can be expressed in cylindrical coordinates as (Kogelnik & Li, 1966);

$$\psi(r,z)=\frac{\omega_0}{\omega(z)}\exp\left[-\frac{r^2}{\omega^2(z)}\right]\exp\left[-i\frac{kr^2}{2R(z)}\right]\exp[-i(kz-\varphi)], \qquad (1.7)$$

where $r=\left(x^2+y^2\right)^{1/2}$ is the radial distance measured from the z - axis and $\varphi=\arctan(z/z_0)$ is the additional phase shift. The quantity $z_0=(\pi\omega_0^2/\lambda)$ is a constant characteristic of the beam called the Rayleigh range, where λ is the wavelength of the radiation and ω_0 is the beam waist, the minimum radius of the beam measured transversely from the propagation axis at the plane z = 0. The parameter $\omega(z)$ is the radius of the beam at the point where the transverse amplitude of the field is (1/e) of the maximum amplitude and is called the beam width or the spot size and given by;

$$\omega(z)=\omega_0\left[1+\left(\frac{\lambda z}{\pi\omega_0^2}\right)^2\right]^{1/2}. \qquad (1.8)$$

Note that the beam width attains its minimum value ω_0 at z = 0 but increases as the beam propagates along z towards infinity, with the beam divergence being given by $\phi = (\lambda / \pi\omega_0)$. The radius of curvature, $R(z)$ of the wavefront of the beam as measured from the position of minimum beam width is defined as;

$$R(z) = z\left[1 + \left(\frac{\pi\omega_0^2}{z}\right)^2\right]. \tag{1.9}$$

From equation (1.9), it follows that $R(z) \to \infty$ as $z \to 0$, that is, the wavefronts become plane at the beam waist position. As $z \to \infty$, $R(z)$ varies linearly with z. Figure 1.1 shows the evolution of a GB as it propagates along the z direction.

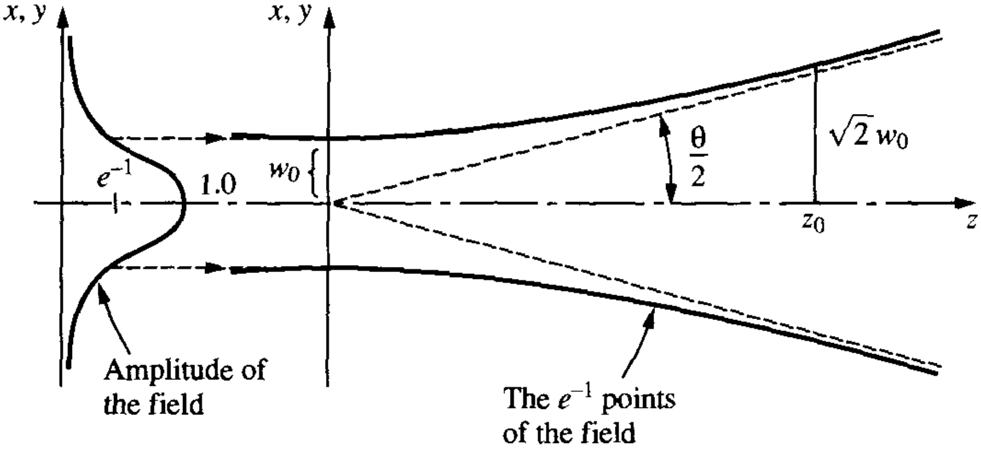

Figure 1.1: The evolution of a GB as it propagates along the z-direction. The inset on the left shows the variation of the amplitude of the field in the transverse direction (Verdeyen, 1995)

The first factor in equation (1.7);

$$\psi_0(r, z) = \frac{\omega_0}{\omega(z)} \exp\left[-\frac{r^2}{\omega^2(z)}\right], \tag{1.10}$$

is the amplitude factor that shows how the amplitude of the field changes as the beam propagates along z. The factor $\omega_0 / \omega(z)$ ensures energy conservation, that is, as the beam expands, the field amplitude decreases in order to keep the total power constant (Weiner & Ho, 2003). From (1.10) it is clear that the amplitude falls off rapidly with r, decreasing from a peak value at r = 0 to a value (1/e) of the peak value at the beam width.

The second factor in equation (1.7) is called the radial phase factor. It describes the spherical phase front of the beam, with the radius of curvature R(z) defined in equation (1.9). The third factor expresses the change in phase $\phi = kz - \arctan(z / z_0)$ of the wave in the direction of propagation and is called the longitudinal phase factor.

1.3. Novel Laser Beams

There are other solutions of the paraxial wave equation (equation 1.3) having some similar properties with GBs but that form a complete and orthogonal set of functions. These are called ‘modes of propagation’ and every arbitrary distribution of monochromatic light can be expanded in terms of these modes (Kogelnik & Li, 1966). For a system with rectangular geometry, these modes constitute Hermite-Gaussian laser beams but for systems with cylindrical symmetry, they constitute Laguerre-Gaussian laser beams. These beams are examples of laser beams that have transverse intensity profiles that differ significantly from those of Gaussian laser beams and are called novel laser beams. Other novel laser beams include Airy beams, Mathieu beams, Bessel beams and rotating optical beams. Airy beams are non-diffracting laser beams with transverse intensity profiles that are described by the Airy function and propagate along a parabolic path (Siviloglou et al., 2007). Mathieu beams are propagation-invariant optical fields (PIOFs) that are solutions of Helmholtz's wave equation in elliptical coordinates (Gutiérrez-Vega et al., 2001). Since Airy beams, Mathieu beams, Laguerre-Gaussian beams and Hermite-Gaussian beams are not the subject of the investigation of this thesis, they will not be discussed further.

Bessel beams are propagation-invariant optical beams that are non-singular scalar solutions to the free-space Helmholtz's wave equation and are described mathematically by Bessel functions [Durnin, 1987; Durnin, Miceli & Eberly, 1987). Zero-order Bessel beams (ZOBBs) have an intensity maximum at the centre while higher-order Bessel beams (HOBBs) have a dark central spot – an intensity null – due to a phase singularity at that point, surrounded by alternate bright and dark rings (McGloin & Dholakia, 2005). HOBBs carry orbital angular momentum (OAM) owing to their azimuthal phase variation. Rotating optical fields (ROFs) are novel laser beams with transverse intensity profiles that rotate about the propagation axis as the beam propagates along the axis (Vasilyeu, Dudley, Khilo & Forbes, 2009). They are obtained from superpositions of higher-order modes of novel laser beams such as Laguerre-Gaussian beams (Kotlyar, Khonina, Skidanov & Soifer, 2007) and Bessel beams (Chavez-Cerda et al., 1996). More discussions of these beams: Bessel and rotating optical beams are presented in Chapter 3 since they form the core of the investigation in this thesis.

1.4. Statement of the problem

This thesis reports on the experimental generation of rotating optical fields (in particular rotating Bessel beams) using digital holographic methods. Rotating optical beams have been experimentally generated using a variety of techniques. For instance, an axicon lens and a physical ring slit aperture, a binary phase diffractive axicon, and a complex spatial filter have been applied to generate the beams. However, the use of these methods resulted in a limited set of rotating beams and a limited flexibility to dynamically control the parameters of the beams. Consequently the range of applications of the beams was also limited.

This study sought to address these challenges by applying digital holography to generate rotating Bessel beams. In addition, the study investigated the propagation properties of the beams in free space and past obstacles of various sizes and geometries placed on and off-axis. Theoretical investigation of the rotation and propagation of these beams was also undertaken as a means of validating the experimental results.

1.5. Objectives of the Study

The objectives of the study are to:

1. Apply digital holography to experimentally generate rotating optical beams
2. Investigate experimentally the free-space propagation of rotating optical beams
3. Measure experimentally the rotation rates of rotating optical beams
4. Investigate the self-reconstruction dynamics of obstructed rotating optical beams

1.6 Significance of the study

Laser applications have grown tremendously since the invention of the first laser. While a number of the applications have been achieved with ordinary Gaussian laser beams, novel laser beams have expanded the scope of these applications. For instance, while optical trapping and manipulation has been possible with GBs, Bessel beams have made it possible to trap, simultaneously, two or more micro-particles that are spatially separated along the direction of beam propagation owing to their self-reconstruction property. In addition, the ring structure of Bessel beams has made it possible to simultaneously trap particles with low and high indices of refraction. On the other hand, rotating optical beams have opened possibilities for trapping and rotating micro-particles, including biological specimens for diagnostics purposes. However, the generation of these beams using ordinary methods such as axicon lenses, binary phase diffractive optical elements (DOEs) and computer generated holograms (CGHs) have limited these applications since only a given set of rotating beams can be generated. In addition, it is difficult to dynamically control the beam since the elements are static in nature. Digital holography provides a versatile and dynamic method for generating and applying these laser beams since it does not require any transparency and chemical or other processing. In addition, the understanding of the propagation properties of rotating optical beams, in free space and past obstacles of various geometries and sizes, opens endless possibilities for existing and new applications.

CHAPTER TWO

LITERATURE REVIEW

2.1 Introduction

Rotating optical fields are an interesting class of novel laser beams for whom transverse intensity distribution experience a rotation about the propagation axis as the beams propagate. The intensity distributions are longitudinally periodic in that the original intensity distribution, including the orientation, is reproduced exactly at integer multiples of a characteristic propagation distance (Pääkkönen et al., 1998). These beams are closely related to exact propagation-invariant optical fields (PIOFs) and self-imaging fields (SIFs) and are therefore also called rotating scale-invariant optical fields.

Rotating optical fields have attracted increased attention in recent years owing to their interesting properties and potential applications in diverse fields but more specifically in optical tweezing. These beams have been applied in optical tweezers to rotate optically trapped particles. The number of arms in the rotating interference pattern can be tailored to match the geometry of the object to be rotated and the pattern can be set into continuous rotation by introducing a frequency shift between the interfering modes. The speed and/ or the orientation of the trapped particles can be controlled by changing the effective path length of one of the interfering beams (MacDonald, Paterson, Volke-Sepulveda, Arlt, Sibbett & Dholakia, 2002). In addition, some rotating optical beams have been applied recently to simultaneously trap and rotate dielectric particles over a spiral path on the optical axis (Kotlyar et al., 2007) and to trap and rotate a Chinese hamster chromosome (Paterson, MacDonald, Arlt, Sibbett, Bryant & Dholakia, 2001). Similarly, a special type of rotating beams has been shown to induce spiral motion on trapped micro-particles along the beam’s path (Daria, Palima & Glückstad, 2011).

Several types of rotating optical fields have been theoretically and experimentally demonstrated. The intensity profiles of the superpositions of Laguerre – Gaussian beams (Kotlyar et al., 2007; Schechner, Pietsun & Shamir, 1996; Kotlyar, Soifer & Khonina, 1997; Khonina, Kotlyar, Soifer, Honkanen, Lautanen & Turunen, 1999), higher-order Bessel beams (Chavez-Cerda et al, 1996; Paterson & Smith, 1996; Pääkkönen et al., 1998; Vasilyeu et al, 2009; Kotlyar et al., 2007; Tervo & Turunen, 2001) and multi-mode Hyper-Geometric beams (Kotlyar et al., 2007) have been shown to experience a rotation and the theoretical conditions necessary for the rotation to occur have been derived (Paterson & Smith, 1996, Pääkkönen et al., 1998; Vasilyeu et al, 2009; Kotlyar et al., 2007; Schechner et al., 1996; Kotlyar et al., 1997). Other types of ROFs include spiralling and spiral-type beams (Jarutis, Matijošius, Trapani, & Piskarskas, 2009; Matijošius, Jarutis, & Piskarskas, 2010; Sun, Zhou, Fang, Liu & Liu, 2011; Anguiano-Morales, Salas-Peimbert & Trujillo-Schiaffino, 2011; Abramochkin & Volostnikov, 1996; Abramochkin, Losevsky & Volostnikov, 1997), optical propellers (Zhang, Huang, Hu, Hernandez & Chen, 2010) and optical twisters (Daria et al., 2011). Optical twisters have both their phase and amplitude describing a helical profile as the beam propagates in free space while optical propellers are optical beams with rotating intensity blades and exhibit self-trapping features.

2.2 Rotating Bessel Beams

2.2.1 Bessel Beams

Bessel beams belong to a special class of laser beams referred to as nondiffracting beams. These beams, also called propagation-invariant beams or diffraction-free beams are non-singular scalar solutions of Helmholtz’s wave equation in free space and are described mathematically by Bessel functions (Durnin, 1987; Durnin et al., 1987). In addition, the beams have sharply defined transverse intensity distributions which are independent of the propagation distance and, like plane waves, have finite energy density but infinite energy and are not square-integrable in the transverse direction (Durnin, 1987). In comparison with a Gaussian beam of the same parameters (same wavelength, central spot size and aperture radius), a zero-order Bessel beam (ZOBB) can travel a distance approximately twenty eight times larger than a Gaussian beam without changing appreciably in shape and transverse intensity distribution (Recami & Zamboni-Rached, 2009).

The first mention of optical beams, other than plane waves, that do not experience diffractive spreading was when Stratton (Stratton, 1941) developed a monochromatic solution to the wave equation that was described by a Bessel function and whose transverse shape was confined in the vicinity of its propagation axis. Several years later, Durnin (1987) and Durnin et al. (1987) demonstrated, theoretically and experimentally, the finite-aperture approximations of these exact solutions which are now called Bessel beams. Since then, other nondiffracting beams have been realized, both theoretically and experimentally. Mathieu beams (Gutiérrez-Vega et al., 2001; Gutiérrez-Vega, Iturbe-Castillo & Chávez-Cerda, 2000; Chávez-Cerda et al., 2002) are exact solutions of Helmholtz equation in elliptical cylindrical coordinates and are described by Mathieu functions. They are PIOFs with a highly localized distribution along one of the transverse directions and a sharply peaked quasi-periodic structure along the other. Parabolic beams (Bandrés, Gutiérrez-Vega & Chávez-Cerda, 2004), on the other hand, are nondiffracting beams that are solutions of Helmholtz's equation in parabolic cylindrical coordinates.

Several investigators have described Bessel beams using different formulations. Durnin (1987) described Bessel beams as a superposition of plane waves whose wave vectors traverse the surface of a cone. The beams can thus be characterized by the opening angle of the cone. Individual propagating waves undergo the same phase shift over a given propagating distance. Bouchal, Wagner and Olivik (1995) considered Bessel beams to be constructed from spherical waves emitted by an annular source and then phase-corrected by a lens to eliminate transverse magnification. Another formulation (Chávez-Cerda et al., 1996; Chávez-Cerda, 1999) decomposes a Bessel beam into two conical waves, one travelling inwards towards the propagation axis and the other travelling away from the axis. These conical waves are described by Hankel functions (Chávez-Cerda, 1999) which are fundamental solutions of Helmholtz's wave equation. The superposition of the incoming and outgoing conical waves leads to the formation of Bessel beams and other PIOFs.

Bessel beams have interesting properties such as the ring structure of the intensity profile, the non-diffracting nature and self-reconstruction. The fundamental Bessel beam, also called the ZOBB has an intensity maximum on the beam axis (the core) while a HOBB has a dark core, an intensity null, due to a phase singularity at that point but in both cases the nondiffracting core is surrounded by alternate bright and dark rings (McGloin & Dholakia, 2005; Durnin, 1987). The energy or power carried by a Bessel beam is evenly distributed between its rings. The higher-order Bessel beams (HOBBs) carry orbital angular momentum (OAM) which arises due to their azimuthal phase variation. Another interesting property of Bessel beams is their self-reconstruction. This property refers to the ability of a Bessel beam to re-form its intensity profile after propagating past an opaque non-absorbing obstacle placed in the path of propagation of the beam (McGloin & Dholakia, 2005). At a certain minimum distance of propagation beyond the obstacle, called reconstruction distance, the intensity profile of the beam is the same as what it would have been at that distance in the absence of the obstruction provided the spatial extent of the obstacle is small compared to the size of the beam. This reconstruction is due to the propagation of one of the unobstructed conical waves that form the Bessel beam.

Self-reconstruction has been studied widely, both theoretically and experimentally. Herman and Wiggins (1991) first suggested that a ZOBB is a type of self-regenerating field that heals rapidly following the stoppage of light in any area comparable in size with the central spot and this has already been demonstrated experimentally for a ZOBB (Bouchal, Wagner & Chlup, 1998). The conical dynamics of Bessel beams obstructed on- and off-axis using an opaque circular obstruction have also been investigated, numerically and experimentally (Anguiano-Morales, Méndez-Otero, Iturbe-Castillo & Chávez-Cerda, 2007). They found that the position, size and form of the obstruction affect the individual conical waves and consequently the invariance or non-diffractive property of these beams could be lost.

Litvin, McLaren and Forbes (2009) applied a conical projection model, which is based on the conical wave formulation, to investigate the reconstruction of Bessel and Bessel-Gauss beams beyond obstacles of arbitrary geometries and complex orientation. The model predicts whether the beam will reconstruct, where it will reconstruct and how the shadow and conical wave regions will change during propagation of the beam away from the obstacle. In addition, they found that the propagation of the Bessel and Bessel-Gauss beams after the obstacle and the potential for reconstruction depended on the geometry and the position of the obstacle in the optical field. The self-reconstruction of Bessel beams in nonlinear media (Sogomonian, Klewitz & Herminghaus, 1997; Butkus et al., 2002), of fractional Bessel beams (Tao & Yuan, 2004), of tightly focused scalar and vector Bessel-Gauss beams (Vyas, Kozawa & Sato, 2011) and of optical airy beams (Broky, Siviloglou, Dogariu & Christodoulides, 2008) has been reported. In addition, the possibility of creating light beams that are self-healing in directions other than the propagation direction has also been demonstrated (Thomson & Courtial, 2008). Snaking or curved trajectory Bessel beams: ZOBBs that can be designed to deviate from straight-line propagation have been experimentally realized (Morris, Čižmár, Dalgarno, Marchington, Gun-Moore & Dholakia, 2010). Such beams can propagate around obstructions placed on the optical axis.

Other aspects of Bessel beams have also been investigated. The mode properties of Bessel beams (Valyaev & Krivoshiykov, 1989) and the OAM of a HOBB based on a vectorial treatment (Volke-Sepulveda, Garcés-Chávez, Chávez-Cerda, Arlt & Dholakia, 2002) have been studied. Martelli, Tacca, Gatto, Moneta and Martinelli (2010) investigated the Gouy phase shift in Bessel beams and showed that the nondiffracting nature of these beams is due to the accumulation of an extra axial phase shift (the Gouy phase shift) which is linearly dependent on the propagation distance. Hacyan and Jáuregui (2006) studied the general properties of Bessel beams, in terms of Hertz potentials, within a fully relativistic framework. They showed that there exists a unique reference frame in which the linear propagation of Bessel beams is eliminated and the waves propagate circularly.

Owing to their unique properties Bessel beams have found a variety of interesting applications. For instance, the optical manipulation of micron-sized particles, including biological samples, using a ZOBB has been demonstrated (Arlt, Garcés-Chávez, Sibbett & Dholakia, 2001). Using laser powers of about 35 mW (corresponding to a power of about 4 mW in the central maximum of the Bessel beam), they were able to optically tweeze and manipulate, in two dimensions, silica spheres, *E. coli* and Chinese hamster chromosomes at speeds of about 10 μm/s. However, at higher laser powers of about 65 mW, they demonstrated optical guiding, alignment and stacking of particles. In optical guiding, the beam's gradient force is used to confine a particle along the propagation axis, in two dimensions, and then the radiation pressure propels the particle along the axis of the laser beam. Such transport of microscopic particles is important for applications in aerosol science, micro-biology and nano-technology. Bessel beams are particularly suited for optical guiding as compared to Gaussian and other hollow beams owing to their nondiffractive propagation. In addition, vertical alignment and subsequent manipulation of elongated samples, such as several biological specimens, allows the isolation and transfer of the samples from one chamber to another. This is particularly useful in chromosome studies where chromatid fragments may need to be spatially separated for polymerase chain reactions to be performed (He, Liu, Smith & Berns, 1997).

The multi-ringed structure of Bessel beams has made possible the simultaneous trapping of both low- and high-index particles (Volke-Sepulveda, Chávez-Cerda, Garcés-Chávez & Dholakia, 2004) while the self-reconstruction property has enabled the simultaneous trapping of particles that are spatially separated (Garcés-Chávez, McGloin, Melville, Sibbett & Dholakia, 2002). Since the beam has different reconstruction distances for different particles depending on their refractive indices, it follows that the self-reconstruction effect can be used as a means of characterizing particles and biological samples. Fahrbach, Simon and Rohrbach (2010) have demonstrated a prototype of a microscope, microscopy with self-reconstructing beams, using self-reconstructing Bessel beams and showed that a holographically shaped, scanned Bessel beam reduces scattering artefacts while simultaneously increasing image quality and penetration depth in dense media. They showed that owing to the self-reconstruction effect, a scanned Bessel beam generated by a computer hologram can produce high quality images in strongly scattering media such as the human skin and other biological samples. The self-reconstructing and propagation-invariant properties of Bessel beams have also been demonstrated to have potential applications in optical interconnects (MacDonald, Boothroyd, Okamoto, Chrostowski & Syrett, 1996; Yu, Wang, Varela & Chen, 2000; Al-Ababneh & Testorf, 2004). It has also been experimentally demonstrated that the OAM and spin angular momentum (SAM) of Bessel beams can be transferred to micro-particles and cold atoms [He, Friese, Heckenberg & Rubinsztein-Dunlop, 1995); Tabosa & Petrov, 1999; Garcés-Chávez, Volke-Sepulveda, Chávez-Cerda, Sibbett & Dholakia, 2002; Garcés-Chávez, McGloin, Padgett, Dultz, Schmitzer & Dholakia, 2003). The trapped micro-particles have been shown to rotate, owing to the transferred OAM and SAM, and their rotation rates have been measured (Garcés-Chávez, Volke-Sepulveda, Chávez-Cerda, Sibbett & Dholakia, 2002; Garcés-Chávez, McGloin, Padgett, Dultz, Schmitzer & Dholakia, 2003).

Bessel beams and in general nondiffracting beams can be generated using a variety of techniques, which apply refractive or diffractive optical elements. Durnin et al. (1987) reported the first experimental realization of a ZOBB by illuminating, with a collimated beam, an annular slit placed at the back focal plane of a positive lens. However, this method is very inefficient as most of the intensity of the illuminating beam is screened off by the aperture and only a small fraction propagates through the annular slit. The axicon, also called a conical lens, has been widely used to generate Bessel beams with much higher efficiencies since almost all the incident intensity is converted into the Bessel beam. Herman and Wiggins (1991) illuminated an axicon with a collimated Gaussian beam to generate a ZOBB while Scott and McArdle (1992) generated a similar beam using a rectangular aperture and an axicon illuminated likewise. Arlt and Dholakia (2000) obtained a HOBB using an axicon illuminated with a Laguerre-Gaussian beam with high conversion efficiencies of close to 100%. HOBBs have also been generated using a Mach-Zehnder interferometer in which the beam was decomposed into its constituent even and odd spatial components and then superimposed using the interferometer (López-Mariscal, Gutiérrez-Vega & Chávez-Cerda, 2004).

Computer generated holograms (CGHs) (Vasara, Turunen & Friberg, 1989; Paterson & Smith, 1996b) and axicon-type CGHs programmed on a spatial light modulator (SLM) (Davis, Guertin & Cottrell, 1993; Davis, Carcole & Cottrell, 1996) have been used to generate Bessel beams and their superpositions. Chávez-Cerda et al. (1996) showed that the superposition of HOBBs results in a periodically reconstructing beam with rotating and spiral wave features. In addition, Davis et al. (1996) showed that the intensity of the superposition of the HOBBs appeared as a circular pattern with a radius which depended on the order, m, of the Bessel function and that the intensity is azimuthally modulated resulting in $2m$ spots arranged on a circumference. Similar intensity patterns were obtained from the superpositions of HOBBs by Vasilyeu et al. (2009) using a SLM and a ring slit aperture (RSA). The aperture was divided into two rings of equal width but different radii and hence the superimposed beams had different wave vectors. The transverse intensity patterns of the superimposed beams depicted an interesting feature: the pattern rotated about the propagation axis as the beams propagated along the axis.

2.2.2 Rotating Zero-OAM Bessel Beams

Rotating Bessel beams can be generated by the superposition of two or more HOBBs. The superposition of HOBBs of the same order m (same azimuthal phase variation) but of opposite handedness results in Bessel beams with zero OAM but whose intensity of superposition rotate about the propagation axis as the beams propagate (Vasilyeu et al., 2009; Kotlyar, et al., 2007). Litvin, Dudley and Forbes (2011) measured the OAM density of such superpositions and found that while the global OAM is zero, the local OAM at various spatial locations is non-zero but changes radially across the beam and can be made to oscillate from positive to negative values by an appropriate choice of the parameters of the component beams. The angle of rotation of the intensity profile has been predicted theoretically (Vasilyeu et al., 2009; Davis et al., 1996) to be given by $\theta = \Delta kz/2|m|$ where Δk is the difference between the longitudinal wave vectors of the two superimposed beams and $|m|$ is the order (azimuthal index) of the beams. The rate of rotation of the intensity profile given by $d\theta/dz = \Delta k/2|m|$ is therefore a constant. The rotation rate, in radians per meter, varies linearly with the difference between the longitudinal wave-vectors of the superimposing beams but inversely with the order $|m|$ of the beams. Thus, by appropriately measuring the angle of rotation of the intensity pattern at various propagation distances, it is possible to determine the rotation rate of the intensity profile and to investigate the effect of changing the values of Δk and order m on the rotation rate. The method by which to execute such a study is outlined in the methodology section of this thesis.

2.2.3 Helicon Rotating Bessel Beams

Helicon beams have an intensity pattern which rotates at a constant rate about the optical axis but is otherwise unchanged and their lines of constant intensity trace out helices about the optical axis (Paterson & Smith, 1996a). They consist of superpositions of HOBBs of different orders (unequal topological charges) and hence carry orbital angular momentum owing to a net azimuthal variation. Helicon beams have been realized theoretically and experimentally and the theoretical conditions necessary for their rotation have been studied (Paterson & Smith, 1996a; Kotlyar et al., 2007). The rate of rotation of the intensity profile is given by $d\theta/dz = \Delta k/\Delta m$ where $\Delta m = m_1 - m_2$. Thus, it is possible to achieve high rotation rates with Helicon beams obtained from superpositions of HOBBs with large values of m_1 and m_2 provided Δm is chosen to be small. The approach followed to determine the rotation rates is discussed in the methodology section (chapter 4) of this thesis.

2.3 Rotating Laguerre-Gaussian Beams

Laguerre-Gaussian beams (LGBs) are higher order solutions of the paraxial wave equation with cylindrical symmetry about their axes of propagation. LGBs are characterized by two indices l and p, which are the azimuthal and radial mode numbers respectively. The index l is an integer which expresses the phase singularity order on the beam axis and hence characterizing the beam as an optical vortex with topological charge $+l$ and $-l$, depending on the rotation direction of its helical wavefront (Topuzoski & Janicijevic, 2009). The index p is a positive integer. If $l = 0$ and $p = 0$ then a Gaussian beam is represented. The intensity profile of a LGB consists of alternate bright and dark rings surrounding a dark or bright central spot. If $l \neq 0$ in the transverse cross-section of the beam, then the transverse intensity profile consists of (p+1) bright rings surrounding a dark central spot whereas if $l = 0$, p bright rings surround a central bright spot (Topuzoski & Janicijevic, 2009).

The superposition of two or more LG modes with different optical frequencies can result in rotating LGBs but only if certain conditions, as discussed by Kotlyar et al. (1997), are satisfied. Unlike for rotating Bessel beams the angular velocity of rotation of the intensity profile of rotating LGBs decreases with propagation distance.

2.4 Spiralling and Spiral-type Beams

Spiralling beams are a special case of Helicon beams and have an intensity pattern that is laterally displaced with respect to the optical axis and rotates as a whole around the axis as the beams propagate along it (Jarutis et al., 2009; Matijošius et al., 2010; Sun et al., 2011; Anguiano-Morales et al., 2011. Spiral-type beams have been demonstrated, theoretically and experimentally as modes of a ring resonator with a beam rotator (Abramochkin & Volostnikov, 1996) and have been shown to correspond to the quantum-mechanical ground states of a charged particle in a uniform magnetic field (Abramochkin et al., 1997). Spiralling ZOBB has been generated by illuminating, with a Gaussian beam, a combination of a conventional axicon and a phase hologram which introduces an equal phase shift of spiral form on the beam (Pääkkönen et al., 1998; Peatross & Ware, 2011). Spiralling HOBBs of arbitrary order have been realized experimentally by illuminating an aperture axicon and a hologram with a single-ringed Laguerre-Gaussian beam (Sun et al., 2011). The spiralling HOBB so produced rotated around the propagation axis with a hollow centre. Recently, a spiral wave was generated by illuminating a combination of a lens and an amplitude mask which consisted of two incomplete annular slits of equal radii but with one-half slightly displaced with respect to the other (Anguiano-Morales et al., 2011).

2.5 Generation of Rotating Bessel Beams

Rotating Bessel beams (RBBs) have been generated using a variety of techniques. Davis et al. (1996) used a binary phase diffractive optical element (DOE) written on a magneto-optic spatial light modulator (MOSLM) while Kotlyar et al. (2007) used a similar DOE written on a liquid crystal SLM to generate rotating zero OAM Bessel beams. Recently, spatial light modulators (SLMs) with imprinted digital holograms have been used. Vasilyeu et al. (2009) modified the method used by Durnin et al. (1987) by using a ring slit aperture, divided into two slits of equal width but different radii, placed at the focal plane of a positive lens. The azimuthal phase in each slit varied from 0 to 2π equal times but with opposite handedness. The HOBB generated by illuminating a liquid crystal SLM imprinted with an appropriate phase hologram was incident on the ring slit aperture.

Helicon beams have been experimentally generated using a single binary phase diffractive axicon element (Paterson & Smith, 1996a). This method of generation of Helicon beams relied on the use of odd-numbered conical diffraction orders of a binary phase diffractive optical element, and as such only a limited set of rotating Bessel beams could be generated. Pääkönen et al. (1998) used a complex spatial filter, which is a diffractive optical element that modulated both the amplitude and the phase of the incident field according to some desired amplitude transmittance. They found that if the amplitude information of the superimposed fields is completely neglected, it does not in general lead to good results for rotating beams. This thesis reports, in the methodology section, an appropriate and effective technique for generating rotating zero OAM and Helicon beams and for measuring their rotation rates. In addition, the method is modified to investigate the propagation dynamics of these beams beyond partial and total obstructions set on- and off-axis.

CHAPTER THREE

THEORY

3.1 Introduction

Rotating optical fields (ROFs) can be treated as scalar or electromagnetic (vector) fields. In scalar treatment, only the energy density (intensity) of ROFs is considered and ROFs have uniformly rotating intensity distributions and propagation-invariant radial scales. However, in the vectorial approach the state of polarization of the field is considered in addition to the energy density of the field. Consequently, the conditions for the rotation of the field are different for scalar and electromagnetic ROFs (Tervo & Turunen, 2001).

Scalar ROFs are like propagation-invariant and self-imaging fields since the intensity distribution, including its transverse scale, at any transverse plane z = c, where c is a real constant, is exactly the same as at z = 0, except for a rotation by an angle $\phi = 2\pi z / z_T$, where z_T is a characteristic distance, called the Talbot distance, over which the intensity distribution of the field undergoes a rotation of 2π radians (Pääkönen et al., 1998).

Although the scalar theory does not describe completely the nature of ROFs, it is often sufficient for linearly polarized electromagnetic fields in many situations. This is because, although the electric field of a light wave is a vector, the wave field is scalar and with paraxial approximation, the polarization is almost uniform near the axis of a laser beam with only one component for which the scalar approach is a good approximation. In addition, the vector field can always be obtained once the scalar theory of a particular optical field has been found (Weiner & Ho, 2003). In the following section, we present the scalar theory of ROFs only since it is adequate to capture the key aspects of this study.

3.2 Scalar Rotating Optical Fields

Durnin and co-workers (Durnin, 1987; Durnin et al., 1987) showed that there exists a family of propagation-invariant optical beams that are exact non-singular solutions of the wave equation (equation 1.2). Such scalar optical beams are not subject to transverse spreading, have finite energy density and have sharply defined intensity distributions. These beams can be expressed mathematically, in the form first presented by Whittaker and Watson (1927), as;

$$E(x,y,z\geq 0,t)=\exp[i(k_z z-wt)]\int_0^{2\pi}A(\theta)\exp[ik_r(x\cos\theta+y\sin\theta)]d\theta\,, \qquad (3.1)$$

where $k_z^2+k_r^2=k^2=(\omega/c)^2=(2\pi/\lambda)^2$ in which k is the wave number, ω is the angular frequency, $c=3.0\times 10^8 m/s$ is the speed of light in free space and λ is the wavelength of the beam. The quantity $A(\theta)$ is the complex angular spectrum of the field. The optical intensity of the field, which is defined by equation (3.1) does not depend on the coordinate z and hence obeys the condition (Durnin, 1987);

$$|E(x,y,z>0,t)|^2 = |E(x,y,z=0,t)|^2 . \tag{3.2}$$

The intensity distribution is independent of the coordinate along the propagation axis (the z - axis) except for a linear rotation as the beam propagates. This implies that the intensity distribution at the transverse plane $z>0$ is exactly the same as at the plane $z=0$. In cylindrical coordinates $\rho=(r,\theta,z)$ and $k=(k_r,k_\theta,k_z)$, the angular spectrum of the field in equation (3.1) is given by (Tervo & Turunen, 2001),

$$E(r,\theta,z)=\exp(ik_z z)\int_0^\infty\int_0^{2\pi} k_r A(k_r,k_\theta)\exp[ik_r \cos(\theta-k_\theta)\,dk_r dk_\theta, \tag{3.3}$$

where r, θ and z are the radial, azimuthal and longitudinal coordinates respectively and k_r, k_θ and k_z are the wave vectors in the three directions respectively. The propagation-invariance condition (equation 3.2) can then be rewritten, to define the rotation of the intensity profile, as (López-Mariscal, 2003);

$$|E(r,\theta,0)|^2 = |\exp[i\eta(r,\theta,\Delta z)]E(r,\theta+\varepsilon\Delta z, z+\Delta z)|^2 , \tag{3.4}$$

where $\varepsilon = 2\pi/\Delta z$ is a constant that specifies the direction of rotation and the longitudinal period of the field, η is an arbitrary real function and Δz is the change in the propagation distance. Applying equation (3.4) on equation (3.3) gives the angular spectrum as (Tervo & Turunen, 2001);

$$\sum_{m=-\infty}^{\infty}\int_0^\infty a_m(k_r)\mathrm{J}_m(k_r r)\exp(im\theta)\left\{\exp\left[i\eta(r,\theta,\Delta z)\right]-\exp\left[i(m\varepsilon+k_z)\Delta z\right]\right\}\mathrm{d}k_r = 0 , \tag{3.5}$$

where $\mathrm{J}_m(k_r r)$ is the Bessel function of the first kind of order *m* and,

$$a_m(k_r) = i^m k_r \int_0^{2\pi} A(k_r, k_\theta) \exp(-imk_\theta)\, dk_\theta \tag{3.6}$$

is obtained by applying the Jacobi-Anger expansion (Arfken & Weber, 2001).

Since equation (3.5) must hold for all r and θ then the integrand must vanish, giving

$$\eta(r, \theta, \Delta z) = \eta(\Delta z) = (m\varepsilon + k_z)\Delta z + 2\pi n, \tag{3.7}$$

where *n* is an integer. Since the phase change $\eta(\Delta z)$ must be continuous and $\eta(0) = 0$ then $n = 0$. Thus k_z assumes only discrete values given by $k_{zm} = k_{zo} - m\varepsilon$ where $k_{zo} \le k$ is a positive real constant (Tervo & Turunen, 2001). The angular spectrum of the field now consists of a discrete set of concentric rings, called Montgomery's rings (Montgomery, 1967; Saastamoinen, Tervo, Vahimaa & Turunen, 2004) with radii

$$k_r = \left(k^2 - k_{zm}^2\right)^{\frac{1}{2}}. \tag{3.8}$$

Equation (3.8) implies that the transverse components of the wave vectors must be confined to the set of Montgomery's rings. These are a set of concentric rings of well-defined radii representing the spatial frequencies within which the angular spectrum of longitudinally periodic fields is confined (Montgomery, 1967). The width of the rings decreases as the order of the field increases. For a set, *M*, of allowed values of *m* for which $0 \le k_{zm} \le k$ and $a_m \equiv a_m(k_{\rho m})$, the field expression becomes (Tervo & Turunen, 2001);

$$E(r,\theta,z)=\sum_{m=1}^{M}a_m J_m(k_r r)\exp[i(m\theta+k_{zm}z)]\,. \tag{3.9}$$

If $k_{zm}=k$, then it follows from (3.8) that $k_r=0$ and hence the angular spectrum represents that of a plane wave. If $k_{zm}=0$, then the field does not propagate in the z-direction. However, if the k_z values do not belong to a discrete set, then the field describes a non-periodic rotating beam. The distance over which the field completes a full rotation is defined by equation (3.4) and is given by $z_R=2\pi m/k_z$.

3.3 Bessel Beam Modes

The integrand in equation (3.1) can be expressed as;

$$V(x,y)=\int_0^{2\pi}A(\theta)\exp\left[ik_r\left(x\cos\theta+y\sin\theta\right)\right]d\theta, \tag{3.10}$$

where all the symbols are as defined earlier. Equation (3.10) represents a superposition of homogeneous plane waves, of wave number k_r and amplitude $A(\theta)$, which propagate in all directions in the *x-y* plane (Turunen & Friberg, 2009). The Fourier expansion of the amplitude $A(\theta)$ can be expressed as;

$$A(\theta)=\sum_{m=-\infty}^{+\infty}a_m\exp(im\theta), \tag{3.11}$$

where the Fourier coefficients a_m are defined by

$$a_m=\frac{1}{2\pi}\int_0^{2\pi}A(\theta)\exp(-im\theta)d\theta\,. \tag{3.12}$$

In polar coordinates (r,θ) and employing the Bessel function identity

$$J_m(x)=\frac{i^{-m}}{2\pi}\int_0^{2\pi}\exp[i(m\theta+x\cos\theta)]d\theta\,, \tag{3.13}$$

where J_m is the Bessel function of the first kind and order *m*. By letting $C_m = 2\pi i^m a_m$, then the general expression for propagation-invariant optical fields (equation 3.1) can be expressed as a superposition of Bessel functions as (Chávez-Cerda et al., 1996);

$$E\left(r,\theta,z\right)=\exp\left(ik_z z\right)\sum_{m=-\infty}^{+\infty} C_m J_m\left(k_r r\right)\exp(im\theta)\,, \tag{3.14}$$

where the time-dependence in equation (3.1) has been omitted. In the simplest special case, $C_m = 0$ for all but one value of *m* and equation (3.14) then represents Bessel field modes with rotationally symmetric transverse intensity distributions of the form $I(r)\propto J_m^2(k_r r)$ (Turunen & Friberg, 2009). The complex amplitude of the transverse electric field of the Bessel field mode is obtained, from equation (3.14), as (McGloin & Dholakia, 2005);

$$E\left(r,\theta,z\right)=J_m\left(k_r r\right)\exp[i\left(k_z z+m\theta\right)]\,. \tag{3.15}$$

These free-space Bessel modes can be generated using Bessel filters synthesized on a computer by digital holographic methods (Valyaev & Krivoshiykov, 1989).

3.3.1 Fundamental Bessel Field Mode

The fundamental Bessel field mode, also called the zero-order Bessel beam (ZOBB), is obtained from equation (3.15) by letting the azimuthal order *m* be zero. Thus;

$$E(r,\theta,z) = J_0(k_r r)\exp(ik_z z) \tag{3.16}$$

with a transverse intensity distribution $I(r) \propto J_0^2(k_r r)$ and a binary-valued (0 or π radians) phase distribution (Turunen & Friberg, 2009). The intensity distribution exhibits a narrow axial peak surrounded by a set of alternate dark and bright rings concentric about the axis of the beam. The intensity and phase distributions of the ZOBB are shown in the theoretical plots in figure 3.1. The full width at half maximum (FWHM) of the central peak is $r \approx 2.25/k_r$ and the first zero is located at $r \approx 2.405/k_r$ (Turunen & Friberg, 2009).

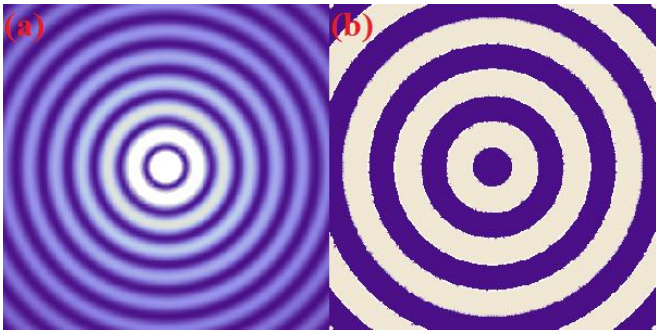

Figure 3.1: Intensity (a) and phase plots (b) of a zero-order Bessel beam. The alternate white and dark blue annular areas in (b) represent phase jumps from 0 to 2π.

3.3.2 Higher-order Bessel Field Modes

High-order Bessel Beams (HOBBs) are described by higher order ($m \geq 1$) Bessel functions and their transverse intensity distributions, $J_m^2(k_r r)$ have a singularity (intensity null) on the beam axis and hence have a non-diffracting dark core rather than a bright one (McGloin & Dholakia, 2005). The transverse electric field is represented by equation (3.15), where $k_r = k \sin\alpha$ and $k_z = k\cos\alpha$ in which α is the half angle of the cone of wave vectors constituting the Bessel beam and is given by $\alpha = \tan^{-1}\left(k_r/k_z\right)$. The phase of a HOBB varies continuously from 0 to 2π a total of m times in one azimuthal revolution and consequently the field possesses orbital angular momentum and hence exhibits an azimuthally spiral-like phase profile with a vortex at the z-axis. The size of the dark core increases with increase in the order m of the HOBBs. The intensity and phase distributions of various HOBBs are shown in figure 3.2.

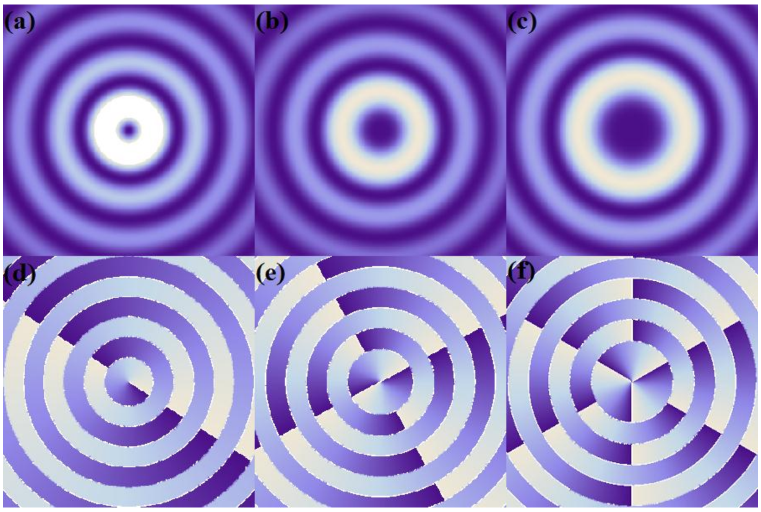

Figure 3.2: The intensity (top row) and phase distributions (bottom row) of higher-order Bessel beams of azimuthal orders *m* = 1 (‘a’ and ‘d’), *m* = 2 (‘b’ and ‘e’) and *m* = 3 (‘c’ and ‘f’).

3.3.3 Rotating Bessel Fields

Bessel beams can be considered as a set of plane waves propagating on a cone, such that each plane wave undergoes the same phase shift $k_z\Delta z$ over a given propagating distance Δz (McGloin & Dholakia, 2005). The angular spectrum of a Bessel field is a ring in k-space and hence a Fourier transform of the ring results in a Bessel beam in configuration space. This is the basis of the first experimental generation of Bessel beams by Durnin et al. (1987). The superposition of two Bessel fields can therefore be considered as the interference of two sets of waves, with each set traversing a cone of half-angle whose magnitude is determined by the radial and longitudinal wave-vectors of the propagating waves. Consider the superposition of two HOBBs of orders equal in magnitude but of opposite topological charges, that is, of orders m and $-m$ respectively. Let the two beams propagate with slightly differing wave-vectors. Figure 3.3 shows the digitally generated annular rings used to superimpose the Bessel fields and the geometrical illustration of the interaction of the two interfering Bessel beams. The physical ring slit aperture is replaced by the digital annular rings (shown on the left) with non-zero azimuthal phase variation. The shaded region beyond the Fourier lens, of focal length f, is the invariance region.

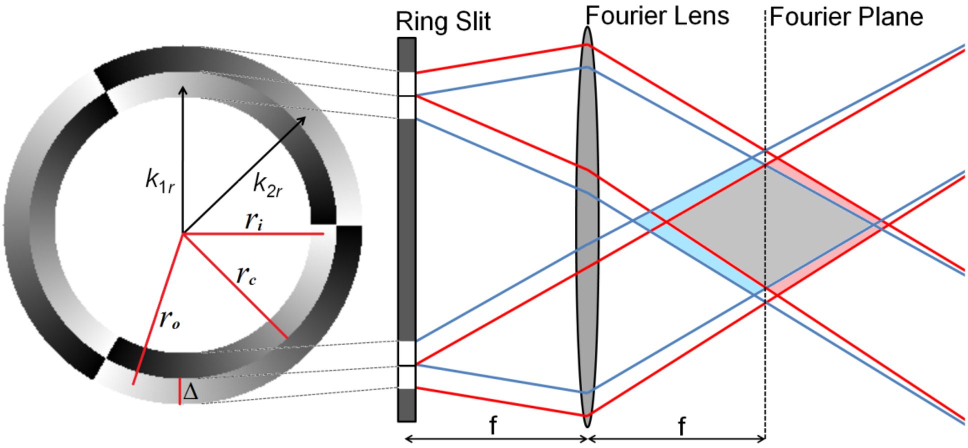

Figure 3.3: A geometrical illustration of the formation of rotating Bessel beams through the superposition of higher-order Bessel beams.

The transmission function of the ring slit aperture is

$$t(r,\theta)=\begin{cases}\exp(im\theta) & r_i-\frac{\Delta}{2}\le r_c\le r_i+\frac{\Delta}{2}\\ \exp(-im\theta) & r_o-\frac{\Delta}{2}\le r_c\le r_o+\frac{\Delta}{2}\\ 0 & \text{elsewhere,}\end{cases} \qquad (3.17)$$

where r_i and r_o are the radii of the two annular rings respectively and Δ is the width of each ring-slit (see figure 3.3), which were chosen to be equal. The far-field of the ring-slit aperture is given by the Kirchhoff-Huygens diffraction integral as (Vasilyeu et al., 2009);

$$E(r,\theta,z)=\frac{-i}{\lambda z}\int_0^{2\pi}\int_{r_i-\frac{\Delta}{2}}^{r_o+\frac{\Delta}{2}} t(r,\theta)\exp\left[i\left(1-\frac{z}{f}\right)r_1^2\right]\exp\left[-i\frac{krr_1}{f}\cos\left(\theta_1-\theta\right)\right]r_1dr_1d\theta_1 .$$

(3.18)

The field contribution from the two ring-slits, in the far field, is given, respectively by

$$E_m(r,\theta,z) = -\frac{ik}{f}\int_{r_i-\frac{\Delta}{2}}^{r_i+\frac{\Delta}{2}} i^m \exp(im\theta) J_m\left(\frac{krr_1}{f}\right)\exp\left[-\frac{r_1^2}{\omega^2} + i\frac{kr_1^2}{2f}\left(1-\frac{z}{f}\right)\right] r_1 dr_1, \quad (3.19)$$

and

$$E_{-m}(r,\theta,z) = -\frac{ik}{f}\int_{r_o-\frac{\Delta}{2}}^{r_o+\frac{\Delta}{2}} i^{-m} \exp(-im\theta) J_{-m}\left(\frac{krr_1}{f}\right)\exp\left[-\frac{r_1^2}{\omega^2} + i\frac{kr_1^2}{2f}\left(1-\frac{z}{f}\right)\right] r_1 dr_1. \quad (3.20)$$

Hence the total field, in the far field, due to the two ring-slits is simply the sum of the individual contributions from slits, which on simplification gives

$$E(r,\theta,z) = J_m(k_{1r}r)\exp\left[i(k_{1z}z + m\theta)\right] + J_{-m}(k_{2r}r)\exp\left[i(k_{2z}z - m\theta)\right], \qquad (3.21)$$

in which the approximation $k_r = k\sin\alpha = k\sin\left(r_c/f\right) \simeq kr_c/f$ has been applied. k_{1r}, k_{2r} and k_{1z}, k_{2z} are, respectively, the radial and longitudinal wave-vectors of the two beams. The intensity of superposition, which is given by $I(r,\theta,z) = E(r,\theta,z)E^*(r,\theta,z)$ is directly obtained from equation (3.21) as

$$I_{m,-m}(r,\theta,z) \propto J_m^2(k_{1r}r) + J_{-m}^2(k_{2r}r) + 2J_m(k_{1r}r)J_{-m}(k_{2r}r)\cos(\Delta kz - 2m\theta), \quad (3.22)$$

where

$$\Delta k = k_{2z} - k_{1z} = \frac{2\pi}{\lambda}\left|\cos\left(\frac{r_o}{f}\right) - \cos\left(\frac{r_i}{f}\right)\right|, \qquad (3.23)$$

and r_i and r_o are the radii of the inner and outer annular rings respectively and f is the focal length of the Fourier lens. One can simplify equation (3.22) by making the approximation that $k_{1r} \sim k_{2r}$ and hence $J_m(k_{1r}r) \sim J_m(k_{2r}r) = J_m(k_r r)$ and applying the

Bessel function identity $J_{-m}(k_{2r}r) = (-1)^m J_m(k_{2r}r)$, the intensity of the superposition $I_{m,-m}$ is proportional to

$$J_m^2(k_r r)\left[1 + \cos\left(\Delta kz - 2m\theta\right)\right], \tag{3.24}$$

where k_r is the average radial wave-vector of the two fields. If the longitudinal wave-vectors of the superimposing beams are equal, $\Delta k = 0$ and hence

$$I_{m,-m} \propto 2J_m^2(k_r r)\cos^2(m\theta)\,. \tag{3.25}$$

With this approximation one can readily note from equation (3.25) that the intensity of the superposition field is modulated in the azimuthal co-ordinate by the function $\cos^2(m\theta)$. From the properties of the cosine function, it follows that the number of intensity maxima in the intensity of superposition is twice the order m of the beams. Thus the superposition of an m^{th} order Bessel beam with its mirror image ($-m^{\text{th}}$ order Bessel beam) produces a resultant intensity pattern having $2|m|$ lobes, or ‘petals’, arranged on the circumference of the set of rings defined by the enveloping Bessel function (radial only).

The intensity profile of the resultant field rotates about the azimuthal coordinate as the beam propagates along the z direction. To see how the rotation arises, consider equation (3.24): the term in square brackets determines the angular position of the resultant lobes along the circumference of the Bessel rings. Since for any two superimposed beams, Δk and order m are constants, the azimuthal coordinate, which gives the angular position of the petals changes with the propagation distance of the beam and hence the entire intensity profile rotates about the common centroid, the centre of the dark core. The angle of rotation has been predicted (Vasilyeu et al., 2009; Kotlyar et al., 2007] to be given by

$$\theta = \frac{\Delta k}{2m} z\,, \tag{3.26a}$$

and the rate of rotation of the intensity profile, given by

$$\frac{d\theta}{dz} = \frac{\Delta k}{2m}\,, \tag{3.26b}$$

is a constant. The rotation rate, in radians per meter, varies linearly with the difference between the longitudinal wave numbers of the superimposing beams but inversely with the order |*m*| of the beams. Thus, by appropriately measuring the angle of rotation of the intensity pattern at various propagation distances, it is possible to determine the rotation rate of the intensity profile and to investigate the effect of changing the values of *Δk* and order *m* on the rotation rate. The method by which the investigation of the rotation rate was done is outlined in chapter 4 and the results are presented and discussed in chapter 5 of this thesis.

For Helicon RBBs, which are superpositions of two HOBBs with distinct orders, m_1 and m_2, the complex amplitude of the resultant field is

$$E_{m_1,m_2}(r,\theta,z) = J_{m_1}(k_{1r}r)\exp\left[i\left(k_{1z}z + m_1\theta\right)\right] + J_{m_2}(k_{2r}r)\exp\left[i\left(k_{2z}z + m_2\theta\right)\right]. \tag{3.27}$$

The intensity of the superposition is given by the proportionality

$$I_{m_1,m_2}(r,\theta,z) \propto J_{m_1}^2(k_{1r}r) + J_{m_2}^2(k_{2r}r) + 2J_{m_1}(k_{1r}r)J_{m_2}(k_{2r}r)\cos[\Delta kz + (\Delta m)\theta], \quad (3.28)$$

where $\Delta m = |m_1 - m_2|$, the absolute difference between the orders of the two beams. The rate of rotation of the intensity profile is given, from equation (3.28) by

$$\frac{d\theta}{dz} = \frac{\Delta k}{\Delta m}. \quad (3.29)$$

From this expression of rotation rate, it follows that it is possible to achieve high rotation rates with Helicon beams obtained from superpositions of HOBBs with large values of m_1 and m_2 provided that Δm is chosen to be small. However, high rotation rates are only possible with zero global OAM RBBs of lower m values. If the angular displacement of a given petal in the intensity pattern is measured at various distances along the propagation axis and plotted as a function of the propagation distance, a linear variation is predicted (by equation 3.26a) whose slope gives the rate of rotation of the intensity profile of the Helicon beam. Similarly, the investigation of the rotation rates of Helicon RBBs is presented in chapter 4 and the results are discussed in chapter 5 of this thesis.

3.3.4 Self-reconstruction of Bessel Beams

Self-reconstruction is the regeneration of electromagnetic energy and hence the intensity profile of a beam (in particular a Bessel beam) after propagating past an opaque obstacle placed in its path. The Bessel beam reconstructs its amplitude and phase beyond the obstruction, provided that the spatial extent of the beam is larger than that of the obstacle. The minimum distance beyond the obstacle at which the beam reforms its intensity structure is called the reconstruction distance, $z_{\min}$, and is given by (Litvin et al., 2009)

$$z_{\min} = D\frac{k_z}{k_r} = \frac{D}{2\tan\alpha}, \tag{3.30}$$

where D is the diameter of the obstacle and α, measured in radians, is the half-angle of the cone traversed by the wave vectors of the beam. For the generation of Bessel beams using an annular slit and a positive lens, $\alpha = r/f$, where r is the radius of the annular slit and f is the focal length of the lens. If an axicon is used, $\alpha = (n-1)\gamma$, where n is the refractive index of the axicon material and γ is its opening angle. The reconstruction distance is shown in figure 3.4 which illustrates geometrically the reconstruction effect.

The reconstruction property has been explained in detail using the conical wave approach (Anguiano-Morales et al., 2007), which considers the cone of wave vectors constituting the Bessel beams as consisting of two conical waves (CWs), an incoming conical wave (ICW) and the other, an outgoing conical wave (OCW). These CWs can be represented by Hankel functions of the second kind, $H_0^{(2)}(k_r r)$, and of the first kind, $H_0^{(1)}(k_r r)$, respectively (Chávez-Cerda, 1999);

$$H_0^{(1)}(k_r r)\exp(ik_z z) = \left[J_0(k_r r) + iN(k_r r)\right]\exp(ik_z z), \tag{3.31}$$

$$H_0^{(2)}(k_r r)\exp(ik_z z) = \left[J_0(k_r r) - iN(k_r r)\right]\exp(ik_z z), \tag{3.32}$$

where $J_0(k_r r)$ and $N(k_r r)$ are the zero-order Bessel and Newman functions respectively. The ICW generates the OCW and on traversing the propagation axis interferes with it to reconstruct the Bessel beam.

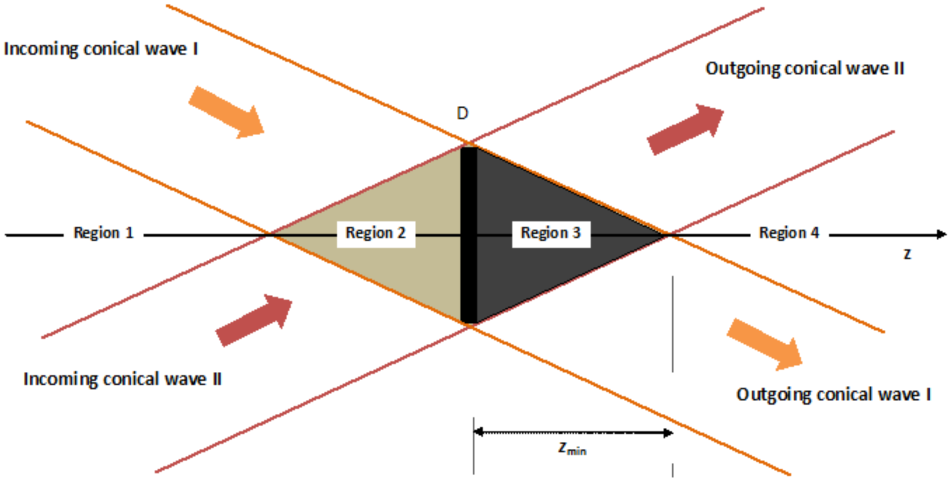

Figure 3.4: Geometrical illustration of self-reconstruction.

The incoming conical waves interact in region 2 and are blocked by the obstacle which casts a shadow into region 3. However, the parts of the incoming waves that are not blocked by the obstruction proceed into and interact in region 4. The length of the shadow region measured along the propagation axis, z, and beyond the obstacle is the reconstruction distance, z_{min}, beyond which the Bessel beam reconstructs. Although in a Bessel beam, locally, light travels parallel to the propagation axis, the energy flux follows the direction determined by the cone of wave vectors (Anguiano-Morales et al., 2007). Thus reconstruction occurs as a result of the parts of the conical waves that are not obstructed by the obstacle. When the obstruction is circular and placed on-axis, the edge waves create a diffracting Bessel intensity pattern, which appears as a bright spot at the centre and is called the Poisson or Arago spot (Lucke, 2006).

3.4 Spatial Light Modulators

The performance of optical information processing and data storage systems has been greatly enhanced by the discovery of the spatial light modulator. A spatial light modulator (SLM) is an electro-optic device that is capable of converting data in electronic or in incoherent optical form into spatially modulated coherent optical signals (Goodman, 1996). Since a SLM is digitally programmable, it can be used to impose a given set of information on an optical wave by spatially modulating its amplitude distribution (and hence its intensity) or its phase distribution or both. In principle, a SLM is a device which allows the user to change the phase, intensity or polarisation of a light field in an arbitrary way. It can hence serve the purpose of interfacing in many optical information processing systems to provide input to and to extract information from the system (Goodman, 1996). Generally, the performance requirements for a good SLM include flat-panel, light weight, low driving voltages and low power consumption (Yeh, 1993)]. In addition, high fill factor and high diffraction efficiency are essential performance parameters.

There are several SLM technologies but the most important ones include liquid crystal (LC), magneto-optic (MO), deformable mirror (DM), micro-channel plate (MCP) and multiple-quantum-well (MQW) SLMs (Goodman, 1996). In the section that follows, the basic construction and operation of liquid crystal spatial light modulators (LCSLMs) is presented briefly since the SLM applied in this investigation is the LC type.

3.4.1 Liquid Crystals

Liquid crystals (LCs) are technologically important electro-optical materials owing to their many unique physical and electro-optical properties. In addition to the solid and liquid phases, liquid crystals exhibit intermediate phases called the liquid crystal mesophase in which they flow like liquids yet possess some physical properties of crystals (De Gennes, 1974). There are several types of liquid crystals but the most common ones are thermotropic, lyotropic and polymeric LCs. Thermotropic LCs are of three types: nematics, cholesterics and smectics and are the most widely used and studied in terms of their linear and non-linear optical and electro-optical properties.

LCs exhibit extraordinarily large optical nonlinearities over the entire visible-near infrared-infrared spectral region. These nonlinear optical and electro-optical phenomena include optical phase conjugation, degenerate and non-degenerate wave mixing, self- focusing and self-phase modulation, optical parametric amplification and photorefractive effect (Khoo, 1995). Due to these nonlinear effects, liquid crystals have found extensive applications in the electronic display industry, information processing and storage, spatial light modulation and communication. Owing to their high optical anisotropy (different indices of refraction for different axes of the molecule) LCs may be used as phase, polarisation or intensity modulators. It is this optical behaviour, the change in the optical properties of the LC due to a reorientation of its director as a result of the application of an electric or optical field that is exploited in spatial light modulators. When a field is applied, the LC molecules reorient depending on the direction of the field. When the direction of the field is reversed the direction of the molecules undergo a rotation, changing the polarization characteristics of the LC (Khoo, 1995).

3.4.2 Liquid Crystal SLMs

There are several types of LCs that have been applied in SLM manufacture, but the most commonly used are the ferroelectric and nematic LCs (Goodman, 1996). Ferroelectric SLMs have shorter switching times but they often have a binary output and are sensitive to shock and vibration. Although nematic SLMs are slower, they have a greater dynamic range and better amplitude uniformity. They are therefore often used for applications where 2π phase only modulation is necessary.

LCSLMs operate on the principle of electrically controlled birefringence. The operation is based on ‘the reorientation of the director axis of the LC material by an applied field (electric or optical), which causes a change in the refractive index of the LC material. The field induces a dipole in the LC molecules, which interacts with the field to produce a torque that rotates the molecules. This manifests itself as a spatially dependent phase change to any light travelling through the liquid crystal. LCSLMs may be addressed in two ways: using an electric field applied via electrodes on a silicon wafer (electrically addressed SLM, EASLM) or optically, using an incident light focussed on a photosensitive material sandwiched between two transparent electrodes (optically addressed SLM, OASLM) (Barbier & Moddel, 1997).

For a reflective EASLM, polarized light reaches the LC via the transparent electrode, is reflected off the shiny pixel electrodes but modulated by the orientation impinged on the LC by electric field applied on the pixels. Figure 3.5 illustrates the construction of an EA LCSLM. Examples of EA LCSLMs include those manufactured by Boulder Nonlinear Systems (BNS) (2010) and HoloEye Photonics (2010). Figure 3.6 shows a picture of an EA LCSLM from Holoeye Photonics.

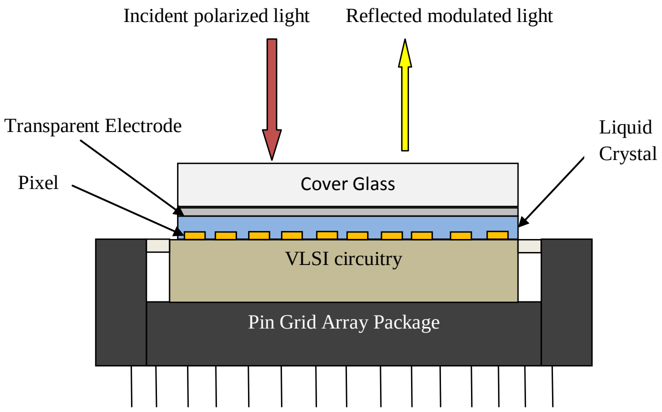

Figure 3.5: A cross-section of the construction of a typical reflective EA LCSLM.

Figure 3.6: A picture of a reflective EA LCSLM manufactured by Holoeye Photonics (Holoeye Photonics, 2010). In the foreground is the LCD in which the whitish rectangular region is the active sensor area of the SLM. The black unit in the background comprises the electronics unit.

Electrically addressed LCSLMs have fast update rates and high resolution but they suffer from poor surface flatness, produce pixelation artefacts and often create poor phase modulation due mainly to the type of liquid crystal used (Preece, 2011). In optically addressed LCSLMs, the input optical beam (the writing beam) activates photo-receptors in a photoconductive layer to generate suitable charge distribution (Barbier & Moddel, 1997). Figure 3.7 shows a reflective optically addressed LCSLM and the beam geometry. In the transmissive mode, the readout and writing beams impinge on the LC layer from the same side and the transmitted readout beam is the modulated signal. The dielectric reflector is excluded. OA LCSLMs are primarily manufactured by Hamamatsu (2010), have good optical flatness owing to the lack of electronics and can create more than 2π phase changes. However, they are slower to update and require intensity modulation (Preece, 2011).

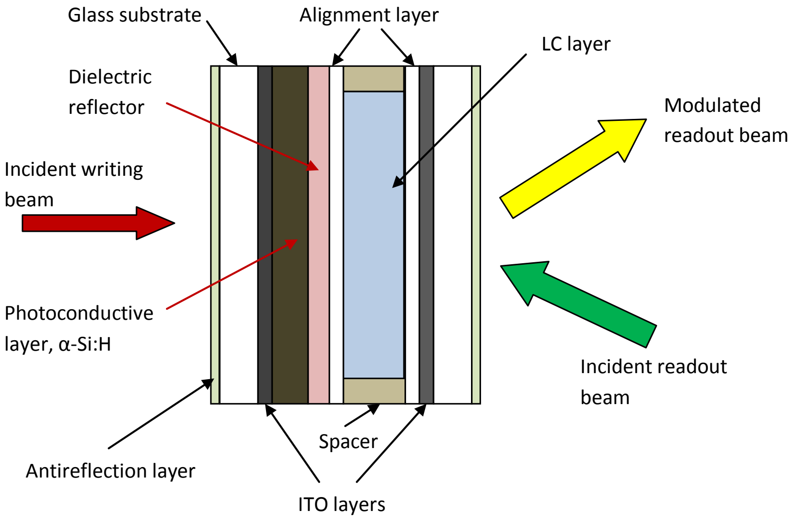

Figure 3.7: A cross-section of the construction of a typical reflective OA LCSLM.

The effectiveness of an SLM depends on its ability to produce a specific amplitude and/or phase modulation independently in each addressable pixel. For SLMs based on liquid crystals, the actual modulation that can be achieved depends on the polarizations of the incident and transmitted beams (Ferreira & Belsley, 2010). Since the actual modulation in relation to a given beam's polarization is not known in advance, then any SLM must be characterized for the particular wavelength and polarization of the beam. The purpose of performing the calibration is to verify that for one's working wavelength a phase shift from 0 to 2π is achieved over all the 256 addressable phase (or grey) levels. If the phase shift for the assigned grey-levels does not fall in the range from 0 to 2π then the voltages applied to the electrodes of the pixels need to be adjusted appropriately so as to achieve the correct phase modulation (Dudley, 2011).

3.4.3 Factors affecting the efficiency of a LCSLM

The efficiency of a LCSLM is affected by several factors such as diffraction efficiency, fill factor, reflectivity, angle of incidence, temperature and thickness of LC layer. In addition, there are several performance characteristics of an SLM, which include space bandwidth product (SBP), response time, contrast, dynamic range, sensitivity, and spectral response. These characteristics have been discussed in good detail by Neff, Athale and Lee (1990). As examples, only diffraction efficiency and fill factor are discussed briefly in this section.

Diffraction Efficiency

Diffraction efficiency is the ratio of the intensity diffracted into the first order to the incident optical intensity (Goodman, 1996). Ideally, an SLM modulates the light incident on it according to the phase digitally imprinted on it, such that the reflected or transmitted light undergoes the desired phase change. However, in practice, fabrication errors may lead to phase errors in the uneven etch depths or uneven etch areas resulting in the appearance of the zero order, for most commercially available SLMs (Wong & Chen, 2008). Thus a good fraction of the incident light either remains unchanged or is changed in way that is undesirable (Preece, 2011). Diffraction efficiency of the SLM then gives a measure of that proportion of the incident light whose phase has been modulated in a desirable way, that is, according to the phase imprinted on the SLM.

Fill Factor

Fill factor is the ratio of the active diffracting area of the SLM to the total contiguous area occupied by the array of pixels. The presence and sizes of gaps between the charged pixels in EA LCSLMs introduces undesirable diffraction effects. Since the gaps are not charged they are regions of zero field and hence will cause diffraction of incident light depending on their relative sizes. This effect reduces the overall efficiency of the SLM by throwing a certain amount of reflected light into unwanted diffraction orders or even leaving some of the reflected light unaltered by the SLM. In addition, polarization coupling may occur owing to the improperly modulated regions between electrodes and the director deformations may propagate elastically into the interpixel region causing undesired phase and amplitude distortions of the propagating light (Stockley, Subacius & Serati, 1999).

3.4.4 Modulation Transfer Function of a LCSLM

The performance of any optical information processing system involving an SLM is determined greatly by the transmission characteristic of the SLM, which is described by its modulation transfer function (MTF) (Goodman, 1996). The MTF of an SLM is a function of the spatial frequency of the input signal and represents the capability of transferring the modulation depth from the input to the output signals (Hsieh, Hsu, Paek & Wilson, 1999). It can be defined as the diffraction efficiency of the displaying grating pattern, which is measured at the Fourier plane of the SLM. It describes the LCSLM’s capability to display patterns at different spatial frequencies.

The MTF of a LCSLM can be analytically determined using the Fourier series expansion technique. Since a LCSLM is a pixelated structure, it can be considered as a grating of period *N* pixels assumed to be in a squared structure with a fill factor of *r*. Thus the MTF of the LCSLM is (Hsieh et al., 1999),

$$M = \frac{4(a^2 + b^2)}{\pi^2 r^2}, \tag{3.33}$$

where

$$a = \sum_{n=0}^{N-1} \cos\left[\frac{2\pi}{N}\left(n + \frac{r}{2}\right)\right] \sin\left(\frac{\pi r}{N}\right), \tag{3.34}$$

and

$$b = \sum_{n=0}^{N-1} \sin\left[\frac{2\pi}{N}\left(n + \frac{r}{2}\right)\right] \sin\left(\frac{\pi r}{N}\right). \tag{3.35}$$

For the LCSLM, the minimum period is $N = 2$, which corresponds to the pattern of ON and OFF for every alternate pixels. In general, the MTF of a LCSLM is high at high grating frequencies but is uniform at low frequencies. Further, it is not affected by the fill factor except for the grating with maximum spatial frequency ($N = 2$).

3.5 Computer Generated Holograms (CGHs)

3.5.1 Introduction

A hologram is a recorded interference pattern between a wavefront, scattered from an object, and a coherent wave, called the reference wave. A hologram is usually recorded on an optically flat surface, but contains information about the entire three-dimensional wavefield. This information is coded in the form of bright and dark micro interferences, usually not visible for the human eye due to the high spatial frequencies. The object wave can be reconstructed by illuminating the hologram with the reference wave again. This reconstructed wave is indistinguishable from the original object wave. An observer sees a three-dimensional image which exhibits all the effects of perspective and depth of focus (Schnars & Jüptner, 2002).

Conventional holography requires the existence of a real physical object in order for a hologram to be produced. However, in computer generated holograms (CGHs) images of objects that do not exist in the real physical world can be easily created. Computer generated holography refers to the use of analytical methods to create holograms by means of a digital computer, which are then transferred to a transparency by means of a suitable output device (such as a plotter of a printer) (Goodman, 1996). Such holograms enable the generation of wavefronts with any desired amplitude and phase distribution and are thus very useful for a wide range of applications.

Computer generated holography was invented by Brown and Lohmann (1966) as a means of creating wavefronts that could be defined mathematically. The design of CGHs is based on detour phase, which refers to the phase shift introduced to the light diffracted from an aperture in a sample cell in a hologram (Lee, 1990). A computer generated hologram (CGH) consists of many apertures of various sizes at various locations shifted differently from a two-dimensional array of a periodic pattern of sample points. At a certain diffraction angle, the position of the aperture relative to the centre of the sample cell determines the phase of the diffracted light while the size of the aperture determines the amplitude of the light (Lee, 1990). Thus, light incident on the CGH will be modulated differently both in amplitude and in phase by different sample apertures.

Computer generated holography has two defining features. First, the object need not exist and hence idealized wavefronts describing a virtual object can be produced. Secondly, hologram synthesis is the reverse of the usual diffraction process, that is, the nature of the image is prescribed or known and the corresponding diffracting object, which is the hologram, is being determined (Tricoles, 1987). The creation of a CGH involves two main steps (Goodman, 1996; Hariharan, 1987): the first being the determination, by calculation, of the complex fields that the object would produce in the hologram plane if it existed. This process involves determining the appropriate number of sampling points for the object and the hologram and executing the correct discrete Fresnel or Fourier transform on the object fields usually using the fast Fourier transform (FT) algorithm (Cochran et al., 1967). The second step involves using the computed values of the discrete FT to produce a transparency (the hologram) which reconstructs the object wave when it is suitably illuminated (Hariharan, 1987).

There are several types of CGHs, which include the binary detour-phase holograms, the kinoform and the referenceless on-axis complex hologram (ROACH). The binary detour-phase holograms consist of many transparent dots on an opaque background and their transmittance assume only the values of zero and unity (Lohmann & Paris, 1967). These holograms use the detour-phase method to modulate the phase of the incident light. The kinoform is a CGH in which all the cells are completely transparent so that the moduli of all the Fourier coefficients are arbitrarily set equal to unity and only the phase of the transmitted light is controlled in accordance with the phase of the computed Fourier coefficients (Hariharan, 1987). Kinoforms have the advantage that they can diffract all the incident light into the final image, unlike binary holograms, but they eliminate entirely the amplitude information of the object by assuming that the phases of the Fourier coefficients carry majority of the information about the object (Goodman, 1996). This assumption applies particularly if the object is diffuse and hence its points can be assigned random and independent phases. ROACH is similar to the Kinoform but utilizes a multilayer colour film as a recording medium to control both the amplitude and phase of the Fourier coefficients (Chu, Fienup & Goodman, 1973). Different layers of the film are exposed selectively by light of different wavelengths. When illuminated with monochromatic light, one layer of the film absorbs while other layers are transparent and hence cause phase shifts according to the variations in the film thickness and refractive index (Hariharan, 1987). In this way the amplitude and phase of the transmitted beam are modulated by the hologram.

Several materials have been applied as holographic recording media to produce CGHs. These include silver halide photographic emulsions, dichromated gelatin, photoresists, photopolymers, photochromics, photothermoplastics, and photorefractive crystals (Smith, 1977; Bartolini, 1977; Urbach, 1977; Staebler, 1977; Hariharan, 1980; Duncan & Staebler, 1977). Although some of these materials have significant advantages for specific applications, none meets all the requirements for the ideal holographic recording medium, that is, spectral sensitivity well matched to available laser wavelengths, linear transfer characteristics, high resolution and low noise and either inexpensive or have the ability to be recycled indefinitely (Hariharan, 1987).

3.5.2 Digital Holography

Digital holography came into being when charged-coupled device (CCD) cameras with appropriate numbers and sizes of pixels and fast computers became available. The Fresnel or Fourier holograms are recorded directly by the CCD and stored digitally (Schnars & Jüptner, 2002). As compared with CGHs, digital holograms do not require any film material or any chemical or other processing and hence the speed and flexibility of hologram preparation is greatly enhanced. In digital holography, the analog photographic film or plate used to record conventional holograms is replaced by a digital detector array that records the hologram and a computer that stores it. The reconstruction of the wavefield, which is done optically by illumination of a hologram, is performed by numerical methods. The numerical reconstruction process is based on the Fresnel–Kirchhoff integral, which describes the diffraction of the reconstructing wave at the micro-structure of the hologram (Schnars & Jüptner, 2002). In the numerical reconstruction process, the intensity as well as the phase distribution of the stored wavefield can be computed from the digital hologram. This offers new possibilities for a variety of applications such as for measuring shape and surface deformation of opaque bodies and refractive index fields within transparent media. Other applications include digital holographic imaging (DHI) and digital holographic microscopy (DHM), which permits a high resolution, multi-focus representation of engineered surfaces and living cells (Kemper, Langehanenberg & Von Bally, 2007).

As in conventional holography a digital hologram can be recorded in-line or off axis. A digital off-axis hologram is recorded by superimposing a plane wave and the wave scattered from the object at the surface of a CCD. The resulting hologram is electronically recorded and stored. During reconstruction the virtual image appears at the position of the original object and the real image is formed at the same distance, but in the opposite direction from the CCD, as the object (Schnars & Jüptner, 2002).

3.6 Objective Lens in Infinity-corrected Optical Systems

In infinity-corrected optical systems, the objective lens (also called the microscope objective) produces a flux of parallel light imaged at infinity (often called infinity space) but which are brought to focus at an intermediate image plane by a lens (sometimes called a tube lens) placed behind and some distance from the objective lens (Olympus, 2011). The distance between the objective lens and the tube lens is called the infinity space since the flux of light travel parallel before being focussed by the tube lens. The infinity space can be of any appropriate length, neither too small nor too large. If the space is too small, the number of auxiliary optical components that can be placed between the tube lens and the objective is limited. On the other hand, if the space is too large, the amount of peripheral light waves that can be collected by the lens reduces significantly, resulting in images that have darkened or blurred edges (Olympus, 2011).

The objective and the tube lens form a compound objective lens system, which produces an image at an intermediate plane, a finite distance behind the lens and whose magnification could be different from the specified magnification of the objective lens. The effective magnification, m_{eff} , of the objective lens in the infinity-corrected setup (which is the magnification between the object space and the intermediate image plane) depends on the focal length, f_T, of the tube lens and the focal length, f_o, of the objective lens and is given by (Thorlabs, 2011)

$$m_{eff} = \frac{f_t}{f_0}. \tag{3.36}$$

The focal length, f_o, of the objective is determined from the dimensions of the objective and its working distance (see the dimensional drawing in figure 3.8) (Olympus, 2011).

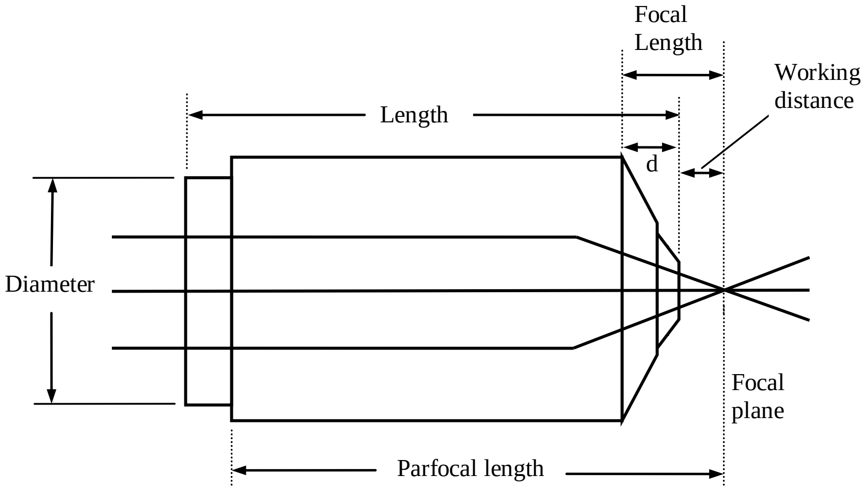

Figure 3.8: A dimensional drawing of the objective lens showing the various lengths (Olympus, 2011)

The focal length of the objective lens is the sum of the length d (measured physically on the actual objective lens) and the working distance, which is usually specified by the manufacturer. For the RMS 10x Olympus Plan N Achromat objective used in this study (see figure 4.6), the working distance was specified as 10.6 mm (Olympus, 2011).

CHAPTER FOUR

METHODOLOGY

4.1 Introduction

In this chapter, the experimental methods applied to generate the two rotating Bessel beams (RBBs) and to investigate their propagation properties are described in detail. Section 4.2 outlines the digital generation of RBBs and section 4.3 outlines the experimental investigation of the rotation rates of their intensity profiles. Section 4.4 presents the experimental investigation of the propagation dynamics of totally and partially obstructed RBBs for on-axis and off-axis obstructions. In addition, the experimental determination of the magnification of the objective lens in infinity-corrected configuration and for the various obstacles used in this investigation is also presented in this section. This experimental work was done in Prof. Andrew Forbes' laboratory at CSIR's National Laser Centre (NLC), Pretoria, South Africa with funding from the African Laser Centre. Prof. Forbes is the Chief Scientist and the research group leader, Mathematical Optics group at NLC.

4.2 Digital Generation of Rotating Bessel Beams

A linearly polarised He–Ne laser beam (of wavelength λ = 632.8 nm and beam radius of about 0.5 mm) was expanded using a 6x telescope and directed onto the liquid crystal display (LCD) of a spatial light modulator (SLM) (HoloEye, PLUTO-VIS, with 1920 x 1080 pixels, each of width 8 µm) over an active sensor area of approximately 15 x 9 mm^2. The SLM had a fill factor of about 90% and was calibrated for a 2π phase shift at 632.8 nm. The experimental set-up is shown in figure 4.1. The technique implemented in this set-up applies digitally generated ring-slits imparted on the phase-only SLM instead of the physical ring-slit applied by Vasilyeu et al. (2009). The technique involved digitally imprinting alternating sets of pixels on the LCD with phase values that are out of phase by π using a digitally generated checkerboard phase pattern, which resulted in the light reflected from the LCD being scattered from its initial direction of propagation (the direction of the zero order). The redistribution of the zero order intensity was necessary because a major limitation of computer generated holograms is the intensity in the zero order that arises from phase imperfections in the hologram (Preece, 2011).

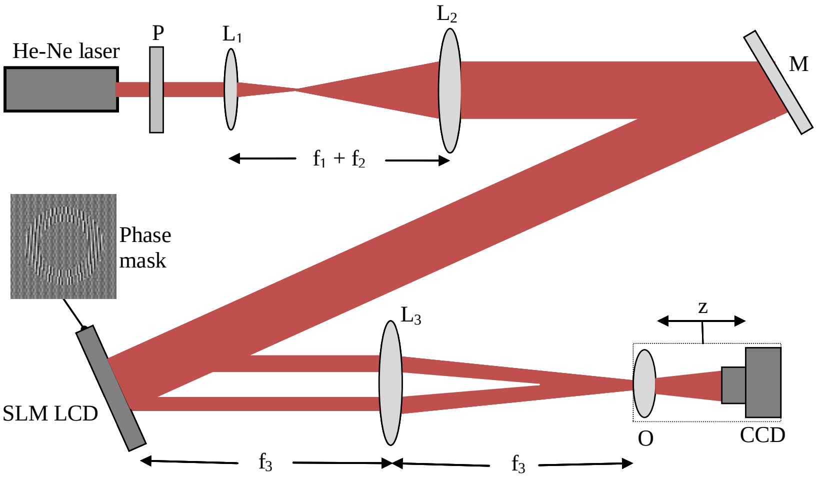

Figure 4.1: Experimental set-up for generating superpositions of higher order Bessel beams. P: Polarizer; L$_1$, L$_2$ and L$_3$: lenses (f_1 = 25 mm, f_2 = 150 mm, f_3 = 200 mm); M: mirror; LCD: Liquid crystal display of spatial light modulator; O: Objective lens; CCD: CCD camera.

Figure 4.2 shows a photograph of the actual experimental set-up that is illustrated diagrammatically in figure 4.1. The experimental technique enabled the creation of digital holograms that acted as pure amplitude functions, which were used to encode annular ring transmission functions of full widths 56 μm, 108 μm, 180 μm, 220 μm, 264 μm and 344 μm respectively. Each annular ring ‘amplitude’ transmission function was sub-divided into two ring slits of equal width. The ring slits were encoded with azimuthal ‘phase’ transmission functions, of opposite handedness, from azimuthal order $m = 1$ to $m = 6$. In this way, the phase-only SLM operated in both amplitude and phase mode and hence allowed the reproduction of Durnin’s ring-slit (Durnin, 1987; Durnin et al., 1987) but with the flexibility to control the phase within the annular rings.

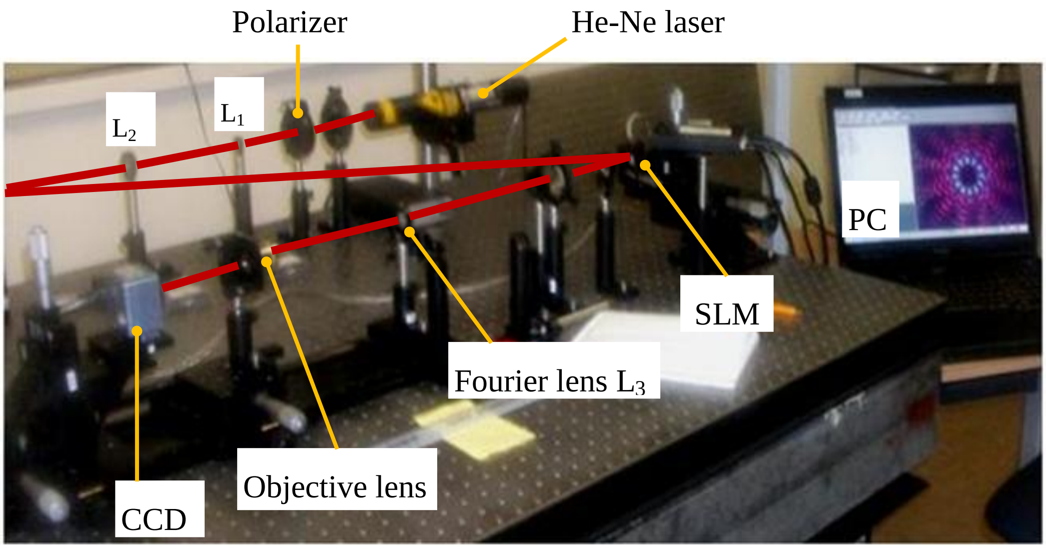

Figure 4.2: A photograph of the experimental set-up used to digitally generate rotating Bessel beams. L_1, L_2: lenses; CCD: camera; SLM: spatial light modulator; PC: computer. The mirror M after lens L_2 is not shown in the picture.

Examples of phase patterns addressed to the SLM for the generation of zero OAM RBBs and Helicon beams are shown in figures 4.3 and 4.4, respectively.

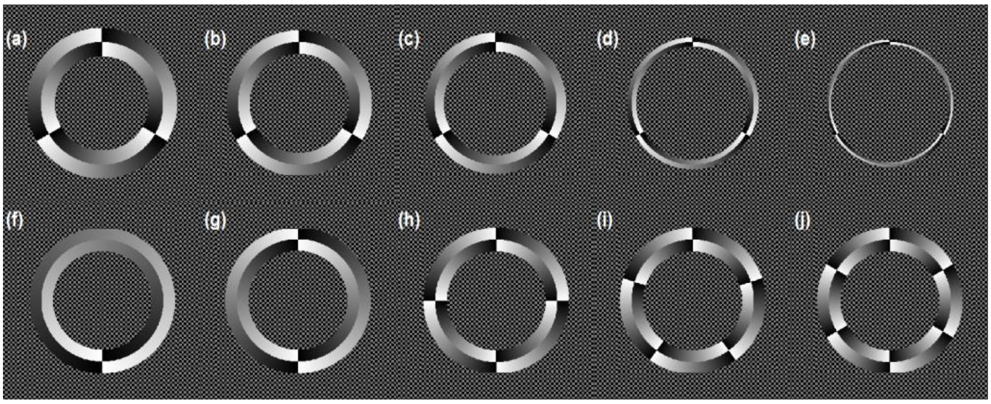

Figure 4.3: Images of the digitally generated phase masks imprinted on the SLM for the generation of zero OAM RBBs.

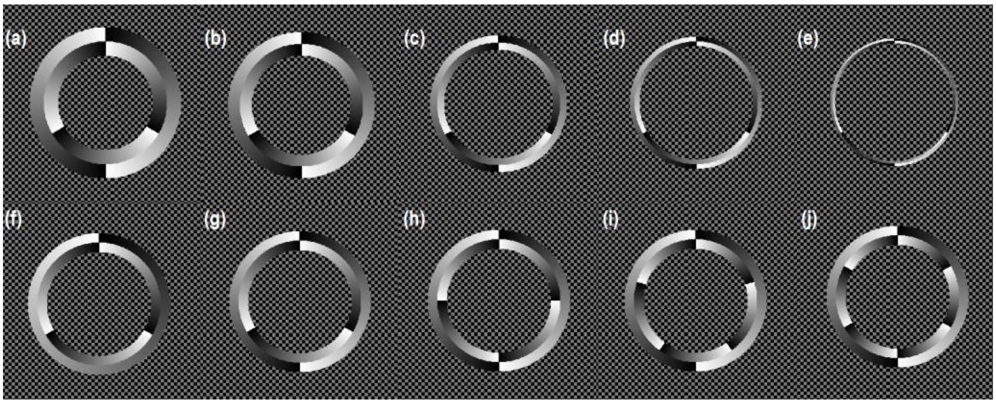

Figure 4.4: Images of the digitally generated phase masks imprinted on the SLM for the generation of Helicon RBBs.

In images ‘a’ to ‘e’ (the top row) of figure 4.3, the phase in both rings varies three times but with opposite handedness and the values of Δk are 130 m^{-1}, 89 m^{-1}, 83 m^{-1}, 41 m^{-1} and 21 m^{-1} respectively. In the bottom row (images ‘f’ to ‘j’), the annular rings have the same value of Δk, that is 89 m^{-1} but the number of times the azimuthal phase varies is $m = \pm 1$, $m = \pm 2$, $m = \pm 4$, $m = \pm 5$ and $m = \pm 6$ respectively. In the top row of figure 4.4 (images ‘a’ to ‘e’), the phase in the outer rings varies two times while in the inner ring it varies three times but with opposite handedness. The values of Δk are 130 m^{-1}, 89 m^{-1}, 66 m^{-1}, 41 m^{-1} and 21 m^{-1} respectively. In the bottom row (images ‘f’ to ‘j’), the annular rings have the same value of Δk, 82 m^{-1}, but the order of the azimuthal phase variation in the rings changes from m1 = 3, m2 = -1; m1 = 3, m2 = -2; m1 = 4, m2 = -2; m1 = 5, m2 = -2 and m1 = 6, m2 = -2 respectively.

A blazed grating of 13 pixels per period was added to the phase patterns to separate the non-diffracted and diffracted components reflected from the SLM (the diffraction efficiency of the SLM was more than 80%). Figure 4.5 shows the checkerboard pattern, the blazed grating, the annular rings and the digital hologram (which is a combination of the checkerboard pattern, the grating and the annular rings) imprinted on the SLM. The Fourier transform field, at the focal plane after L_3 (see figure 4.1) was magnified with a 10x objective and captured on a charge-coupled device (CCD) camera (Spiricon, LBA-FW-SCOR-7350115). The objective and camera were positioned on x-y translation stages which were set on an optical rail in order to investigate the propagation of the resulting field. In the phase patterns (Figures 4.3

and 4.4) the ring-slit is divided into two annular rings each possessing an azimuthal phase of equal order but opposite handedness and hence the resultant rotating field has zero global OAM (Vasilyeu, 2009; Davis et al., 1996).

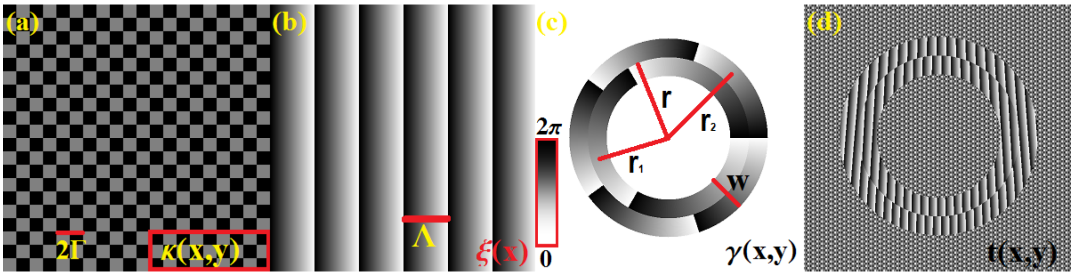

Figure 4.5: Images of (a) the checkerboard with period 2Γ and transmission function κ(x, y), (b) the blazed grating with period Λ and transmission function ξ(x,y), (c) the annular rings with radii r_1 and r_2, width w and transmission function γ(x,y) and (d) the digital hologram imprinted on the SLM, which is a combination of the checkerboard, the grating and the annular rings. The inset in (c) shows the azimuthal phase variation (from 0 to 2π, in the annular rings: three times in the inner ring and five times in the outer ring but in the opposite direction).

The experimental images of the intensity profiles resulting from the superposition of different HOBBs are shown in figures 5.3 and 5.10 of chapter 5 for zero OAM and Helicon RBBs respectively. Also shown in the same figures are the phase patterns imprinted on the SLM to obtain the superpositions and the theoretical images of the same superpositions.

4.3 Determination of Rotation Rates of Rotating Bessel Beams

4.3.1 Zero Orbital Angular Momentum Rotating Bessel Beams

In order to determine the rotation rates of the zero OAM rotating Bessel beams, two higher order Bessel beams (HOBBs) of the same azimuthal order but of opposite handedness were superimposed using the method outlined in section 4.2. The difference, Δk, in the wave numbers of the two superimposed HOBBs, which was determined by the radii of the two annular rings using equation 3.23 were 130 m^{-1}, 89 m^{-1}, 83 m^{-1}, 66 m^{-1}, 41 m^{-1} and 21 m^{-1} respectively. The choice of these values was guided by the fact that, through several experimental trials, it was found that for values of Δk larger than 130 m^{-1}, the ring slits would transmit too much light and the superposition field would be very intense. On the other hand, values of Δk smaller than 21 m^{-1} produced a superstition field with very low intensity. Six values of Δk were chosen since they would be sufficient in showing trends in rotation rates. For each value of Δk, the superposition field was obtained for six different orders of azimuthal phase variation, that is, $m = \pm1, \pm2, \pm3, \pm4, \pm5$ and ±6. Images of the resultant intensity profiles of the superposition fields were captured at various distances, measured from the Fourier lens and along the propagation axis. Examples of the experimental images captured and showing the changing angular position of a particular ‘petal’ at various distances along the propagation axis are shown in figures 5.4 of chapter 5. The angular position of the centroid of a selected ‘petal’ was calculated for each frame at a particular propagation distance. The angular shift or rotation angle, determined as the change in the angular position of the centroid of the particular ‘petal’ was then plotted as a function of the propagation distance, z, of the field. Examples of some of the plots are presented in figures 5.5, 5.6 and 5.7 of chapter 5. The rotation rate of the intensity profile of the field was determined from the slope of the straight line which best fits the measured data. The rotation rate was plotted as a function of the difference, Δk, in the wave numbers and as a function of the order m of the superimposed HOBBs. The plots are presented in figures 5.8 and 5.9, respectively, in chapter 5.

4.3.2 Helicon Rotating Bessel Beams

Helicon Bessel beams were generated using the experimental set up shown in figure 4.1 by superimposing two HOBBs of unequal topological charges. This was achieved by using digital phase masks in which the azimuthal phases in the two annular rings varied from 0 to 2π unequal number of times but with the same or opposite handedness. For example, in the annular ring shown in Figure 4.5(c), the azimuthal phase in the inner ring varied three times in the clockwise sense (m_1 = -3) and five times in the outer ring in the same direction (m_2 = -5). The rotation rates of the Helicon beams were then determined following the method outlined in section 4.3.1. The Δk values for the Helicon beams were the same as those for the zero OAM rotating Bessel beams except for two Helicon beams for which the Δk value was 121 m^{-1}. Figure 4.4 shows examples of the phase patterns imprinted on the SLM to digitally generate the Helicon beams. Experimental images of the resultant intensity of superposition of the Helicon beams are shown in figure 5.10 of chapter 5.

Examples of the experimental images captured and showing the changing angular position of a particular ‘petal’ at various distances along the propagation axis are shown in figure 5.11 of chapter 5. The angular shifts or rotation angles of various intensity profiles at various propagation distances and the rotation rates of the intensity profiles were determined following the method described in section 4.3.1. The plots of angular shifts as a function of propagation distance and of rotation rates as a function of the difference $\Delta m = |m_1 - m_2|$ between the azimuthal orders of the superimposed HOBBs and as a function of the difference, Δk, in the wave numbers of the two HOBBs are presented and discussed in chapter 5.

4.4 Propagation Dynamics of Obstructed Rotating Bessel Beams

This section outlines the experimental method by which the propagation of significantly and partially obstructed ZOAM and Helicon RBBs was investigated. Prior to the investigation, the sizes of individual petals and petal patterns for various values of order m of the superimposing HOBBs were determined. This was necessary in order to make appropriate choices of the obstacles for obstructing the petals and the petal patterns in the intensity profiles of the beams. In addition, since the sizes of the petals as captured by the CCD camera depended on the magnification of the objective lens (microscope objective), there was need to calibrate the objective lens to determine the actual magnification attained in the set-up. The section thus begins with the determination of the magnification of the objective lens.

4.4.1 Calibration of the Objective Lens

In the experimental investigation of the propagation dynamics of RBBs, an Olympus Plan N Achromat RMS 10x objective lens of numerical aperture 0.25 and characterized for visible light was used. The effective focal length of the objective was worked out as 17 mm [115] following the method described in section 3.7. In this investigation, a tube lens of a focal length of 200 mm was used owing to difficulties in obtaining one with a focal length of 170 mm. The theoretical magnification for the objective in the infinity-corrected configuration was then (200 mm/17 mm) = 11.765, using equation 3.36. Figure 4.6 shows a picture of the objective clearly indicating the manufacturer's specifications (Thorlabs, 2011).

Figure 4.6: A picture of the objective lens showing the manufacturer's specifications (Thorlabs, 2011). The yellow band is the colour code for a magnification of 10x.

The magnification of the objective was experimentally determined using the set-up in figure 4.7. A He-Ne laser was expanded four times and directed onto an object at the focal plane of the objective, a distance 17 mm in front of it. Various objects of known sizes: three opaque circular disks of diameters 200 μm, 400 μm and 600 μm respectively and four circular apertures (pin-holes) of diameters 1.2 mm, 1.5 mm, 1.9 mm and 2.0 mm respectively were used. The magnified image of each object was focussed by a tube lens of focal length 200 mm placed at a distance of 55 mm (the infinity space) behind the objective lens onto a CCD camera set at the focal plane of the tube lens. The experimental images of some of the objects used are shown in figure 5.1 of chapter 5. The 'image size' was then plotted as a function of the 'object size' and the slope of the linear fit gave the magnification of the objective lens as 11.515. The plot is shown in figure 5.2 of chapter five.

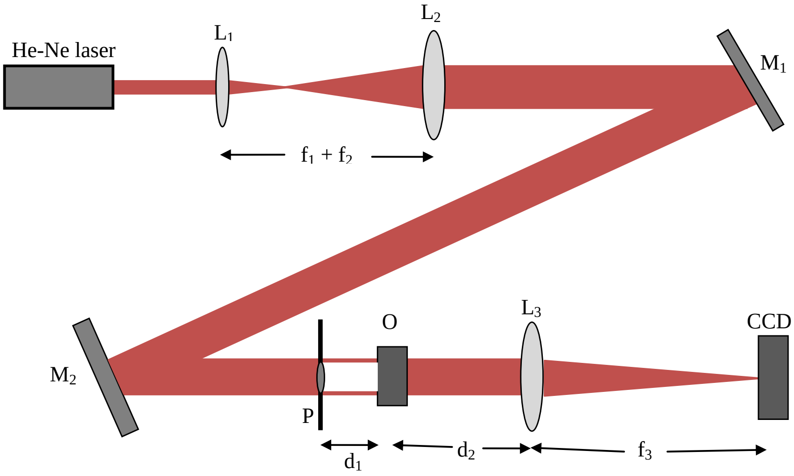

Figure 4.7: Experimental layout for the determination of the magnification of the objective lens. L_1, L_2 and L_3: lenses (f_1 = 50 mm, f_2 = 200 mm); M_1 and M_2: mirrors; P: object plane; O: objective lens; L_3: tube lens (f_3 = 200 mm); CCD: camera. Distances d_1 (focal length of objective) and d_2 (length of the infinity space) were 17 mm and 55mm, respectively.

The distances between the objective and the tube lens and between the tube lens and the CCD camera were maintained throughout the investigation of the propagation dynamics of RBBs and hence the value of the magnification applied for the remaining experiments reported in this section. In addition, using the set up in figure 4.7, the sizes (diameters) of the petals in various intensity patterns of the superposition fields were determined in order to select and use appropriately sized obstacles.

4.4.2 Investigation of the Propagation of Significantly Obstructed RBBs

The propagation of various RBBs past different obstacles set on- or off-axis with respect to the propagation axis of the beams was investigated. The resultant intensity patterns (‘petal’ pattern) of the RBBs were obstructed significantly using opaque circular disks centred on the propagation axis of the beams and the propagation of the obstructed field beyond the obstacles was investigated.

A linearly polarized Gaussian laser beam of radius of about 0.5 mm and average power of 2 mW at 633 nm from a He–Ne laser (ThorLabs HRP020) was expanded and collimated using a 6x telescope. Figure 4.8 shows the experimental set up for investigating the propagation of the obstructed RBBs. The collimated laser beam was then directed onto a phase-only liquid crystal display (LCD) spatial light modulator (HoloEye, Pluto NIR) with 1920 pixels x 1080 pixels each of width 8 μm. The spatial light modulator (SLM) had an active sensor area of about 15 mm x 9 mm, a fill factor of 87% and was calibrated for a 2π phase shift at 633 nm. The RBBs were digitally generated following the method discussed in section 4.3.

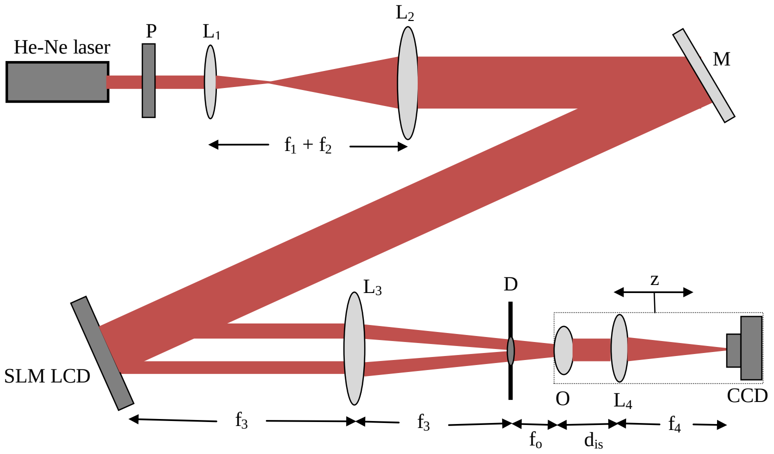

Figure 4.8: Experimental set-up for investigating the propagation of RBBs past various obstructions. P: Polarizer; L$_1$, L$_2$, L$_3$: lenses (f_1 = 50 mm, f_2 = 200 mm, f_3 = 200 mm); M: mirror; LCD: Liquid crystal display of spatial light modulator; D: Plane of obstruction; O: Objective lens (f_o = 17 mm); L$_4$: Tube lens of focal length f_4 = 200 mm; CCD: CCD camera. The length, d_{is} of infinity space was 55 mm.

The 'petal' patterns of the zero OAM RBBs: $m = \pm 1$, Δk = 120 m^{-1}; $m = \pm 2$, Δk = 430 m^{-1}; $m = \pm 3$, Δk = 66 m^{-1}; $m = \pm 3$, Δk = 120 m^{-1} and the Helicon RBBs: $m_1 = 4$, $m_2 = -2$, Δk = 120 m^{-1} and $m_1 = -3$, $m_2 = -5$, Δk = 120 m^{-1} were obstructed significantly (the obstacle was set on-axis so as to block off completely the petal structure) using three opaque disks of diameters 200 μm, 400 μm and 600 μm respectively set at the focal plane of the Fourier lens, which coincided with the focal plane of the objective lens. The light field propagating beyond the obstruction was magnified by the 10x objective (Olympus Plan N Achromat RMS 10x) in the infinity-corrected configuration and captured by a CCD camera (Spiricon USB SP620U of pixel size 4.4 μm, resolution 1600 pixels x 1200 pixels, active sensor area 7.1 mm x 5.4 mm and wavelength range 190–1550 nm). By setting the camera–objective lens combination on an optical rail, the propagation of field at various transverse planes beyond the obstruction was easily investigated. The experimental results and the discussions are presented in chapter 5 of the thesis.

4.4.3 Investigation of the Propagation of Partially Obstructed RBBs

In this section, the experimental investigation of the propagation of partially obstructed RBBs is reported. The propagation of RBBs with partially obstructed 'petal' patterns, with partially obstructed single petals and with significantly obstructed single petals was investigated using the set-up in figure 4.8. The zero OAM RBBs $m = \pm1$, $\Delta k = 120\ m^{-1}$; $m = \pm2$, $\Delta k = 66\ m^{-1}$; $m = \pm3$, $\Delta k = 66\ m^{-1}$; $m = \pm3$, $\Delta k = 120\ m^{-1}$ and $m = \pm6$, $\Delta k = 120\ m^{-1}$ and the Helicon RBBs: $m_1 = 4$, $m_2 = -2$, $\Delta k = 120\ m^{-1}$ and $m_1 = -3$, $m_2 = -5$, $\Delta k = 120\ m^{-1}$ were generated digitally following the technique discussed in section 4.3 and obstructed using two opaque disks 20 μm and 400 μm and two pins, pin 1 and pin 2, respectively. The obstructions were set off-axis with respect to the propagation axis of the beams. Pin 1 had a tip width of 30 μm while pin 2 had a width of 95 μm at the tip. Images of some of the obstacles are shown in figure 5.1 of chapter 5. The field propagating beyond the obstructions was similarly investigated, for each obstruction and beam, at various transverse planes beyond the obstruction. The experimental results and the discussions are presented in section 5.6 of chapter 5 of the thesis.

CHAPTER FIVE

RESULTS AND DISCUSSIONS

5.1 Introduction

This chapter presents the results of all the experimental investigations described in chapter 4. The results of the digital generation of zero OAM and Helicon RBBs, the experimental determination of the rotation rates of the RBBs, the calibration of the objective lens in infinity-corrected configuration and the investigation of the propagation dynamics of obstructed RBBs are presented and discussed. In addition and where possible, theoretically simulated results are presented and compared with the experimental results.

5.2 Magnification of the Objective Lens in Infinity-corrected Mode

The images of some of the objects used in the determination of the magnification of the objective lens in infinity corrected configuration are shown in figures 5.1(a) and (b). The opaque disk in figure 5.1(b) and the pin in 5.1(c) were also used as obstacles in the investigation of the propagation dynamics of obstructed RBBs. From the measured sizes of the obstacles, the magnification of the objective lens was determined by the plot of the image sizes as a function of the object sizes. Figure 5.2 shows a plot of the image size as a function of the object size. The magnification is given by the slope of the linear fit to the plot.

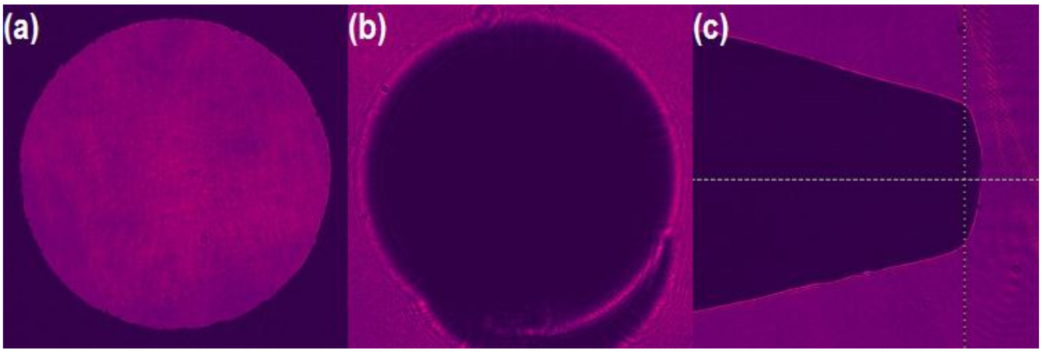

Figure 5.1: Images of some of the objects used in the calibration of the objective lens (‘a’ and ‘b’) and in the investigation of the propagation dynamics of obstructed RBBs (‘b’ and ‘c’); (a) Pinhole of diameter 1.2 mm, (b) opaque disk of diameter 400 µm and (c) pin of tip width 95 µm.

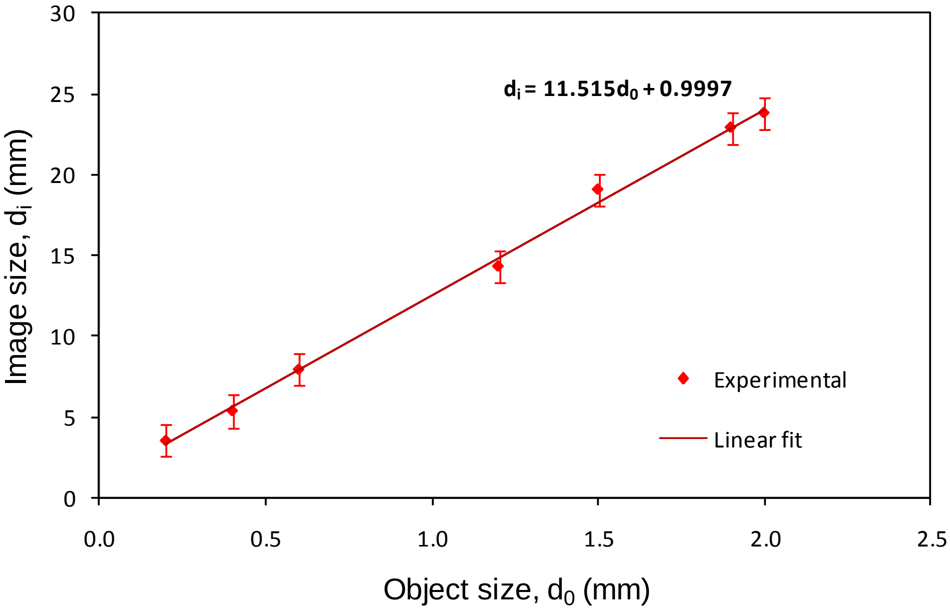

Figure 5.2: Plot of image diameter, d_i as a function of object diameter, d_o. Inset is the trend line equation showing a slope of 11.515.

The experimental value of the magnification of the objective lens, that is, 11.515, agrees well with the theoretical value of 11.765 (see section 4.4.1), with a percentage error of 2.12%, showing that the experimental method attained a good degree of accuracy in the calibration of the objective lens.

5.3 Rotation Rates of Zero-OAM Rotating Bessel Beams

The two HOBBs reflected off the SLM LCD display were superimposed and the superposition field was captured at various transverse planes at specific propagation distances measured from the Fourier plane and along the propagation axis. The resulting intensity patterns of the superposition fields for various values of order m, that is $|m|$=1, 2, 3, 4, 5 and 6, as observed in the Fourier plane, are depicted in the middle row of figure 5.3. The images were approximately 0.2 mm x 0.2 mm in the Bessel zone. The orders, m_1 and m_2, of the two beams and hence of their azimuthal phases were equal in magnitude but of opposite handedness, that is, $m_2 = -m_1$. The intensity of superposition consists of a ‘petal’ structure in which the number of ‘petals’ equals to twice the order m of each of the two superimposed beams. The ‘petals’ (also called ‘lobes’) are points of maximum intensity (due to constructive interference) while the dark regions between the ‘petals’ are points of minimum intensity (due to destructive interference of the two fields).

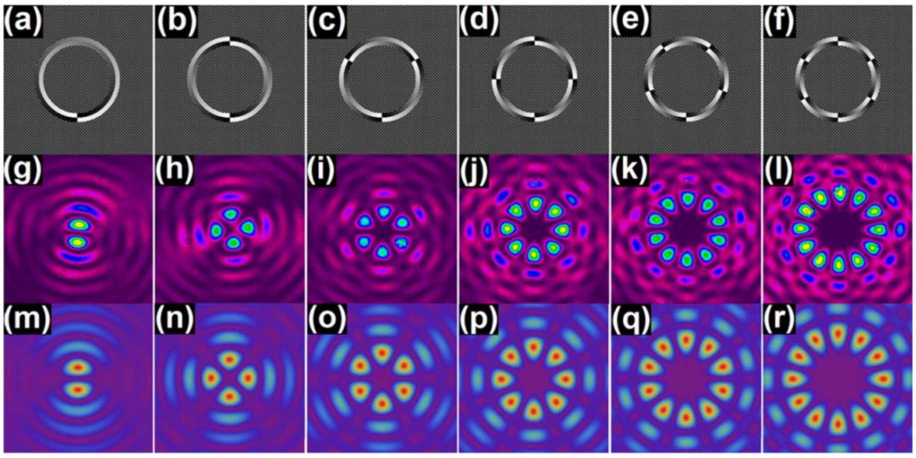

Figure 5.3: Experimental images (middle row) and the corresponding theoretical images (bottom row) of zero OAM RBBs of various orders of equal magnitude but opposite topological charges: $|m|=1$('g' and 'm'), $|m|= 2$ ('h' and 'n'), $|m|=3$ ('i' and 'o'), $|m|= 4$ ('j' and 'p'), $|m|= 5$ ('k' and 'q') and $|m|= 6$ ('l' and 'r'). The top row shows the corresponding digital holograms imprinted on the SLM to generate the experimental images.

From equation (3.25), it can be deduced that the intensity of superposition is modulated in the azimuthal coordinate by the function $\cos^2\left(m\theta\right)$. From the properties of the cosine function, it follows that the number of intensity maxima in the intensity of superposition is twice the order m of each of the superimposing beams.

The top row in figure 5.3 shows the digital holograms imprinted on the SLM in order to implement the superposition of the two fields and hence generate the experimental images. These digital SLM phase masks were generated using MatLab® Software (Knight, 2000). The bottom row shows the theoretical images of the superposition, for various values of order *m*, obtained by simulation using Mathematica® Software (Shifrin, 2008). The MatLab® and Mathematica® scripts used are shown in Appendices B and C, respectively. The agreement between the experimental images, figures 5.3(g) to 5.3(l) and the corresponding theoretical images, figures 5.3(m) to 5.3(r) is excellent showing that the experimental technique is highly accurate for such experiments. From the images it is evident that the spatial extent of the dark core of the intensity of superposition increases with increase in the order, *m*, of the superimposing beams. Consequently, the radius of the circular path described by the 'petal' pattern also increases with increasing order. This is because the 'petals' or 'lobes' are arranged on the circumference of the set of rings defined by the enveloping Bessel function (radial only) of the first kind (equation 3.13), whose radius increases with increase in the order *m* of the function. The intensity profile rotates about the propagation axis as the field propagates along the axis, that is, each 'petal' in the intensity pattern experiences an angular shift in position as the propagation distance, measured from the Fourier plane, increases. As an example, figure 5.4 shows the intensity profiles captured at various propagation distances for the zero OAM RBB for which $|m| = 2$ and the difference, Δk in the longitudinal wave vectors of the two beams was 83 m^{-1}.

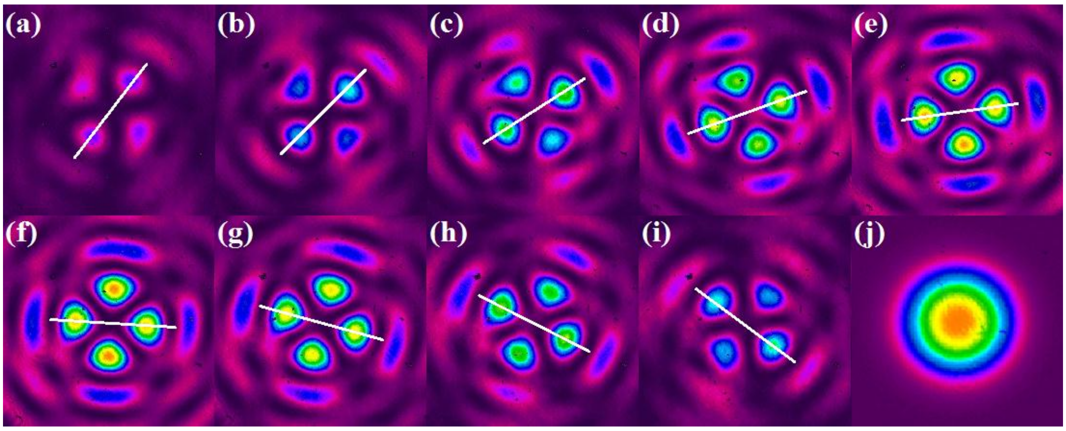

Figure 5.4: Experimental images ('a' to 'i') of the intensity profiles of the superimposed field, for $|m| = 2$, $\Delta k = 83\,\mathrm{m}^{-1}$ captured at intervals of 10 mm along the propagation axis.

It can be observed from figure 5.4 (images 'a' to 'i') that there is a change in the angular position of the petals as highlighted by the white line, which illustrates a rotation in the field as it propagates. Image 'j' shows the Gaussian beam that was incident on the SLM to generate the rotating beams. As expected, the petal structure appears at the beginning of the propagation invariance region with low intensity, which attains a maximum mid-way through the invariance region, and then decreases again as the conical waves separate out back to an annular ring structure. However, while the scale of the pattern is invariant, the intensity profile rotates about the propagation axis. The angular shift of the intensity pattern as a function of propagation distance was deduced using the coordinates of the centroid of a given 'petal'. The coordinates were obtained by manually selecting the pixel at which the peak value of the 'petal' intensity occurred. The standard deviation in the angular shift of the 'petal', was determined by assuming that the manually selected coordinate was within a one-sixth range of the petal's diameter from the true centroid, that is, the standard deviation, θ_σ in the angular shift is given by;

$$\theta_\sigma = \arctan\left(\frac{\sigma}{R}\right) = \arctan\left(\frac{D}{18R}\right), \tag{5.1}$$

where D is the diameter of the 'petal', R is the distance from the centre of the field to the centroid of the 'petal' and σ is the standard deviation in the petal's position. Since the standard deviation in the 'petal' position is scaled as a function of R and R increases with the order, *m*, as is evident from figure 5.3, then the standard deviation θ_σ also scales as a function of the order, *m* (see figure 5.6). For the example plotted in figure 5.5, the standard deviation in the θ is 66 mrad. The absolute error in the propagation distance, given by the smallest increment on the optical rail on which the detection system was mounted, was 1 mm. Figure 5.5 shows a plot of the angular shift as a function of the propagation distance for $m = \pm 3$ and $\Delta k = 66$ m^{-1}.

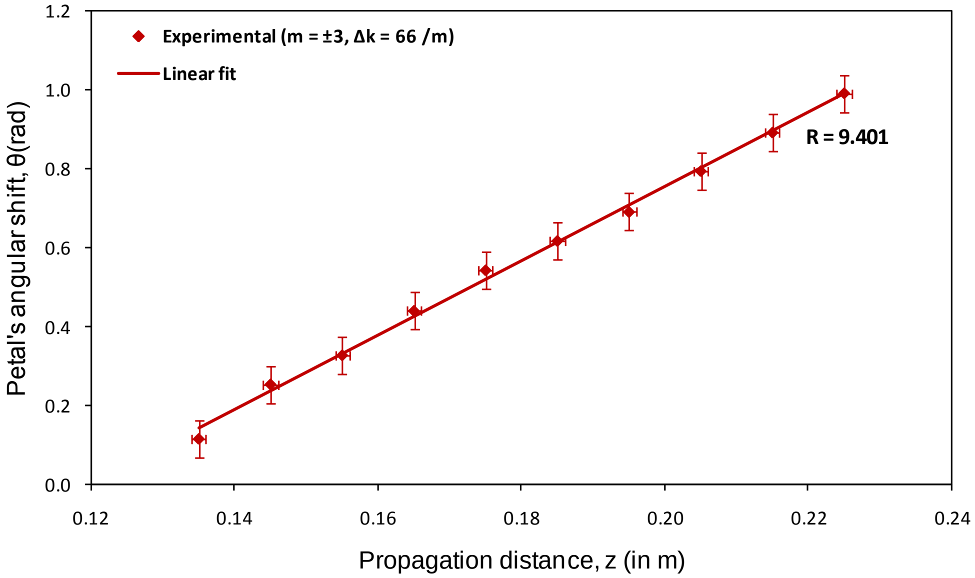

Figure 5.5: Plot of the angular shift (rotation angle) of a 'petal', for the intensity pattern, $|m| = 3$ and $\Delta k = 66\,\mathbf{m}^{-1}$ as a function of the propagation distance, *z*. The rotation rate, 9.626 rad/m, of the pattern is given by the slope of the linear fit.

Similar graphs were obtained for various values of $|m|$ for a given value of Δk and also for various values of Δk for a given value of order m. The corresponding experimental rotation rates were similarly determined from the slope of the linear fit to each plot and are shown adjacent to each plot. As an example, the plots of the petal's angular shift as a function of propagation distance for Δk = 66 m^{-1} and for $|m|$ = 1, 2, 3, 4, 5 and 6 are presented on the same axes in figure 5.6 while figure 5.7 presents similar plots for four values of Δk (41 m^{-1}, 83 m^{-1}, 88 m^{-1} and 130 m^{-1}) and for $|m|$ = 2.

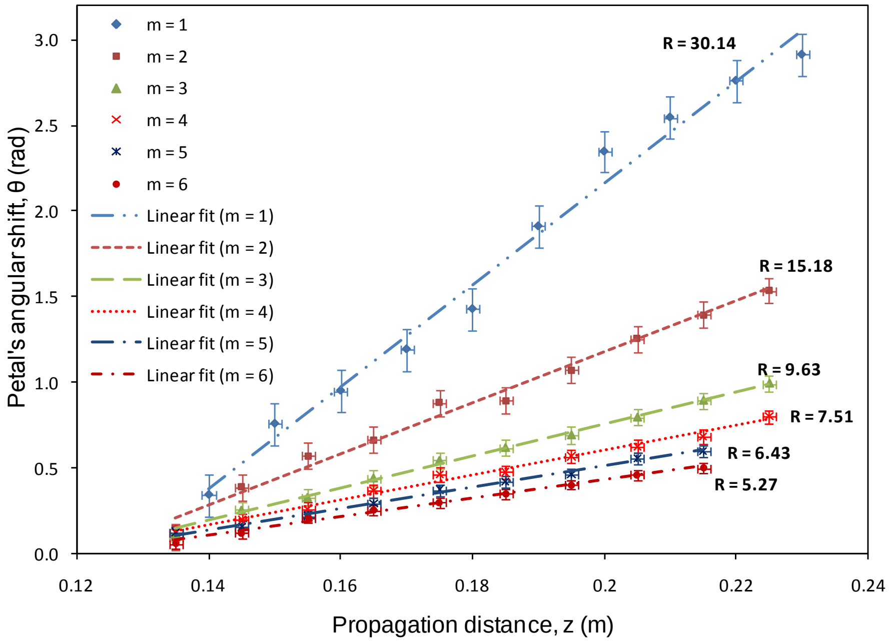

Figure 5.6: Plots of the petal's angular shift as a function of propagation distance, *z* for Δk = 66 m^{-1} and for various values of order *m*. The rotation rate, R of the pattern is indicated on each plot.

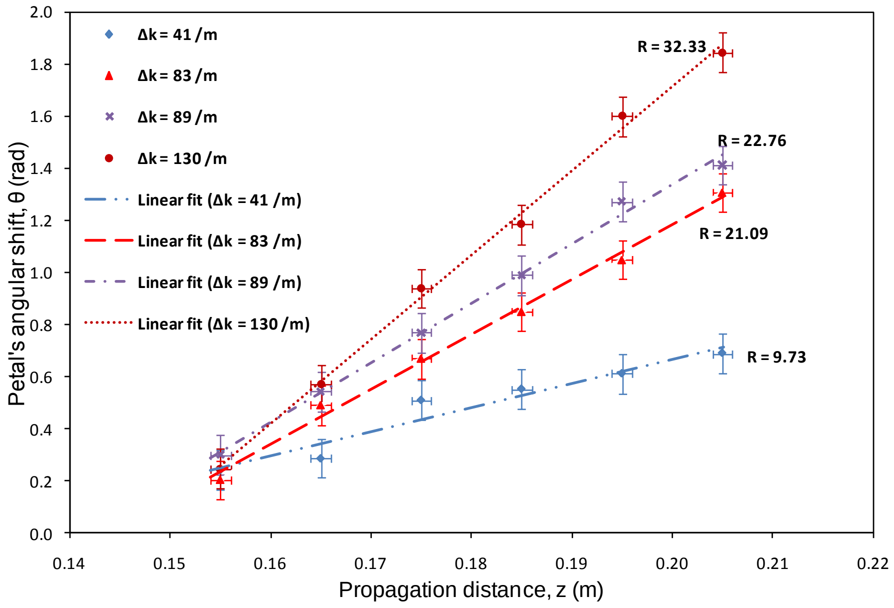

Figure 5.7: Plots of the petal's angular shift as a function of propagation distance, *z* for four values of Δk (41 m^{-1}, 83 m^{-1}, 88 m^{-1} and 130 m^{-1}) and for $|m|$ = 2. The rotation rates of the intensity patterns are indicated on the plots.

The plots in figures 5.5, 5.6 and 5.7 show that, as expected from the expression $\theta = kz/2m$, the angular shift (the rotation angle) of the 'petals' and hence of the intensity profile varies linearly with the propagation distance of the field. In addition, for a given order *m* of the superimposing beams the angular shift varies linearly with the difference, Δk, between the longitudinal wave vectors of the two fields. However, it varies inversely with *m* for a given value of Δk. These experimental results agree well with the theoretical predictions from equation (3.26a). The experimental data was also interpreted by plotting the rotation rate as a function of the order of the azimuthal phase variation, *m*, and of the difference, Δk, between the two longitudinal wave-vectors of the superimposed beams. The plots are shown in figures 5.8 and 5.9 respectively.

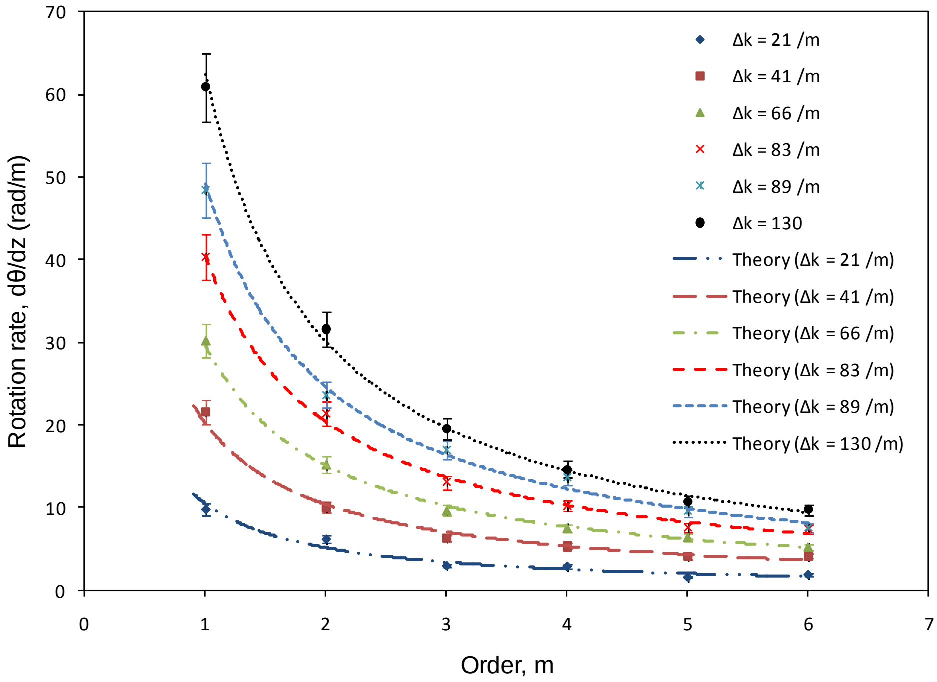

Figure 5.8: Plots of the rotation rate of the intensity pattern as a function of the order, *m* of the superimposed beams, for six different values of Δk (21 m^{-1}, 41 m^{-1}, 66 m^{-1}, 83 m^{-1}, 89 m^{-1} and 130 m^{-1}). The dashed lines are the theoretical fits.

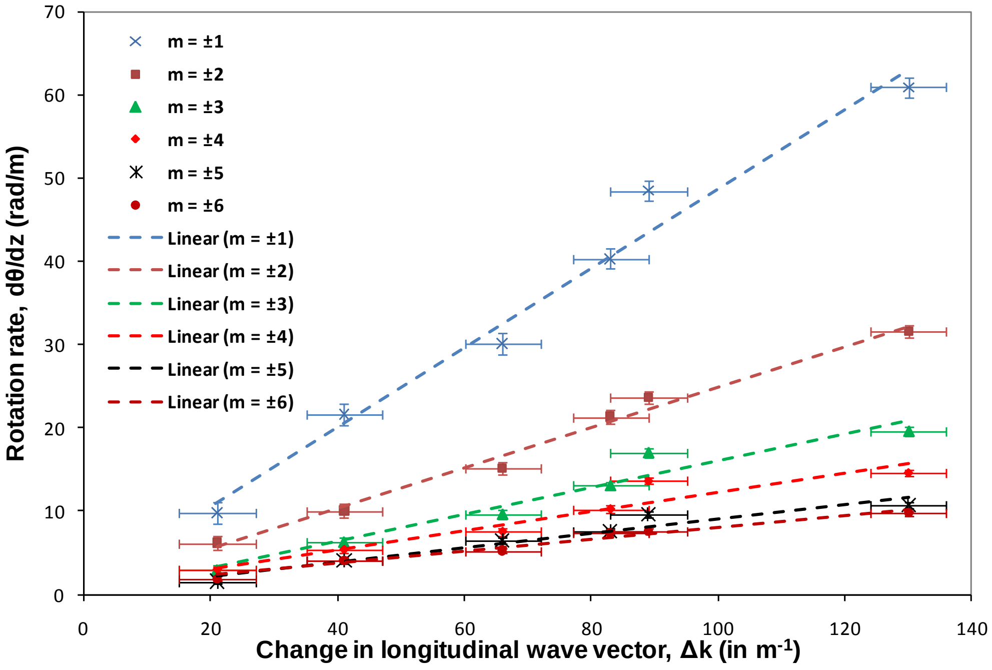

Figure 5.9: Plots of the rotation rate of the intensity pattern as a function of the difference in longitudinal wave vectors, *Δk*, for six different values of order, *m* of the superimposed beams. The dashed lines are the theoretical fits.

Figure 5.8 shows that an increase in the magnitude of *m* results in a hyperbolic decrease in the rotation rate but from figure 5.9, it is evident that an increase in Δk, which was achieved by increasing the width of the inner and outer annular rings, increased the rotation rate of the 'petal' structure linearly. Figures 5.8 and 5.9 both show good agreement between the experimental data (symbols) and the theoretical fits (dashed lines). The error, R_σ in the rotation rate was determined by the error, S_σ in the slope of the graph of the petal's angular shift, θ, as a function of the propagation distance, z, by making use of the following relationship;

$$R_{\sigma} = S_{\sigma} = \frac{\theta_{\sigma} - nz_{\sigma}}{z} = \frac{\theta_{\sigma}}{z}, \tag{5.2}$$

where θ_{σ} is the standard deviation in the angular position of the petal determined using equation (5.1), z is the median of the propagation intervals at which the field is captured and n is the number of intervals. For example, for the case when $|m| = 3$, R_{σ} was found to be 0.5 rad/m. The radius of each ring-slit could be accurately measured to within a single pixel. Taking this absolute error for the radii of the two ring-slits into account, the absolute error for the difference between the two wave vectors was 6 m^{-1}.

For all the results shown thus far, the azimuthal phase within the outer ring-slit varied from white to black (0 to 2π) in an anticlockwise direction and that in the inner ring-slit in a clockwise direction. Inverting the handedness of the two ring-slits resulted in the field rotating with the same rate, but in the opposite direction.

5.4 Rotation Rates of Helicon Beams

The resulting intensity patterns of the Helicon beams, as observed in the Fourier plane, for various values of order Δm but same values of Δk are presented in the middle row of figure 5.10. The top row of figure 5.10 shows SLM phase masks used to digitally generate the beams while the bottom row shows the corresponding theoretical images simulated using Mathematica® software. Figure 5.11 shows the intensity profile of three Helicon beams captured at various transverse planes at specific propagation distances measured from the Fourier plane and along the propagation axis.

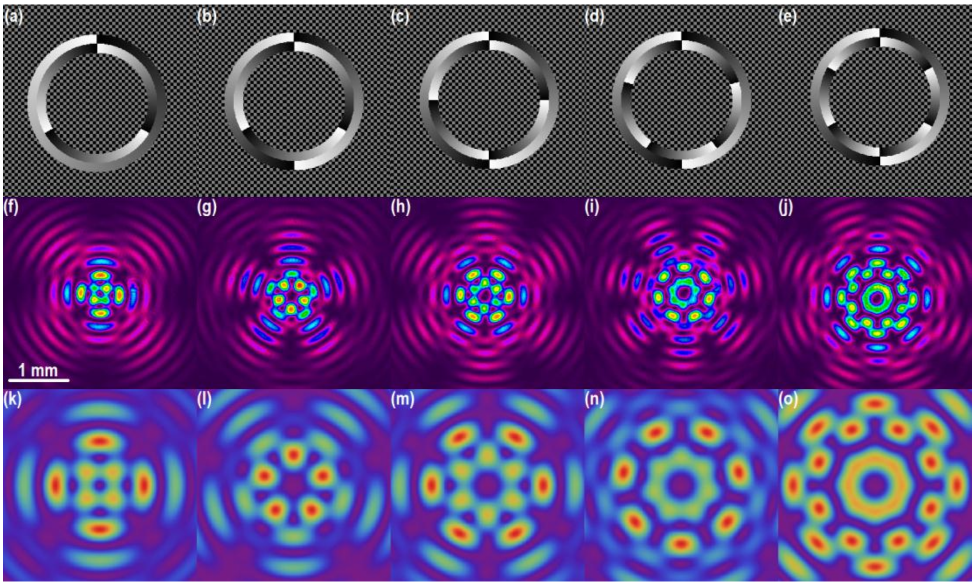

Figure 5.10: Experimental images (middle row) and the corresponding theoretical images (bottom row) of Helicon RBBs formed by the superposition of HOBBs with Δk = 83 m^{-1} and of orders m_1 = 3, m_2 = -1('f' and 'k'), m_1 = 3, m_2 = -2 ('g' and 'l'), m_1 = 4, m_2 = -2 ('h' and 'm'), m_1 = 5, m_2 = -2 ('i' and 'n'), and m_1 = 6, m_2 = -2 ('j' and 'o'). The top row shows the SLM phase holograms used to generate the experimental images.

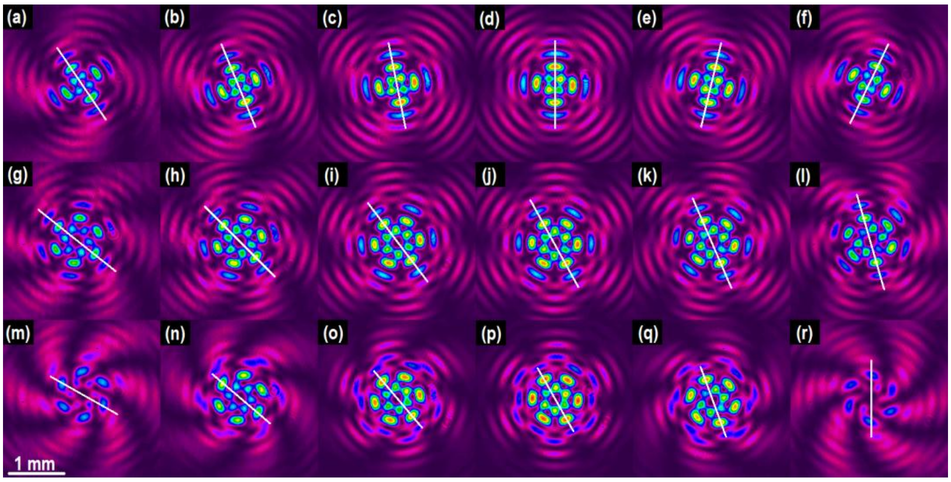

Figure 5.11: Experimental images captured at intervals of 10 mm and showing the clockwise rotation of the intensity profile of Helicon RBBs: Δk = 83 m^{-1}, m_1 = 3 and m_2 = -1(top row); Δk = 83 m^{-1}, m_1 = 4 and m_2 = -2 (middle row) and Δk = 130 m^{-1}, m_1 = 4 and m_2 = -2 (bottom row). The images in each column were captured at equal propagation distances measured from the Fourier plane: The white line in the images shows the angular positions of the 'petals' at various propagation distances.

From figures 5.10 and 5.11, it follows that the intensity pattern of the Helicon RBBs consists of a 'petal' structure in which the number of 'petals' in each ring equals to the absolute difference, $|m_1 - m_2|$ between the azimuthal orders of the superimposed HOBBs. This experimental result follows from the properties of the cosine function in the theoretical prediction in equation (3.25). In addition, there is excellent agreement between the experimental and the theoretical images, showing that the experimental method applied was appropriate and accurate. From figure 5.11, it is apparent that the various Helicon beams rotate but at different rotation rates. A comparison of the rotation of the Helicon beam Δk = 83 m^{-1}, m_1 = 3 and m_2 = -1(top row) with that of Δk = 83 m^{-1}, m_1 = 4 and m_2 = -2 (middle row) shows that the former rotates faster than the latter. Similarly the Helicon beam Δk = 130 m^{-1}, m_1 = 4 and m_2 = -2 (bottom row) rotates faster than Δk = 83 m^{-1}, m_1 = 4 and m_2 = -2 (middle row). These experimental results agree well with the theoretical prediction in equation (3.29) and are confirmed by the plots, shown in figure 5.12, of the angular shift of the 'petals' as a function of propagation distance for the three Helicon beams in figure 5.11. From the experimental and theoretical images in figure 5.10, it is clear that, as expected, the radii of the circular envelope of the 'petals' and the size of the dark core of the intensity pattern increases with increase in the absolute difference $|m_1 - m_2|$ between the orders of the two superimposing beams. In addition, the images in figure 5.11 show that the intensity of the 'petals' is low towards the start and end of the invariance region but is a maximum around the centre of the region. This is due to the fact that the centre of the invariance region is at the focal plane of the Fourier lens.

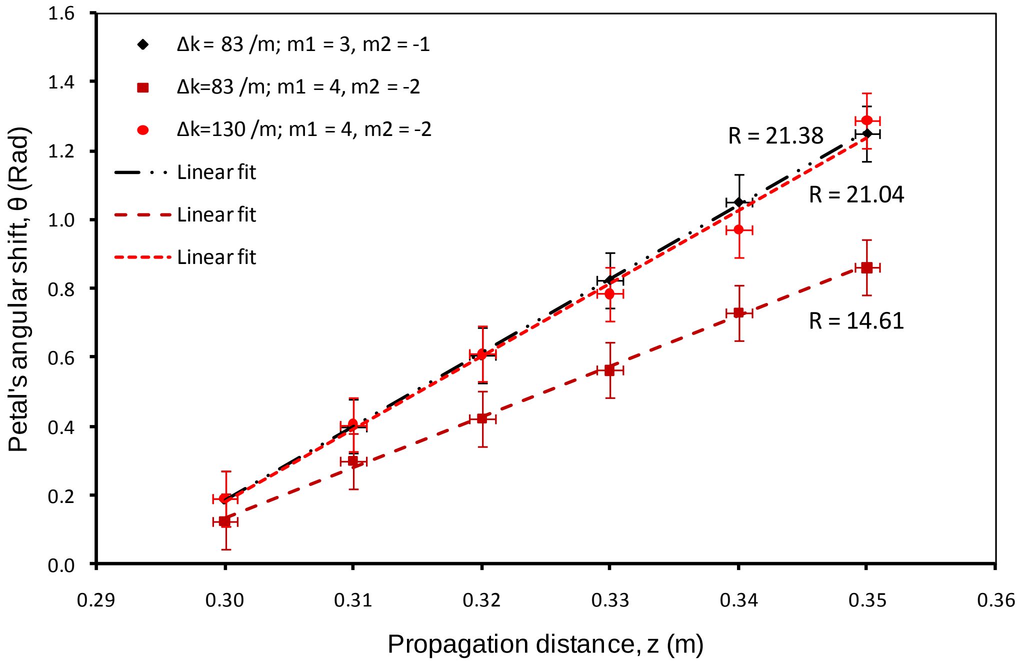

Figure 5.12: Plots of petal's angular shift as a function of propagation distance for the Helicon RBBs: $\Delta k = 83$ m^{-1}, $m_1 = 3$ and $m_2 = -1$; $\Delta k = 83$ m^{-1}, $m_1 = 4$, $m_2 = -2$ and $\Delta k = 130$ m^{-1}, $m_1 = 4$ and $m_2 = -2$. The rotation rates of the intensity profiles of the beams are shown adjacent to the plots.

The theoretical rotation rates of the three Helicon beams, using equation (3.29), are respectively 20.75 rad/m, 13.83 rad/m and 21.67 rad/m and the associated percentage errors are 3.0%, 5.6% and 2.9%, respectively. Thus the experimental results of the rotation rates of the Helicon beams agree well with theoretical predictions.

5.5 Propagation Dynamics of Obstructed Rotating Bessel Beams

5.5.1 Theoretical Results

In order to demonstrate the self-reconstruction of RBBs theoretically, analytical simulations were implemented by directly solving the Fresnel integral [17] using the discrete Fourier transform (DFT) (Sundararajan, 2001). The results of the simulation for the partial obstruction of the petal patterns of two zero OAM rotating Bessel beams; $|m| = 1$, $\Delta k = 120$ m^{-1} and $|m| = 3$, $\Delta k = 120$ m^{-1} respectively and one Helicon beam, $m_1 = -3$, $m_2 = -5$, $\Delta k = 120$ m^{-1} are shown in figure 5.13. For the zero OAM RBBs, a single petal was significantly obstructed while for the Helicon RBB, the petal was partially obstructed.

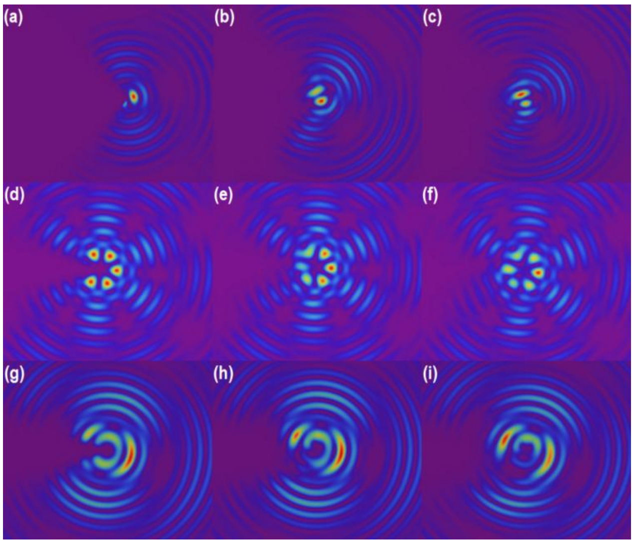

Figure 5.13: Theoretical images of the self-reconstruction of RBBs: zero OAM Bessel beams (top and middle rows) and a Helicon beam (bottom row). Images (a), (d) and (g) are at the plane of obstruction while the other images are at (b) 18 mm, (c) 23 mm; (e) 8 mm, (f) 18 mm, (h) 4 mm and (i) 8 mm along the propagation axis and beyond the obstruction.

The beams in figure 5.13 were theoretically generated for the wavelength λ = 633 nm, radial wave vectors k_{1r} = 63,494 m^{-1}, k_{2r} = 79,863 m^{-1}, difference in longitudinal wave vectors Δk_z = 120 m^{-1} and radii 0.00128 m and 0.001616 m respectively for the inner and outer annular rings. From figure 5.13, it is clear that the three beams reconstruct at different reconstruction distances: 23 mm, 18 mm and 8 mm respectively. This is because the sizes of the obstructions, as seen from images (a), (d) and (g) are different. The minimum reconstruction distance z_{min} varies linearly with the size of the obstacle (see equation 3.30). However, although the sizes of the obstacles in (d) and (g) are almost the same, the Helicon RBB reconstructs much faster (z_{min} = 8 mm) than the zero OAM RBB $|m|$ = 3, Δk = 120 m^{-1} (z_{min} = 18 mm) because the single petal in the Helicon beam was partially obstructed but in the case of zero OAM beam it was significantly obstructed. The self-reconstruction of the beams results in a redistribution of electromagnetic energy and hence intensity among the petals. This can be seen by comparing the intensities of corresponding petals in the last two images of each row in figure 5.13.

5.5.2 Propagation of Significantly Obstructed Zero-OAM RBBs

The intensity (petal) patterns of the two zero OAM RBBs, namely; $|m|$ = 1, Δk = 120 m^{-1} and $|m|$ = 3, Δk = 120 m^{-1} were significantly obstructed on-axis using a 400 µm opaque disk centred at the propagation axis and set at the focal plane of the Fourier lens. The propagating field after the obstruction was captured at various transverse planes (or distances) along the propagation axis. Figures 5.14 and 5.15 show the intensity patterns of the obstructed beams (top rows) and unobstructed beams (bottom rows), taken at corresponding transverse planes, at various propagation distances for the two beams respectively.

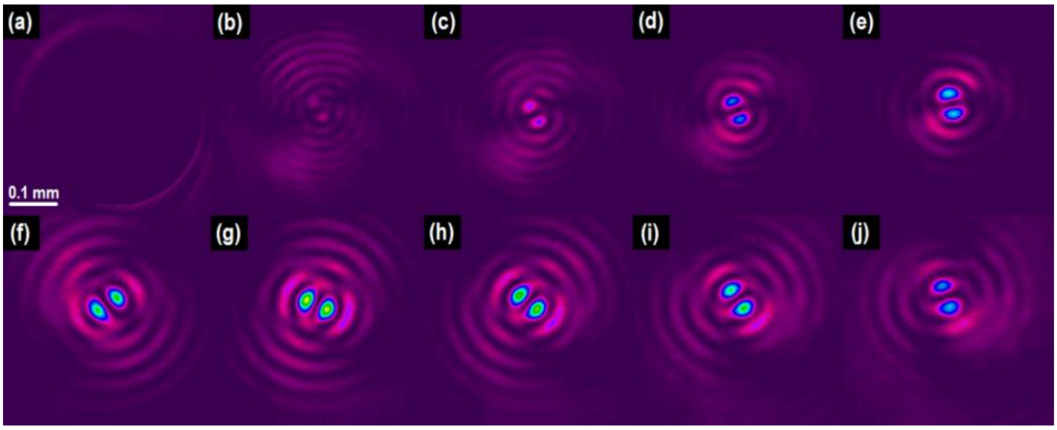

Figure 5.14: Experimental images (top row) showing the propagation of the significantly obstructed zero OAM rotating Bessel beam, $|m| = 1$, $\Delta k = 120\ \mathrm{m}^{-1}$, at various distances beyond the plane of obstruction of the 400 µm opaque disk: (a) 0 mm, (b) 18 mm, (c) 23 mm, (d) 28 mm and (e) 33 mm.

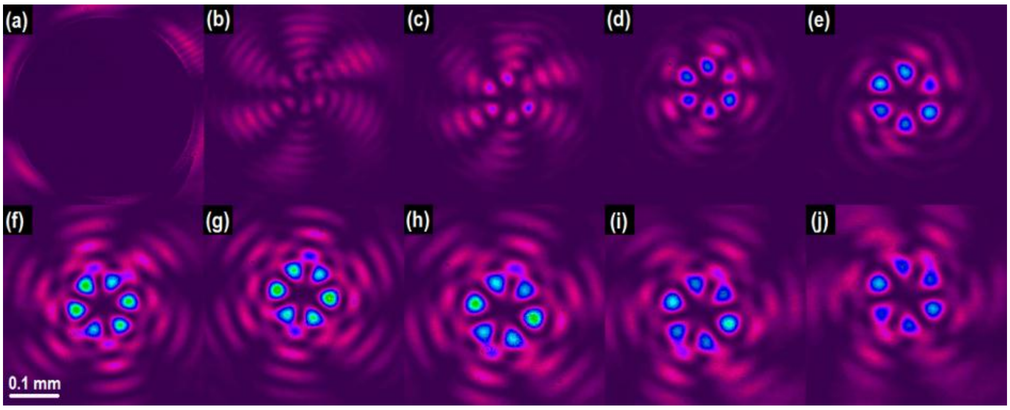

Figure 5.15: Experimental images (top row) showing the propagation of the significantly obstructed zero OAM rotating Bessel beam, $|m| = 3$, $\Delta k = 120$ m^{-1}, at various distances beyond the plane of obstruction of the 400 µm opaque disk: (a) 0 mm, (b) 18 mm, (c) 23 mm, (d) 29 mm and (e) 33 mm.

The theoretical reconstruction distance, $z_{\min}$ calculated from equation (3.30) for the 400 µm on-axis obstruction is 28 mm. From figures 5.14 and 5.15, it is evident that the two zero OAM RBBs reconstruct at a distance of about 28 mm from the plane of obstruction, and hence the experimental reconstruction distances agree with the theoretical value. A comparison of the images of the obstructed and unobstructed beams in figures 5.14 and 5.15 shows that the intensity patterns have the same orientation and symmetry (see for instance images 5.14 ‘e’ and 5.14 ‘j’) indicating that the obstruction does not affect the rotation of the beams. In addition, although the two beams have different rotation rates (54.14 rad/m and 18.40 rad/m respectively) they reconstruct at the same distance showing that the rotation rates of the beams do not affect their minimum reconstruction distances.

5.5.3 Propagation of Significantly Obstructed Helicon RBBs

The ‘petal’ patterns of the two Helicon RBBs, namely; $m_1 = -3$, $m_2 = -5$, $\Delta k = 120\ \mathrm{m}^{-1}$ and $m_1 = 4$, $m_2 = -2$, $\Delta k = 120\ \mathrm{m}^{-1}$ were significantly obstructed on-axis using the 400 µm opaque disk centred at the propagation axis and set at the focal plane of the Fourier lens. The propagating field after the obstruction was captured at various transverse planes (or distances) along the propagation axis. Figures 5.16 and 5.17 show the experimental images of the intensity patterns of the obstructed beams at various transverse planes along the propagation axis for the two beams respectively. Also shown in the bottom rows of the figures are the intensity profiles of the unobstructed beams at distances corresponding to those of the obstructed beams.

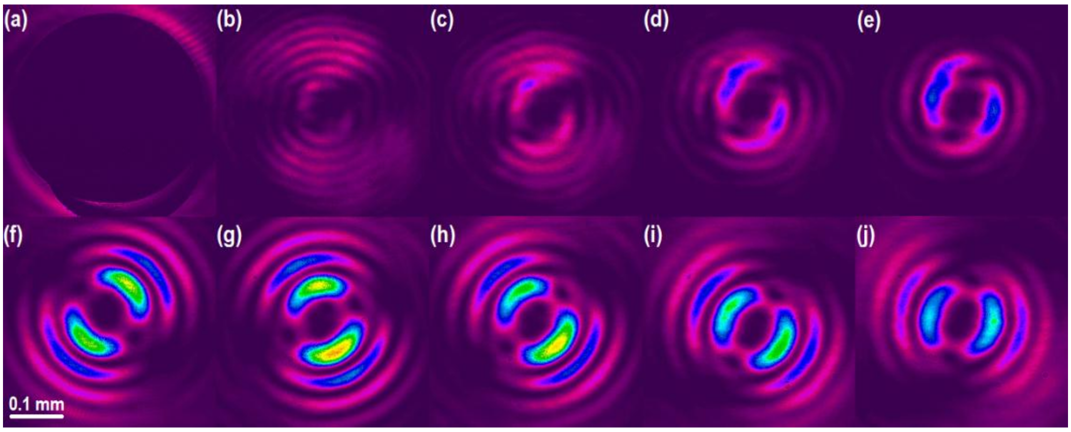

Figure 5.16: Experimental images (top row) showing the propagation of significantly obstructed Helicon rotating Bessel beam $m_1 = -3$, $m_2 = -5$, $\Delta k = 120\ \mathrm{m}^{-1}$, at various distances beyond the plane of obstruction of the 400 µm opaque disk: (a) 0 mm, (b) 18 mm, (c) 23 mm, (d) 28 mm and (e) 33 mm.

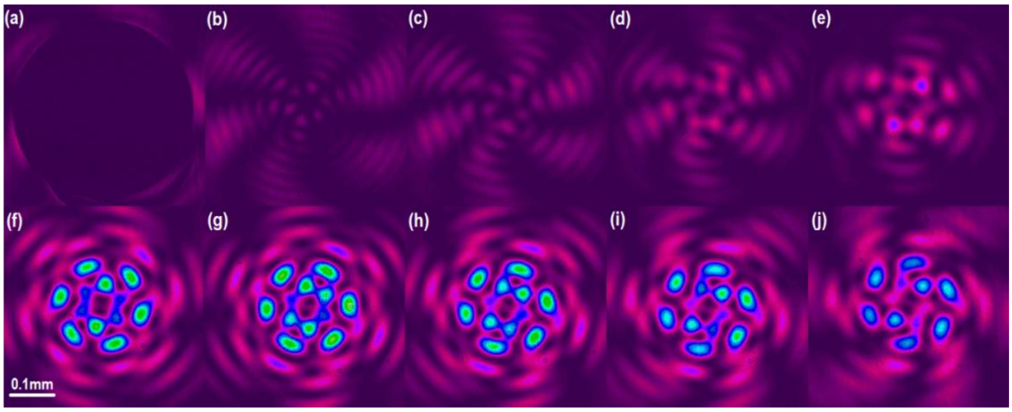

Figure 5.17: Experimental images (top row) showing the propagation of significantly obstructed Helicon rotating Bessel beam, $m_1 = 4$, $m_2 = -2$, $\Delta k = 120$ m^{-1}, at various distances beyond the plane of obstruction of the 400 µm opaque disk: (a) 0 mm, (b) 15 mm, (c) 20 mm, (d) 25 mm and (e) 30 mm.

It can be deduced from figures 5.16 and 5.17 that the reconstruction distances of the two Helicon beams are also about 28 mm from the plane of obstruction. Thus the experimental reconstruction distances agree with the theoretically predicted value of 28 mm. Similarly the reconstructed intensity patterns have the same orientation and symmetry as the unobstructed pattern at the same distances from the plane of obstruction. In addition, the rotation of the beams does not affect their reconstruction (note that the two Helicon beams have different rotation rates, 62.23 rad/m and 22.35 rad/m respectively, but their reconstruction distances are the same). However, from figure 5.17, it is evident that beam does not reconstruct fully: the propagating field does not regain the full profile of the unobstructed pattern. It is possible, for example, that the Poynting vector rotation leads to a flow of energy from the unobstructed petal to the obstructed petal, in addition, to the energy transfer from the conical waves that bypass the obstruction.

5.6 Propagation of Partially Obstructed Rotating Bessel Beams

This section reports the propagation dynamics of the rotating beams for which a single petal in the intensity pattern was partially or significantly (fully) obstructed. The obstruction size was in most cases of the same order as that of the petal, and thus not more than 20% of the total beam size. In the results that follow the obstruction is shown in one of the frames of the data, indicating the relative size of the obstruction to the ‘petal’ and the ‘petal’ pattern.

5.6.1 Partial Obstruction of a Single Petal

A single petal of the Helicon beam Δk = 120 m^{-1}, m_1 = -3, m_2 = -5 was obstructed partially using a pin of tip width of about 30 μm. In addition, single petals of the zero OAM beams: Δk = 120 m^{-1}, m_1 = +3, m_2 = -3 and Δk = 66 m^{-1}, m_1 = +3, m_2 = -3 were obstructed partially using the pin of width 30 μm and an opaque disk of diameter 20 μm respectively. The field propagating beyond each obstruction was captured at different distances measured from the plane of obstruction along the propagation axis. Figures 5.18 and 5.19 show the self-healing dynamics of the three beams respectively. The bottom row (images ‘f’ to ‘j’) in figure 5.18 shows the images of the unobstructed beam at the same distances as the corresponding images in the top row.

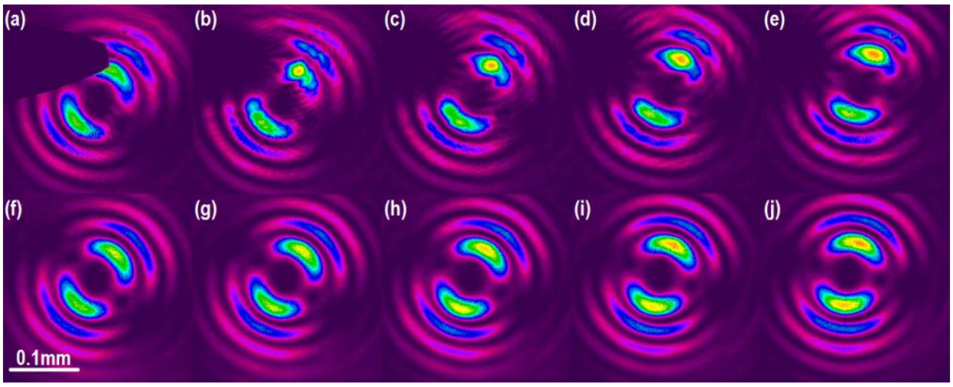

Figure 5.18: Experimental images (top row) showing the propagation of Helicon beam, m_1 = -3, m_2 = -5, Δk = 120 m^{-1} for which a single petal was partially obstructed by a pin tip of width 30 µm. The images were captured at distances: (a) 0 mm, (b) 2 mm, (c) 4 mm, (d) 6 mm and (e) 8 mm beyond the plane of obstruction.

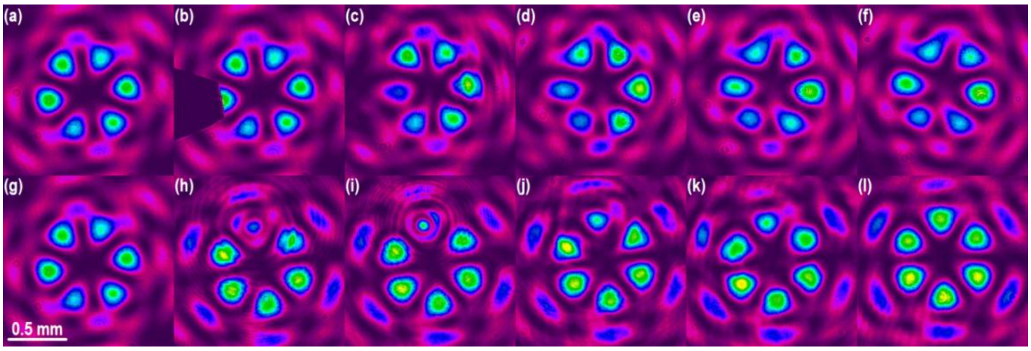

Figure 5.19: Experimental images showing the propagation of zero OAM beams: Δk = 120 m^{-1}, m_1 = +3, m_2 = -3 (images 'b' to 'f') and Δk = 66 m^{-1}, m_1 = +3, m_2 = -3 (images 'h' to 'l') after obstruction by a pin of tip width 30 µm and an opaque disk of diameter 20 µm respectively.

Images ‘b’ to ‘f’ in figure 5.19 were captured at 0 mm, 4 mm, 8 mm, 12 mm and 16 mm respectively while images ‘h’ to ‘l’ were at 0 mm, 2 mm, 4 mm, 6mm and 14 mm respectively from the plane of obstruction. Images ‘a’ and ‘g’ are the unobstructed intensity patterns of the two beams at the plane of obstruction, $z = 0$ mm.

From figures 5.18 and 5.19 it can be observed that although some form of reconstruction of the intensity patterns occurs, the reconstructed beams do not attain the exact nature of the initial patterns. A redistribution of electromagnetic energy occurs resulting in some petal(s) becoming more intense than the other petal(s). As the beam propagates the petals exchange energy such that a petal that is more intense at a particular plane becomes less intense after some propagation distance. In addition, some petals get distorted in shape in the process of reconstruction. This is clearly evident from a comparison of the obstructed and unobstructed images in figure 5.18 and the top row of figure 5.19. However, from the bottom row of figure 5.19, it is apparent that the reconstructed intensity pattern (image ‘l’) is similar to the unobstructed pattern (image ‘g’) except for a shift in the angular position of the petals, which can be attributed to the rotation of the intensity profile of the beam. The difference in the self-healing dynamics of the two beams in figure 5.19 could be attributed to the fact that the pin used as an obstacle in the top row partially obstructs, not just the single petal, but also a part of the intensity pattern adjacent to the petal. However, the 20 μm opaque disk in figure 5.19(h) partially obstructs only the single petal and does not obstruct any intensity in the surrounding region of the petal.

Further, since the disk did not obstruct fully the single petal, diffraction of light around the circular disk occurred, which appeared as diffraction rings concentric about the petal and the Poisson's spot at the centre of the petal in images 5.19(h) and 5.19(i).

The theoretical reconstruction distance of the Helicon beam, Δk = 120 m^{-1}, m_1 = -3, m_2 = -5 for the 30 μm pin obstruction is 6.6 mm. From figure 5.18 the obstructed petal first reappears at a distance of about 8 mm but the initial form of the pattern occurs at 23 mm from the plane of obstruction. In the top row of figure 5.19, the petal reconstructs at a distance of about 8mm and hence the theoretical and experimental reconstruction distances agree fairly well.

5.6.2 Significant Obstruction of a Single Petal

In this section the propagation of rotating beams after significant obstruction of a single petal (similar to partial obstruction of the petal pattern) is presented. A single petal of the zero OAM beam Δk = 120 m^{-1}, m_1 = +1, m_2 = -1 was significantly obstructed using a pin of tip width 95 μm. Similarly, single petals of the zero OAM beam: Δk = 120 m^{-1}, m_1 = +3, m_2 = -3 and the Helicon beam Δk = 120 m^{-1}, m_1 = +4, m_2 = -2 were obstructed partially using the pin of width 30 μm. The field propagating beyond each obstruction was captured at different distances measured from the plane of obstruction along the propagation axis. Figures 5.20, 5.21 and 5.22 show the propagation dynamics of the three beams respectively. The bottom rows show the experimental images of the unobstructed beam at the same distances as the corresponding images in the top row. The intensity patterns rotate in the clockwise direction, in figures 5.20 and 5.21, and in the anticlockwise direction in figure 5.22 as the beams propagate.

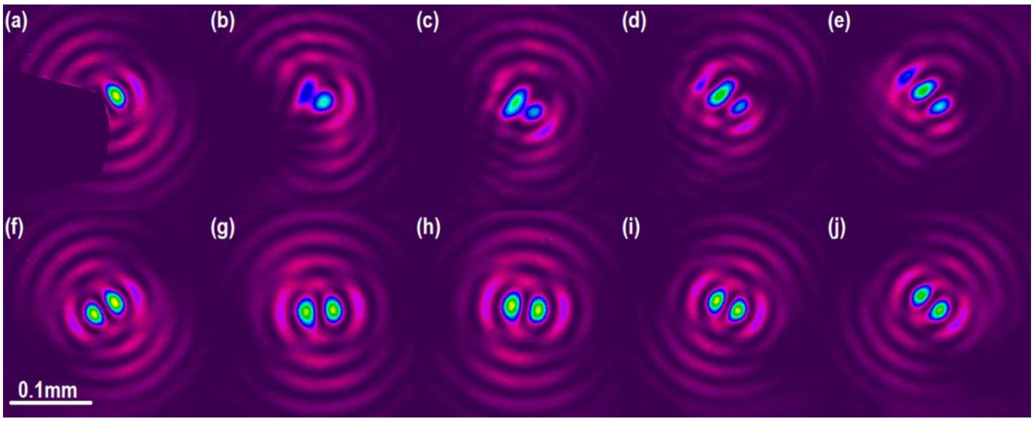

Figure 5.20: Experimental images ('a' to 'e') showing the reconstruction of the partially obstructed petal pattern of zero OAM beam Δk = 120 m^{-1}, $m_1 = +1$, $m_2 = -1$ at various distances from the plane of obstruction: (a) 0 mm, (b) 8 mm (0.38z_{min}), (c) 13 mm (0.62z_{min}), (d) 18 mm (0.86z_{min}) and (e) 23 mm (1.1z_{min}).

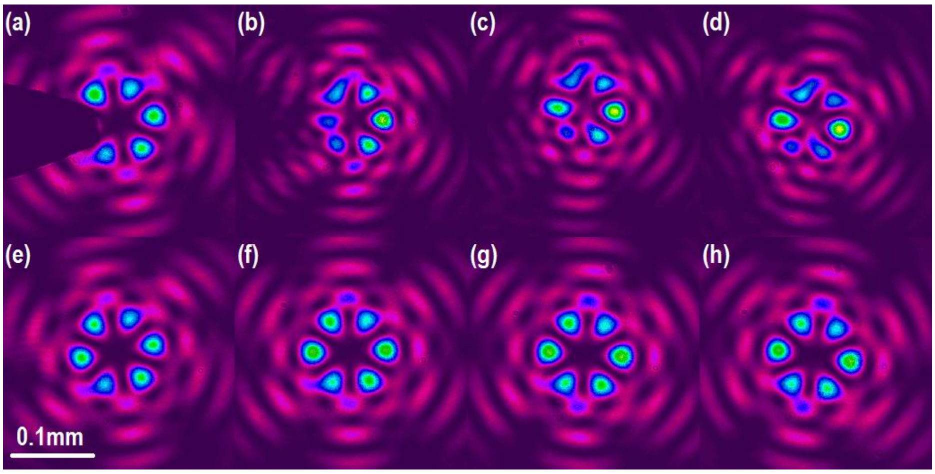

Figure 5.21: Experimental images (‘a’ to ‘d’) showing the reconstruction of the petal pattern of the zero OAM beam Δ*k* = 120 m^{-1}, *m*$_1$ = +3, *m*$_2$ = -3 after significant obstruction of a single petal at various distances from the plane of obstruction (a) 0 mm (b) 8 mm (1.22z$_{min}$) (c) 13 mm (1.98z$_{min}$) (d) 18 mm (2.75z$_{min}$).

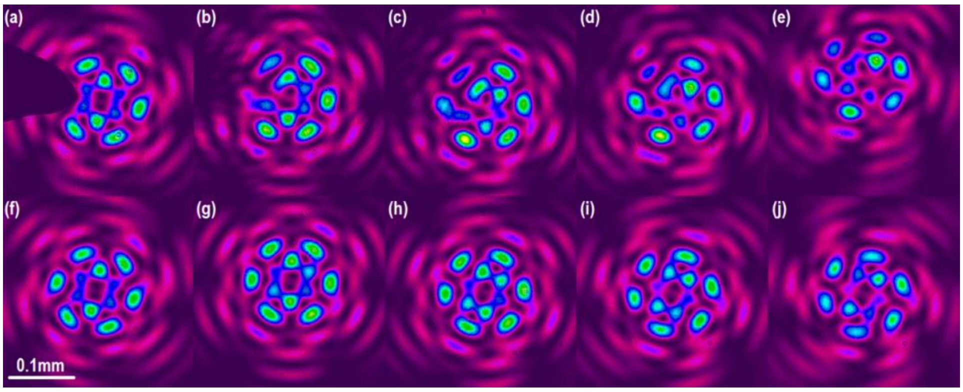

Figure 5.22: Experimental images (‘a’ to ‘e’) showing the reconstruction of the partially obstructed petal pattern of the Helicon beam Δ*k* = 120 m^{-1}, *m*$_1$ = +4, *m*$_2$ = -2 at distances; 0 mm, 8 mm (1.22z$_{min}$), 13 mm (1.98z$_{min}$), 18 mm (2.75z$_{min}$) and 23 mm (3.51z$_{min}$) from the plane of obstruction.

From figures 5.20, 5.21 and 5.22, it is clear that the reconstruction dynamics of beams with significantly obstructed single petals are similar to those of beams with partially obstructed single petals (section 5.6.1). As the beams propagate, the petals exchange electromagnetic energy and some petals get distorted in shape in the process of reconstruction. This is clearly evident from a comparison of the obstructed and unobstructed images in figure 5.20 and from the theoretical results in figure 5.13. The experimental results, shown in figures 5.20 and 5.21 compare well with the theoretical results in figure 5.13. In the three cases of petal obstruction, the obstacle was set off-axis. It is clear from the results in figures 5.18 - 5.22 that the self-reconstruction dynamics of rotating beams after propagating past off-axis obstructions are different from those arising from on-axis obstructions (see figures 5.14 – 5.17). For example, for on-axis obstruction, the reconstruction process does not affect the shapes of the petals unlike for the case off-axis obstruction. In addition, the petals in a given intensity pattern reconstruct uniformly for on-axis obstruction but for off-axis obstruction there appears to be a flow of energy from the unobstructed petal to the obstructed petal, in addition to the energy transfer from the conical waves that bypass the obstruction.

CHAPTER SIX

CONCLUSIONS AND RECOMMENDATIONS

6.1 Introduction

This chapter outlines the conclusions deduced from the experimental results on the digital holographic generation of rotating optical fields (in particular rotating Bessel beams), the investigation of their propagation in free space and the determination of the rotation rates of their intensity profiles. In addition, the chapter presents conclusions on the investigation of the dynamics of dynamics of self-reconstruction of RBBs using obstacles of various sizes and geometries that are positioned at different locations in the beam profile with respect to the axis of the beam. The chapter also presents recommendations, based on the conclusions, for possible future work on the problem area and the general area under study.

6.2 Conclusions

In this work, two types of rotating Bessel beams have been successfully generated using a technique based on digital holography. In addition, the propagation of these beams has been investigated and the rotation rates of their transverse intensity profiles in free space have been successfully measured. The self-reconstruction dynamics of rotating Bessel beams, past on and off-axis partial and total obstructions of various geometries, have also been investigated. The experimental technique that was implemented to generate rotating Bessel beams using digital holographic imprints of their respective angular spectra on a spatial light modulator is a simple and effective method for generation of such optical beams. From a comparison of the theoretical and experimental intensity profiles of the beams, it is clear that there is very good agreement showing that the experimental method was very successful.

The Superposition of two higher order Bessel beams of equal azimuthal orders but opposite topological charges and of distinct azimuthal orders was found to result in a superposition field whose transverse intensity profile rotates about the propagation axis as the field propagates along the axis in free space. The transverse intensity profile consists of ‘petals’ or ‘lobes’, which are regions of maximum intensity, arranged on the circumference of the Bessel rings. For the superposition of HOBBs with equal orders but of opposite handedness (that is, zero OAM RBBs), the number of lobes in the intensity profile is equal to twice the absolute value of the order of each beam. For the superposition of HOBBs with distinct orders (that is, Helicon RBBs) the number of ‘petals’ was found to be equal to the absolute difference between the orders of the superimposed beams.

The rotation rates of zero OAM RBBs and of Helicon RBBs were established to vary linearly with the difference in the longitudinal wave numbers of the two superimposed HOBBs. However, the rotation rates of zero OAM RBBs varied inversely with the order of each of the superimposed beams and that of Helicon RBBs varied inversely with the absolute difference between the orders of the two superimposed HOBBs. In addition, it was found that Helicon RBBs have higher rotation rates, even when the topological charges of the component fields were large, as compared to zero OAM RBBs which required low topological charges to attain high rotation rates.

Rotating Bessel beams were found to reconstruct after propagating past obstacles whose dimensions were small compared to the size of the beam. The rotation of the intensity profile did not affect the reconstruction of RBBs. However, the position of the obstacle with respect to the propagation axis of the beam was important in determining the nature of the reconstruction process of the beam. For on-axis obstructions, the reconstructed intensity pattern had the form and orientation of the unobstructed beam, at the same propagation distance, but off-axis obstructions resulted in a beam which did not attain the exact form of the unobstructed beam. A redistribution of the intensity (electromagnetic energy) of the petals was found to occur as the rotating beams propagated beyond the obstruction, that is, the petals exchanged energy in the process of reconstruction such that a petal that was more intense at a particular propagation distance became less intense at subsequent distances along the propagation axis.

6.3 Recommendations

Although significant work has been done in this investigation and useful results obtained, there is still much ground to cover in this field of rotating optical fields so as to fully understand them and open opportunities for the wide range of applications of these beams. In view of this, the following recommendations are therefore put forth.

1. This study has shown that by varying the extent of the annular shaped spectra and the order of the beams imprinted on the SLM, arbitrarily fine control over the rotation rates of the intensity profile can be achieved. It is this ability to control the rotation rate of these rotating fields and the fact that high rotation rates are possible with Helicon rotating Bessel beams that make RBBs ideal for controlled rotation of trapped particles in optical trapping and manipulation. Thus the implementation of optical trapping using these beams is therefore a possible aspect for future investigation, especially in view of the fact that optical tweezing is now an emerging diagnostic tool in medical and biomedical fields. In addition, owing to their ‘petal’ intensity structure and their reconstruction properties, RBBs may be of interest to the optical trapping and tweezing community for customized OAM density fields that may be used to trap multiple objects in a column.

2. In this investigation, RBBs have been studied as scalar rotating optical fields. However, theoretical studies have shown that electromagnetic (vectorial) rotating optical beams have different propagation properties including

different conditions for rotation of their intensity profiles. It would be of great interest to generate vector rotating Bessel fields using the same or any other appropriate experimental technique and to investigate the effect of the polarization state of the fields on the rotation and propagation of these beams.

3. The propagation of RBBs in free space is, to some extent, now understood. It is recommended that there is need to investigate the propagation of these fields in wave guides such as optic fibres and significantly aberrated media to determine how these media affect the propagation properties of the beams.

4. This study has shown that RBBs possess the property of self-reconstruction. The experimental results obtained have shown good agreement with theoretical predictions. However, further studies may need to be carried out to fully characterize the dynamics of self-reconstruction of RBBs with obstructions of different and even complex geometries.

5. The RBBs generated in this study are superpositions of HOBBs, which are examples of canonical optical vortices. It would be of great interest to extend this study to generate experimentally non-canonical optical vortices and to investigate the propagation properties of their superpositions. On the same note, one could explore the possibility of applying the same method used in this study to experimentally generate superpositions of multiple (more than two) HOBBs and investigate their propagation and the parameters affecting

their rotation. The author of this thesis has already done some theoretical simulations on the same.

6. The energy exchange between the petals during the process of reconstruction could be as a result of the rotation of the Poynting vector which leads to a flow of energy from the unobstructed petal to the obstructed petal, in addition to the energy transfer from the conical waves that bypass the obstruction. It would be of interest to construct an experimental set-up to investigate this idea.

7. Finally, although the overall optical efficiency of the experimental set-up was not a consideration in this study, the efficiency of the system can be made close to the efficiency of the SLM by illuminating the digital holograms with an annular field from a conical telescope (two inward facing axicons, suitably separated). This is particularly important in set-ups in which highly intense beams are needed, such as in optical trapping.

REFERENCES

Abramochkin, E., & Volostnikov, V. (1996). Spiral-type beams: optical and quantum aspects. *Optics Communications,* 125, 302 – 323.

Abramochkin, E., Losevsky, N., & Volostnikov, V. (1997). Generation of spiral-type laser beams. *Optics Communications*, 141, 59 – 64.

Al-Ababneh, N., & Testorf, M. (2004). Analysis of free space optical interconnects based on non-diffracting beams. *Optics Communications,* 242, 393 – 400.

Anguiano-Morales, M., Méndez-Otero, M. M., Iturbe-Castillo, M. D., & Chávez-Cerda, S. (2007). Conical dynamics of Bessel beams. *Optical Engineering,* 46 (7), 078001-1 – 078001 - 9.

Anguiano-Morales, M., Salas-Peimbert, D. P., & Trujillo-Schiaffino, G. (2011). Generation of a spiral wave by a modified annular slit. *Optical Engineering*, 50 (7), 078002-1 – 078002-4.

Arfken, G. B., & Weber, H. J. (2001). *Mathematical Methods for Physicists*. New York: Academic Press.

Arlt, J., & Dholakia, K. (2000). Generation of higher-order Bessel beams by use of an axicon. *Optics Communications,* 177, 297-301.

Arlt, J., Garces-Chavez, V. Sibbett, W., & Dholakia, K. (2001). Optical micromanipulation using a Bessel light beam. *Optics Communications,* 197, 239 – 245.

Bandrés, M. A., Gutiérrez-Vega, J. C., & Chávez-Cerda, S. (2004). Parabolic nondiffracting optical wavefields. *Optics Letters*, 29, 44 – 46.

Barbier, P. R., and Moddel, G. (1997). Spatial light modulators: Processing light in real time. *Optics and Photonics News*, 17, 16 – 21.

Bartolini, R. A. (1977). Optical recording media review. In L. Beiser and D. Chen (Eds.), *Optical Storage Materials and Methods: Proceedings of SPIE* (pp. 2 – 9). Bellingham: SPIE.

Bouchal, Z., Wagner, J., & Chlup, M. (1998). Self reconstruction of a distorted nondiffracting beam. *Optics Communications*, 151, 207 – 211.

Bouchal, Z., Wagner, J., & Olivik, M. (1995). Bessel beams in the focal region. *Optical Engineering*, 34, 1680 - 1688.

Boulder Nonlinear Systems. Retrieved August 2010 from http://www.bnonlinear.com/rd/index.htm

Broky, J. A., Siviloglou, G. A., Dogariu, A., & Christodoulides, D. N. (2008). Self-healing properties of optical Airy beams. *Optics Express,* 16 (17), 12880 – 12891

Brown, B. R., and Lohmann, A. W. (1966). Complex spatial filtering with binary masks. *Applied Optics*, 5 (6), 967 – 969.

Butkus, R., Gadonas, R., Janusonis, J., Piskarskas, A., Regelskis, K., Smilgevicius, V., & Stabinis, A. (2002). Nonlinear self-reconstruction of a truncated Bessel beam. *Optics Communications*, 206, 201 – 209.

Chávez-Cerda, S. (1999). A new approach to Bessel beams. *Journal of Modern Optics*, 46, 923.

Chavez-Cerda, S., McDonald, G. S., & New, G. H. C. (1996). Nondiffracting beams: travelling, standing, rotating and spiral waves. *Optics Communications,* 123, 225–233.

Chávez-Cerda, S., Padgett, M. J., Allison, I., New, G. H. C., Gutiérrez-Vega, J. C., O'Neill, A. T., MacVicar, I., & Courtial, J. (2002). Holographic generation and orbital angular momentum of higher-order Mathieu beams. *Journal of Optics B: Quantum and Semiclassical Optics,* 4, S52 – S57.

Chu, D. C., Fienup, J. R., & Goodman, J. W. (1973). Multi-emulsion, on-axis, computer generated holograms. *Applied Optics*, 12, 1366 – 1368.

Cochran, W. T., Cooley, J. W., Favin, D. L., Helms, H. D., Kaenel, R. A., Lang, W. W., Maling, G. C., Nelson Jr., D. E., Rader, C. M., & Welch, P. M. (1967). What is the fast Fourier transform? *Proceedings of IEEE,* 55, 1664 – 1674.

Curtis, J. E., Koss, B. A., & Grier, D. G. (2002). Dynamic holographic optical tweezers. *Optics Communications*, 207, 169 – 175.

Daria, V. R., Palima, D. Z., & Glückstad, J. (2011). Optical twists in phase and amplitude. *Optics Express*, 19 (2), 476 – 481.

Davis, J. A., Carcole, E., & Cottrell, D. M. (1996). Nondiffracting interference patterns generated with programmable spatial light modulators. *Applied Optics,* 35 (4), 599 - 602**.**

Davis, J. A., Guertin, J., & Cottrell, D. M. (1993). Diffraction-free beams generated with programmable spatial light modulators. *Applied Optics*, 32 (31), 6368 - 6370**.**

De Gennes, P. G. (1974). *The Physics of liquid crystals.* Oxford: Clarendon Press.

Dudley, A. (2011). *Superpositions of light fields carrying orbital angular momentum*. Unpublished doctoral dissertation, University of Kwazulu Natal.

Duncan, Jr. R. C., & Staebler, D. L. (1977). Inorganic photochromic materials. In Holographic recording materials. *Topics in Applied Physics*, 20, Ed. H. M. Smith. Berlin: Springer-Verlag, 133 – 160.

Durnin, J. (1987). Exact solutions for non-diffracting beams. I. The scalar theory. *Journal of Optical Society of America A*, 4, 651– 654.

Durnin, J., Miceli Jr, J. J., & Eberly, J. H. (1987). Diffraction-free beams. *Physical Review Letters*, 58, 1499 –1501.

Fahrbach, F. O., Simon, P., & Rohrbach, A. (2010). Microscopy with self-reconstructing beams. *Nature Photonics*, 4, 780 – 785.

Ferreira, F. P., & Belsley, M. S. (2010). Direct calibration of a spatial light modulator by lateral shearing interferometry. *Optics Express,* 18 (8), 7899 – 7904.

Garces-Chavez, V., McGloin, D., Melville, H., Sibbett, W., & Dholakia, K. (2002). Simultaneous micromanipulation in multiple planes using a self-reconstructing light beam. *Nature*, 419, 145 – 147.

Garces-Chavez, V., McGloin, D., Padgett, M. J., Dultz, W., Schmitzer, H., & Dholakia, K. (2003). Observation of the transfer of the local angular momentum density of a multiringed light beam to an optically trapped particle. *Physical Review Letters*, 91 (9) 093602-1 – 4.

Garces-Chavez, V., Volke-Sepulveda, K., Chavez-Cerda, S., Sibbett, W., & Dholakia, K. (2002). Transfer of orbital angular momentum to an optically trapped low-index particle. *Physical Review A*, 66, 063402-1- 8.

Goodman, J. W. (1996). *Introduction to Fourier optics.* New York: The McGraw-Hill Companies, Inc.

Gutiérrez-Vega, J. C., Iturbe-Castillo, M. D., & Chávez-Cerda, S. (2000). Alternative formulation for invariant optical fields: Mathieu beams. *Optics Letters*, 25 (20), 1493 – 1495.

Gutiérrez-Vega, J. C., Iturbe-Castillo, M. D., Ramírez, G. A., Tepichín, E., Rodríguez-Dagnino, R. M., Chávez-Cerda, S., & New, G. H. C. (2001). Experimental demonstration of optical Mathieu beams. *Optical Communications*, 195 (1), 35 – 40.

Hacyan, S., & Jáuregui, R. (2006). A relativistic study of Bessel beams. *Journal of Physics B: Atomic, Molecular and Optical Physics*, 39, 1669 – 1676.

Hamamatsu. Retrieved August 2010 from http://sales.hamamatsu.com

Hariharan, P. (1980). Holographic recording materials: Recent developments. *Optical Engineering,* 19, 636 – 641.

Hariharan, P. (1987). *Optical Holography: Principles, techniques and applications.* Cambridge: Cambridge University Press.

He, H., Friese, M. E. J., Heckenberg, N. R., & Rubinsztein-Dunlop, H. (1995). Direct observation of transfer of angular momentum to absorptive particles from a laser beam with a phase singularity. *Physical Review Letters,* 75 (5), 826-829.

He, W., Liu, Y., Smith, M., & Berns, M. W. (1997). Laser micro-dissection for generation of a human chromosome region-specific library. *Microscopic Microanalysis*, 3, 47 – 52.

Herman, R. M., & Wiggins, T. A. (1991). Production and uses of diffractionless beams. *Journal of the Optical Society of America A,* 8 (6), 932 - 942.

Holoeye Photonics. Retrieved August 2010 from http://www.holoeye.com

Hsieh, M-L., Hsu, K. Y., Paek, E-G., & Wilson, C. L. (1999). Modulation transfer function of a liquid crystal spatial light modulator. *Optics Communications,* 170, 221 - 227.

Jarutis, V., Matijošius, A., Trapani, P. D., & Piskarskas, A. (2009). Spiraling zero-order Bessel beam. *Optics Letters*, 34 (14), 2129 – 2131.

Kemper, B., Langehanenberg, P., & Von Bally, G. (2007). Digital holographic microscopy: A new method for surface analysis and marker-free dynamic life-cell imaging. *Optik and Photonik*, 2, 41 - 44.

Khonina, S. N., Kotlyar, V. V., Soifer, V. A., Honkanen, M., Lautanen, J., & Turunen, J. (1999). Generation of rotating Gauss-Laguerre modes with binary-phase diffractive optics. *Journal of Modern Optics*, 46 (2), 227 – 238.

Khoo, I. C. (1995). *Liquid Crystals: Physical Properties and Nonlinear Optical Phenomena.* New York: Wiley Interscience.

Knight, A. (2000). *Basics of MatLab® and beyond.* London: Chapman & Hall.

Kogelnik, H., & Li, T. (1966). Laser beams and resonators. *Applied Optics*, 5 (10), 1550 – 1567.

Kotlyar, V. V., Khonina, S. N., Skidanov, R. V., & Soifer, V. A. (2007). Rotation of laser beams with zero of the orbital angular momentum. *Optics Communication*, 274, 8 – 14.

Kotlyar, V. V., Soifer, V. A., & Khonina, S. N. (1997). Rotation of multimode Gauss-Laguerre light beams in free space. *Technical Physics Letters,* 23 (9), 657 – 658.

Lee, S. H. (1990). Recent advances in computer generated hologram applications. *Optics and Photonics News*, 18 – 23.

Litvin, I. A., Dudley, A., & Forbes, A. (2011). Poynting vector and orbital angular momentum of superpositions of Bessel beams. *Optics Express,* 19 (18), 16760 – 16771.

Litvin, I. A., McLaren, M. G., & Forbes, A. (2009). A conical wave approach to calculating Bessel-Gauss beam reconstruction after complex obstacles. *Optics Communications*, 282, 1078 – 1082.

Lohmann, A. W., & Paris, D. P. (1967). Binary Fraunhofer holograms, generated by computer. *Applied Optics*, 6 (10), 1739 – 1748.

Lucke, R. L. (2006). Rayleigh-Sommerfeld diffraction and Poisson’s spot. *European Journal of Physics*, 27, 193 – 204.

López-Mariscal, C. (2003). *Propagation of Rotating Invariant Optical Fields*. Unpublished Master’s thesis, Tecnológico de Monterrey.

López-Mariscal, C., Gutiérrez-Vega, J. C., & Chávez-Cerda, S. (2004). Production of higher-order Bessel beams with a Mach-Zehnder interferometer. *Applied Optics,* 43 (26), 5060 – 5063.

MacDonald, M. P., Paterson, P., Volke-Sepulveda, K., Arlt, J., Sibbett, W., & Dholakia, K. (2002). Creation and manipulation of three-dimensional optically trapped structures. *Science*, 296, 1101 – 1103.

MacDonald, R. P., Boothroyd, S. A., Okamoto, T., Chrostowski, J., & Syrett, B. A. (1996). Interboard optical data distribution by Bessel beam shadowing. *Optics Communications,* 122, 169 – 177.

Maiman, T. H. (1960). Stimulated optical radiation in Ruby. *Nature,* 187 **(**4736), 493 – 494.

Martelli, P., Tacca, M., Gatto, A., Moneta, G., & Martinelli, M. (2010). Gouy phase shift in nondiffracting Bessel beams. *Optics Express*, 18 (7), 7108 – 7120.

Matijošius, A., Jarutis, V., & Piskarskas, A. (2010). Generation and control of the spiraling zero-order Bessel beam. *Optics Express*, 18 (9), 8767 – 8771.

McGloin, D., & Dholakia, K. (2005). Bessel beams: diffraction in a new light. *Contemporary Physics,* 46 (1), 15 – 28.

Montgomery, W. D. (1967). Self-Imaging objects of infinite aperture. *Journal of Optical Society of America*, 57 (6), 772 – 775.

Moon, I., Daneshpanah, M., Anand, A., & Javidi, B. (2011). Cell identification with computational three-dimensional holographic microscopy. *Optics and Photonic News*, 22 (10), 18 – 23.

Morris, J. E., Čižmár, T., Dalgarno, H. I. C., Marchington, R. F., Gun-Moore, F. J., & Dholakia, K. (2010). Realization of curved Bessel beams: propagation around obstructions. *Journal of Optics,* 12, 1 – 5.

Neff, J. A., Athale, R. A., & Lee, S. H. (1990). Two-dimensional spatial light modulators: A tutorial. *Proceedings of the IEEE*, 78 (5), 826 – 855.

Olympus microoptics. (2011). Retrieved 2nd July, 2011, from http://www.olympusmicro.com

Olympus Plan N Achromat objectives. (2011). Retrieved 2nd July, 2011, http://www.thorlabs.com

Pääkkönen, P., Lautanen, L., Honkanen, M., Kuittinen, M., Turunen, J., Khonina, S. N., Kotlyar, V. V., Soifer, V. A., & Friberg, A. T. (1998). Rotating optical fields: experimental demonstration with diffractive optics. *Journal of Modern Optics*, 45, 2355-2369.

Pagani, Y. & Nasalski, W. (2005). Diagonal relations between elegant Hermite-Gaussian and Laguerre-Gaussian fields. *Optoelectronics Review*, 13 (1), 51 – 60.

Paterson, C., & Smith, R. (1996a). Helicon waves: propagation-invariant waves in a rotating coordinate system. *Optics Communications*, 124, 131–140.

Paterson, C., & Smith, R. (1996b). Higher-order Bessel waves produced by axicon-type computer-generated holograms. *Optics Communications*, 124, 121-130.

Paterson, L., MacDonald, M. P., Arlt, J., Sibbett, W., Bryant, P. E., & Dholakia, K. (2001). Controlled rotation of optically trapped microscopic particles. *Science*, 292, 912 – 914.

Peatross, J., & Ware, M. (2011). *The Physics of light and optics.* Brigham Young University.

Preece, D. (2011). *Novel uses of spatial light modulators in optical tweezers*. Unpublished doctoral dissertation. Retrieved August 2011 from http://theses.gla.ac.uk/2619/

Quimby, R. S. (2006). *Photonics and Lasers*. New Jersey: Wiley-Interscience.

Recami, E., & Zamboni-Rached, M. (2009). Localized waves: A review. *Advances in Imaging and Electron Physics*, 156, 235 - 353.

Robinson. J. P., Rajwa, B. P., Bae, E., Patsekin, V., Roumani, A. M., Bhunia, A. K., Dietz, J. E., Davisson, V. J., Dundar, M. M., Thomas, J., & Hirleman, E. D. (2011). Using scattering to identify bacterial pathogens. *Optics and Photonic News,* 22 (6), 20 – 27.

Saastamoinen, T., Tervo, J., Vahimaa, P., & Turunen, J. (2004). Exact self-imaging of transversely periodic fields. *Journal of Optical Society of America A,* 21 (8), 1424 - 1429.

Schechner, Y. Y., Pietsun, R., & Shamir, J. (1996). Wave propagations with rotating intensity distributions. *Physical Review E,* 54 (1), R50 – R53.

Schnars, U., and Jüptner, W. P. O. (2002). Digital recording and numerical reconstruction of holograms. *Measurement Science and Technology,* 13, R85–R101.

Scott, G., & McArdle, N. (1992). Efficient generation of nearly diffraction-free beams using an axicon. *Optical Engineering,* 31 (12), 2640-2643.

Shifrin, L. (2008). *Mathematica*® *programming: An advanced introduction.* California: Creative Commons.

Siviloglou, G. A., Brokly, J., Dogariu, A., & Christodoulides, D. N. **(**2007). Observation of accelerating Airy beams. *Physical Review Letters*, 99, 213901-1-4.

Smith, H. M. (1977). (Ed.). *Holographic recording materials*: *Topics in Applied Physics,* 20. Berlin: Springer-Verlag,.

Sogomonian, S., Klewitz, S., & Herminghaus, S. (1997). Self-reconstruction of a Bessel beam in a nonlinear medium. *Optics Communications,* 139, 313 – 319.

Staebler, D. L. (1977). Ferroelectric crystals. In H. M. Smith (Ed.), *Holographic recording material: Topics in Applied Physics* (pp.101 – 132). Berlin: Springer-Verlag.

Stockley, J., Subacius, D., & Serati, S. (1999). The influence of the inter-pixel region in liquid crystal diffraction gratings. *Liquid Crystal Displays II,* 3635, 18–29.

Stratton, J. A. (1941). *Electromagnetic Theory*. New York: McGraw-Hill.

Sun, Q., Zhou, K., Fang, G., Liu, Z., & Liu, S. (2011). Generation of spiraling higher-order Bessel beams. *Applied Physics B: Lasers and Optics,* 10 (1007), 215 - 221

Sundararajan, D. (2001). *Discrete Fourier transform: Theory, algorithms and applications.* Singapore: World Scientific.

Tabosa, J. W. R., & Petrov, D. V. (1999). Optical pumping of orbital angular momentum of light in cold Cesium atoms. *Physical Review Letters*, 83 (24), 4967-4970.

Tao, S. H., & Yuan, X. (2004). Self-reconstruction property of fractional Bessel beams. *Journal of the Optical Society of America A*, 21 (7), 1192 – 1197.

Tervo, J., & Turunen, J. (2001). Rotating scale-invariant electromagnetic fields. *Optics Express*, 9 (1), 9 – 15.

Thomson, L. C., & Courtial, J. (2008). Holographic shaping of generalized self-reconstructing light beams. *Optics Communication*s, 281, 1217–1221.

Topuzoski, S., & Janicijevic, L. (2009). Conversion of higher-order Laguerre-Gaussian beams into Bessel beams of increased, reduced or zeroth order by use of a helical axicon. *Optics Communications,* 282, 3426 – 3432.

Tricoles, G. (1987). Computer generated holograms: an historical overview. *Applied Optics*, 26 (20), 4351 – 4360.

Turunen, J., & Friberg, A. T. (2009). Propagation-Invariant Optical fields. *Progress in Optics*, 54, 1 – 88.

Urbach, J. C. (1977). Thermoplastic hologram recording. In H. M. Smith (Ed.), *Holographic recording material: Topics in Applied Physics* (pp.161 – 207). Berlin: Springer-Verlag.

Valyaev, A. B., & Krivoshiykov, S. G. (1989). Mode properties of Bessel beams. *Soviet Journal of Quantum Electronics,* 19 (5), 679 – 680.

Vasara, A., Turunen, J., & Friberg, A. T. (1989). Realization of generally nondiffracting beams with computer-generated holograms. *Journal of Optical Society of America A***,** 6 (11), 1748-1754.

Vasilyeu, R., Dudley, A., Khilo, N., & Forbes, A. (2009). Generating superpositions of higher-order Bessel beams. *Optics Express*, 17, 23389–23395.

Verdeyen, J. T. (1995). *Laser Electronics.* New Jersey: Prentice Hall.

Volke-Sepulveda, K., Garcés-Chávez, V., Chávez-Cerda, S., Arlt, J., and Dholakia, K. (2002). Orbital angular momentum of a higher-order Bessel light beam. *Journal of Optics B: Quantum and Semiclassical Optics,* 4, S82 – S89.

Volke-Sepulveda, V., Chavez-Cerda, S., Garces-Chavez, V., & Dholakia, K. (2004). Three-dimensional optical forces and transfer of orbital angular momentum from multiringed light beams to spherical microparticles. *Journal of Optical Society of America B*, 21 (10), 1749 - 1757.

Vyas, S., Kozawa, Y., & Sato, S. (2011). Self-healing of tightly focused scalar and vector Bessel-Gauss beams at the focal plane. *Journal of the Optical Society of America A*, 28 (5), 837 – 843.

Weiner, J., & Ho, P. T. (2003). *Light-matter interactions: Fundamentals and applications.* New Jersey: Wiley-Interscience.

Whittaker, E. T., & Watson, G. N. (1927). *A course of modern analysis* (4th ed.). Westford: Cambridge University Press.

Wong, D. W. K., & Chen, G. (2008). Redistribution of the zero order by use of a phase checkerboard pattern in computer generated holograms. *Applied Optics*, 47 (4), 602 – 610.

Yeh, P. (1993). *Introduction to photorefractive nonlinear optics.* New York: John Wiley & Sons, Inc.

Yu, C., Wang, M. R., Varela, A. J., & Chen, B. (2000). High-density non-diffracting beam array for optical interconnection. *Optics Communications*, 177, 369 – 376.

Zhang, P., Huang, S., Hu, Y., Hernandez, D., & Chen, Z. (2010). Generation and nonlinear self-trapping of optical propelling beams. *Optics Letters*, 35 (18), 3129 – 3131.

APPENDICES

APPENDIX A: PUBLICATIONS AND CONFERENCES

Peer-Reviewed Journal Papers

1. **R. Rop**, I. A. Litvin and A. Forbes, “Generation and propagation dynamics of obstructed and unobstructed rotating orbital angular momentum-carrying Helicon beams.” Journal of Optics **14**, 1 - 11 (2012)
2. **R. Rop**, A. Dudley, C. Lopez-Mariscal and A. Forbes, “Measuring the rotation rates of superpositions of higher-order Bessel beams.” Journal of Modern Optics **59** (3), 259 – 267 (2012)
3. A. Dudley, **R. Rop**, I.A. Litvin, C. Lopez-Mariscal, F.S. Roux and A. Forbes, “Putting light in a spin.” Laser Beam Shaping XIII, Proc. of SPIE Vol. 84900 A-1 (2012)

Conferences

1. **R. Rop**, A. Dudley, Y. Ismail, and A. Forbes, “Rotating light beams,” 3rd African Laser Centre Conference (2010), Stellenbosch, South Africa. (Awarded the ‘Best PhD student presentation.’)
2. **R. Rop**, A. Dudley, Y. Ismail, and A. Forbes, “Investigating the rotation rates of superimposed Bessel beams,” 56th South African Institute of Physics (SAIP) Conference (2010), CSIR, Pretoria, South Africa.

APPENDIX B: MATLAB® SCRIPT FOR GENERATING SLM PHASE MASKS

```
clc;
clear all;
close all;
N=1080;
M=1920;
SLM_bin=zeros(N,M);
R1=181;
L1=-3;
L2=-5;
for n = 1 : N
   for m = 1 : M
      r(n,m) = sqrt((m-M/2)^2+(n-N/2)^2);
      if r(n,m) < R1;
         SLM_bin(n,m) = mod(L1*(atan2((n-N/2),(m-M/2))),2*pi);
      else
          SLM_bin(n,m) = mod(L2*(atan2((n-N/2),(m-M/2))),2*pi);
       end
   end
end
check=zeros(N,M);
for n=1:N
   for m=1:M
      n1=floor(n/5);
      m1=floor(m/5);
      if mod(n1+m1,2)==0
        check(n,m)=pi;%0 .5;
      else
        check(n,m)=0;
      end
   end
end
rmin=round (110);
rmax=round (150);
for n=1:N
   for m=1:M
      r(n,m)=sqrt ((n-N/2)^2+(m-M/2)^2);
      if r(n,m)<=rmax& r(n,m)>=rmin;
        bin_check(n,m)=SLM_bin(n,m);
      else
        bin_check(n,m)=check(n,m);
      end
   end
end
imshow (mod(bin_check,2*pi)./max(mod(bin_check(:),2*pi));
```

APPENDIX C: MATHEMATICA® SCRIPTS FOR SIMULATION OF RBBS

C1: Script for Simulating Zero-OAM Rotating Bessel Beams

```
kr :  80 855;
dk :  83;
myI| m_, r_, phi_, z_|  ::  | Abs| BesselJ| m, kr r| | ^2| | 1 ·  Cos| dk z ·  2 m phi| |

 Table| DensityPlot| myI| 3, Sqrt| x^2 ·  y^2| , ArcTan| y, x| , z| ,
   | x, ·  0.000000005 kr, 0.000000005 kr| ,
   | y, ·  0.000000005 kr, 0.000000005 kr| ,
   PlotPoints ·  100, Axes ·  False, Frame ·  False| , | z, 1| |
```

C2: Scripts for Simulating Helicon Bessel Beams

```
k1r :  69 942;
k2r :  80 855;
k1z :  9 920 764;
k2z :  9 920 681;
m1 : · 5;
m2 : · 3;
myI| r_, phi_, z_|  ::  Abs| | BesselJ| m1, k1r r| | | Exp| I| k1z z ·  m1 phi| | |
     ·  | BesselJ| m2, k2r r| | | Exp| I| k2z z ·  m2 phi| | | | ^2

Table| DensityPlot| myI| Sqrt| x^2 ·  y^2| , ArcTan| y, x| , z| ,
   | x, ·  0.000000005 k1r, 0.000000005 k1r| , | y, ·  0.000000005 k1r, 0.000000005 k1r| ,
   PlotPoints ·  100, Axes ·  False, Frame ·  False| , | z, 0, 1, 0.5| |
```

Or

```
k1r :  69 942;
k2r :  80 855;
k1z :  9 920 764;
k2z :  9 920 681;
dkz :  k1z · k2z;
myI| m1_, m2_, r_, phi_, z_|  ::  Abs| | BesselJ| m1, k1r r| | ^2 ·  | BesselJ| m2, k2r r| | ^2 ·
    2 | BesselJ| m1, k1r r| | | BesselJ| m2, k2r r| | Cos| dkz z ·  | m1 ·  m2|  phi| |

 Table| DensityPlot| myI| · 5, · 3, Sqrt| x^2 ·  y^2| , ArcTan| y, x| , z| ,
   | x, ·  0.000000005 k1r, 0.000000005 k1r| , | y, ·  0.000000005 k1r, 0.000000005 k1r| ,
   PlotPoints ·  100, Axes ·  False, Frame ·  False| , | z, 0, 1, 0.5| |
```

APPENDIX D: DATA TABLES

Table D-1: Image diameter, d_i and object diameter, d_o (Data for figure 5.2)

Object diameter, d_o (mm)	0.2	0.4	0.6	1.2	1.5	1.9	2.0
Image diameter, d_i (mm)	3.52	5.37	7.92	14.30	19.05	22.88	23.78

Table D-2: Petal's rotation angle and propagation distance for the zero OAM RBB *m* = 3, Δ*k* = 66/m (Data for figure 5.5)

Propagation distance (m)	x-coordinate	y-coordinate	x-value	y-value	y/x	Arctan (y/x)	Rotation Angle θ
0.125	628.929	501.647	44.364	67.851	1.529	0.992	0.000
0.135	636.758	496.428	52.193	62.632	1.200	0.876	0.116
0.145	641.977	485.989	57.412	52.193	0.909	0.738	0.254
0.155	644.587	480.770	60.022	46.974	0.783	0.664	0.328
0.165	652.416	475.550	67.851	41.754	0.615	0.552	0.440
0.175	655.026	467.721	70.461	33.925	0.481	0.449	0.543
0.185	657.635	462.502	73.070	28.706	0.393	0.374	0.617
0.195	660.245	457.283	75.680	23.487	0.310	0.301	0.691
0.205	662.855	449.454	78.290	15.658	0.200	0.197	0.794
0.215	662.855	441.625	78.290	7.829	0.100	0.100	0.892
0.225	660.245	433.796	75.680	0.000	0.000	0.000	0.992

Table D-3: Petal's angular shift, θ and propagation distance, z for various values of order, *m* (Data for figure 5.6)

m = 1		m = 2		m = 3		m = 4		m = 5		m = 6	
Propagation Distance (m)	**Rotation Angle θ**	**Propagation Distance (m)**	**Rotation Angle θ**	**Propagation Distance (m)**	**Rotation Angle θ**	**Propagation Distance (m)**	**Rotation Angle θ**	**Propagation Distance (m)**	**Rotation Angle θ**	**Propagation Distance (m)**	**Rotation Angle θ**
0.13	0.000	0.125	0.000	0.125	0.000	0.125	0.000	0.125	0.000	0.115	0.000
0.14	0.340	0.135	0.098	0.135	0.116	0.135	0.121	0.135	0.125	0.125	0.025
0.15	0.756	0.145	0.387	0.145	0.254	0.145	0.194	0.145	0.157	0.135	0.057
0.16	0.949	0.155	0.571	0.155	0.328	0.155	0.258	0.155	0.218	0.145	0.120
0.17	1.191	0.165	0.664	0.165	0.440	0.165	0.366	0.165	0.293	0.155	0.208
0.18	1.427	0.175	0.881	0.175	0.543	0.175	0.461	0.175	0.371	0.165	0.250
0.19	1.911	0.185	0.893	0.185	0.617	0.185	0.475	0.185	0.418	0.175	0.298
0.20	2.348	0.195	1.073	0.195	0.691	0.195	0.567	0.195	0.463	0.185	0.349
0.21	2.548	0.205	1.254	0.205	0.794	0.205	0.625	0.205	0.555	0.195	0.401
0.22	2.762	0.215	1.394	0.215	0.892	0.215	0.683	0.215	0.599	0.205	0.458
0.23	2.915	0.225	1.536	0.225	0.992	0.225	0.799			0.215	0.496

Table D-4: Petal's angular shift, θ and propagation distance, z for various values of Δk (Data for figure 5.7)

dk = 41/m		dk = 83/m		dk = 89/m		dk = 130/m	
z (m)	**θ (Rad)**	**z (m)**	**θ (Rad)**	**z (m)**	**θ (Rad)**	**z (m)**	**θ (Rad)**
0.145	0.1148	0.155	0.2026	0.155	0.3001	0.155	0.2477
0.155	0.2430	0.165	0.4900	0.165	0.5431	0.165	0.5695
0.165	0.2874	0.175	0.6689	0.175	0.7684	0.175	0.9384
0.175	0.5096	0.185	0.8490	0.185	0.9893	0.185	1.1845
0.185	0.5526	0.195	1.0484	0.195	1.2716	0.195	1.5987
0.195	0.6111	0.205	1.3078	0.205	1.4119	0.205	1.8443
0.205	0.6892						

Table D-5: Rotation rates and order, m for various values of Δk (Data for figure 5.8)

Order m	Rotation rates for various values of Δk (Rad/m)					
	Δk = 21	**Δk = 41**	**Δk = 66**	**Δk = 83**	**Δk = 89**	**Δk = 130**
1	9.80	21.60	30.14	40.33	48.47	60.91
2	6.19	10.07	15.18	21.34	23.66	31.61
3	2.95	6.30	9.63	13.06	16.99	19.55
4	2.90	5.32	7.51	10.25	13.65	14.63
5	1.57	4.06	6.43	7.63	9.58	10.71
6	1.90	4.13	5.27	7.45	7.62	9.76